DOCTOR OF PHILOSOPHY

Integrated sensor suite for indoor building inspection with an unmanned aerial vehicle

Fisher, Mark

Award date:
2015

Awarding institution:
Bangor University

Integrated Sensor Suite for Indoor Building Inspection with an Unmanned Aerial Vehicle

Thesis submitted in accordance with the requirements of Bangor University for the degree of Doctor in Philosophy

by

Mark Anthony Fisher

June 2015

Summary

This thesis describes the investigation into the use a small sensor suite mounted on an unmanned aerial vehicle operating inside a building to perform indoor building inspections. Firstly, a current method of performing inspections is described. Parallels are drawn from this method and a review of possible alternative methods for gathering inspection data and positioning remote sensors is presented. Using the evidence from this review an alternative method for gathering and deploying sensors to perform indoor building inspections is proposed. A mathematical description of the position and orientation of a target in 3D space relative to a known coordinate system is then described. In order to create a suitable sensor suite a review of laser range scanning methods and camera types is performed, and devices are then selected for use in the sensor suite. Once the sensor suite hardware is chosen a mathematical description of the orientation and position of a target relative to the sensor suite, unmanned aerial vehicle and world coordinate system is presented. The design and construction of two laboratory test rigs to perform experiments are described in order to evaluate if the first test rig can create 3D point clouds from multiple pitched scans is performed. Following on from the first experiment a second experiment to evaluate if the second test rig can simulate an unmanned aerial vehicle performing an indoor building inspection is performed. The data gathered from the previous experiments required analysis, and a method for displaying visual and range data gathered by the sensor suite on one consistent and useful representation is presented. This method allows both the physical dimensions and visual images gathered by the simulated UAV to be extracted using both data sets. In order to evaluate the accuracy of the proposed method experiments are performed. The use of the sensor suite on “real world” targets is investigated and experiments performed to validate the choice laser range scanner. Once the laser range scanner is validated further experiments are performed to validate the simulated unmanned aerial vehicle and sensor suite in a “real world” test environment. Finally, conclusions are drawn as to how well the system works as well as suggestions for the future direction of the project.

Contents

List of Figures

List of Tables

Nomenclature

UAV	Unmanned Aerial Vehicle
MEWP	Mobile Elevation Work Platform
3D	Three Dimensional
2D	Two Dimensional
CMOS	Complementary Metal Oxide Semiconductor
CCD	Charged Coupled Device
LIDAR	Light Detection And Ranging
IR	Infrared
LRS	Laser Range Scanner
GUI	Graphical User Interface
GNSS	Global Navigation Satellite System
SLAM	Simultaneous Location And Mapping
COTS	Commercially Off The Shelf
USB	Universal Serial Bus
FOV	Field OF View
CDC	Communication Device Class
TOF	Time Of Flight
PSTOF	Phase Shift Time Of Flight
DOF	Degrees Of Freedom
CP	Control Points
NCP	Non Control Points
LF	Line Feed
CR	Carriage Return

Declaration and Consent

Details of the Work

I hereby agree to deposit the following item in the digital repository maintained by Bangor University and/or in any other repository authorized for use by Bangor University.

Author Name: …Mark Anthony Fisher……..

Title: Integrated Sensor Suite for Indoor Building Inspection with an Unmanned Aerial Vehicle

Supervisor/Department: .....Dr Iestyn Pierce and Dr Sa'ad Mansoor.....

Funding body (if any): .....KESS , Bangor University and GWERF Cyf.....

Qualification/Degree obtained: …….PhD……..

This item is a product of my own research endeavours and is covered by the agreement below in which the item is referred to as "the Work". It is identical in content to that deposited in the Library, subject to point 4 below.

Non-exclusive Rights

Rights granted to the digital repository through this agreement are entirely non-exclusive. I am free to publish the Work in its present version or future versions elsewhere.

I agree that Bangor University may electronically store, copy or translate the Work to any approved medium or format for the purpose of future preservation and accessibility. Bangor University is not under any obligation to reproduce or display the Work in the same formats or resolutions in which it was originally deposited.

Bangor University Digital Repository

I understand that work deposited in the digital repository will be accessible to a wide variety of people and institutions, including automated agents and search engines via the World Wide Web.

I understand that once the Work is deposited, the item and its metadata may be incorporated into public access catalogues or services, national databases of electronic theses and dissertations such as the British Library's EThOS or any service provided by the National Library of Wales.

I understand that the Work may be made available via the National Library of Wales Online Electronic Theses Service under the declared terms and conditions of use (http://www.llgc.org.uk/index.php?id=4676). I agree that as part of this service the National Library of Wales may electronically store, copy or convert the Work to any approved medium or format for the purpose of future preservation and accessibility. The National Library of Wales is not under any obligation to reproduce or display the Work in the same formats or resolutions in which it was originally deposited.

Statement 1:

This work has not previously been accepted in substance for any degree and is not being concurrently submitted in candidature for any degree unless as agreed by the University for approved dual awards.

Signed …….. (candidate)

Date ……..

Statement 2:

This thesis is the result of my own investigations, except where otherwise stated. Where correction services have been used, the extent and nature of the correction is clearly marked in a footnote(s).

All other sources are acknowledged by footnotes and/or a bibliography.

Signed …….. (candidate)

Date ……..

Statement 3:

I hereby give consent for my thesis, if accepted, to be available for photocopying, for inter-library loan and for electronic storage (subject to any constraints as defined in statement 4), and for the title and summary to be made available to outside organisations.

Signed …….. (candidate)

Date ……..

NB: Candidates on whose behalf a bar on access has been approved by the Academic Registry should use the following version of **Statement 3:**

Statement 3 (bar):

I hereby give consent for my thesis, if accepted, to be available for photocopying, for inter-library loans and for electronic storage (subject to any constraints as defined in statement 4), after expiry of a bar on access.

Signed …… (candidate)

Date ……

<u>Statement 4</u>:

Choose **<u>one</u>** of the following options

a)	I agree to deposit an electronic copy of my thesis (the Work) in the Bangor University (BU) Institutional Digital Repository, the British Library ETHOS system, and/or in any other repository authorized for use by Bangor University and where necessary have gained the required permissions for the use of third party material.	
b)	I agree to deposit an electronic copy of my thesis (the Work) in the Bangor University (BU) Institutional Digital Repository, the British Library ETHOS system, and/or in any other repository authorized for use by Bangor University when the approved **bar on access** has been lifted.	
c)	I agree to submit my thesis (the Work) electronically via Bangor University's e-submission system, however I **opt-out** of the electronic deposit to the Bangor University (BU) Institutional Digital Repository, the British Library ETHOS system, and/or in any other repository authorized for use by Bangor University, due to lack of permissions for use of third party material.	

Options B should only be used if a bar on access has been approved by the University.

In addition to the above I also agree to the following:

1. That I am the author or have the authority of the author(s) to make this agreement and do hereby give Bangor University the right to make available the Work in the way described above.

2. That the electronic copy of the Work deposited in the digital repository and covered by this agreement, is identical in content to the paper copy of the Work deposited in the Bangor University Library, subject to point 4 below.

3. That I have exercised reasonable care to ensure that the Work is original and, to the best of my knowledge, does not breach any laws – including those relating to defamation, libel and copyright.

4. That I have, in instances where the intellectual property of other authors or copyright holders is included in the Work, and where appropriate, gained explicit permission for the inclusion of that material in the Work, and in the electronic form of the Work as accessed through the open access digital repository, *or* that I have identified and removed that material for which adequate and appropriate permission has not been obtained and which will be inaccessible via the digital repository.

5. That Bangor University does not hold any obligation to take legal action on behalf of the Depositor, or other rights holders, in the event of a breach of intellectual property rights, or any other right, in the material deposited.

6. That I will indemnify and keep indemnified Bangor University and the National Library of Wales from and against any loss, liability, claim or damage, including without limitation any related legal fees and court costs (on a full indemnity bases), related to any breach by myself of any term of this agreement.

Signature: …… Date : ……..

Acknowledgements

I would like to thank Dr Iestyn Pierce, Dr Dewi Jones and Dr Sa'ad Mansoor for all the encouragement, advice and support with all areas of this PhD project.

Thanks are also definitely deserved to my family, with a special mention to Gill, Sam and Jac for keeping me going.

Thanks also go to my friends in Dean Street.

This research was funded by a Knowledge Economy Skills Scholarship (KESS), with contributions from the European Social Fund (ESF), Bangor University and GWERF Cyf.

Chapter 1 Introduction

Introduction

Large buildings require maintenance plans in order to reduce the risk of serious structural failures. In order to assess and evaluate these buildings there is a need for a detailed and accurate inspection method. The current method for performing an indoor building inspection is flawed and is compounded when applied to large buildings such as warehouses, factories, stations and other civic buildings. The current method has four main areas: how to gain access, how to gather the data, how to process the data into information and how to store and display the information for the end user. An evaluation of the main arguments in Chapter 2 shows that there are viable alternatives to perform the current building inspection methods.

The thesis describes the investigation into the use of an unmanned aerial vehicle to provide an alternative method for accessing high and enclosed areas while using an on board sensor suite to gather physical dimensions and visual data.

Thesis Overview

Motivation

The motivation for this research was set by a local company Gwefr Cyf, to research into a small electronic payload mounted on an electrically driven UAV (Unmanned Aerial Vehicle) operating inside a building.

To maintain the interior of a building, regular indoor building inspections are taken, according to a building maintenance plan. These inspections are performed by qualified civil engineers and involve measuring and assessing the condition of various structural components. This method gives a visual and written assessment of the building's structural condition with any structural defects or faults recorded. Unfortunately several drawbacks can be noted in this method. Due to the height and size of such buildings, access can be dangerous and difficult, which makes the inspection process time-consuming and expensive. To gain access to high ceilings and enclosed spaces the engineer would

typically use Mobile Elevated Work Platforms (MEWPs). A MEWP allows the engineer to gain access to high or enclosed spaces without the need for installing and removing costly scaffolding, however the MEWP must be repositioned in each location, increasing the time spent performing the inspection. There will always be areas where the engineer is unable to inspect, such as areas where access using a MEWP or scaffolding is not possible, reducing the coverage of the inspection.

An alternative method proposed would be required to find a safer and more cost-effective method of collecting data while inspecting high ceilings and walls of large buildings in enclosed spaces such as industrial warehouses, train stations etc.

This project considers an alternative method of inspection. The proposed method uses an unmanned aerial vehicle, carrying a suitable sensor suite payload which flies to the inspection area and performs the inspection. The UAV is small enough to manoeuvre inside a large building to perform the inspection and navigate obstacles such as roof beams etc, and to examine enclosed areas.

Aims

The aim of this research is to create for the purpose of internal building inspection a sensor suite payload for a small, electrically-powered unmanned aerial vehicle (UAV).

The payload will be :-

1. Lightweight, less than 1Kg
2. Small size to allow access to enclosed areas
3. Integrated multi-modal sensor suite
4. Suitable for mounting onto a UAV to allow for high access inspection

The payload will be able to :-

1. Visually observe defect indicators such as signs of rust and corrosion, deformation or cracking
2. Measure physical structural dimensions
3. Operate at a range of less than 5m
4. Record images for photogrammetric analysis

The system should be suitably tested to ensure that it meets the aims set out above using a suitably designed test rig.

Structure of the Thesis

Chapter 2 describes the background of the project. A review of the literature for a similar method used for external building inspections and possible alternative methods for conducting indoor building inspections is presented. Based on this review, a method is selected for gathering data from a sensor suite mounted on a UAV for indoor building inspections.

Chapter 3 describes how position and orientation can be represented and from this a suitable method is chosen.

Chapter 4 describes a selection of laser range scanner methods that can be used to gather range data from a scene and their mathematical descriptions. The requirements of the UAV system are also reviewed which leads to comparison of currently available laser range scanning devices. The selection of a suitable device is then discussed.

Chapter 5 discusses the method for processing the 2D range scans gathered from the laser range finder into a 3D point cloud. The programs that process the 2D and 3D data and the results are discussed.

Chapter 6 describes the first test rig constructed for the project and used to simulate the UAV in order to perform experiments to test the laser range scanner, camera and the ability to produce three dimensional point clouds and images. The first test rig is tested to see if it was suitable for use, and its results presented.

Chapter 7 describes the second test rig constructed for the project and used to simulate the UAV in order to perform experiments to test the laser range scanner, camera and the ability to produce three dimensional point clouds and images. The second test rig is tested to see if it was suitable for use, and its results presented.

Chapter 8 describes how the gathered visual and range data gathered by the sensor suite is used to allow the user access to both the physical dimensions and the visual images gathered by the UAV on one consistent and useful representation. The chapter discusses the types of transforms used to create this data representation and experimentally tests them. The results from these tests are presented.

Chapter 9 shows experimental results from testing the laser range scanner on different coloured targets and also real world targets typically seen while performing an indoor building inspection.

Chapter 10 discusses the work in this thesis and assessed the extent to which the aims set out in chapter 1 have been satisfied. Conclusions are drawn and a discussion of how the project can be developed in the future is discussed.

Contributions

The research in this thesis has made the following contributions,

- Design and evaluation of a test rig to simulate the movement of the UAV and its mounted sensor suite in chapter 6 and chapter 7
- Chapter 5 describes a novel mathematical model to convert 2 dimensional range scans from the URG-04LX into 3- dimensional range scans. This model takes into account the position and orientation of the UAV and sensor suite on which the URG-04LX is mounted
- Chapter 8 shows a method to create a fused data set from range data and a visual image.
- Chapter 8 shows a method to allow the user to select points from this fused data set and calculate simple distance values
- Chapter 9 the results of the experiments required to assess the suitability and viability of performing indoor building inspection using a UAV and suitable sensor suite
- Chapter 10 contains the conclusions and future work

Chapter 2 Literature Review

This chapter is divided into two sections. The first section discusses a current method for external building inspection on which internal building inspection can be based. The second section reviews alternative methods of gathering data, and deploying sensors for an indoor building inspection.

2.1 Highways Agency Inspection Method

This section reviews the Highways Agency Inspection method which is used by the UK Highways Agency for assess structures for defects that can cause structural faults. As this method deals mainly with external structures it can be used as a reference to understand what an indoor building inspection can look for and the types of defects that may appear on structures. A review of the Highways Agency inspection method highlights the limitations associated with this method if it is applied to performing indoor building inspections, specifically looking at how high and enclosed areas are inspected.

2.1.1 Description of the Highways Agency Inspection Method

To understand how and why building inspections are undertaken, a defined inspection method used by the highways agency was provided by the project's partner company as a reference[1]. The highways agency inspection process is broken down into five elements: Scheduling; Planning and Preparation; Perform Inspections; Record and Report; and Input to Maintenance Planning Process[1].

2.1.2 Scheduling

Scheduling provides information and guidance about when to implement inspections and what needs to be considered before an inspection is scheduled. This element defines how to choose the type of inspection required. There are many types of specific inspection that are undertaken, and external building inspections can be generally be broken down into six types of inspection : Safety Inspection/ Routine Surveillance, General Inspection, Principal Inspection, Special Inspection,

Acceptance Inspection and Inspection for Assessment[1]. Table 1 shows a brief description of each type of inspection and the nominal interval between inspections.

Inspection Type	Nominal Interval	Description
Safety Inspection/ Routine Surveillance	As often as to timely identify defects whilst reflecting the importance of the structure	Cursory visual inspection made on foot or in a slow moving vehicle.
General Inspection	2 Years	A visual inspection from ground level which reports the physical condition of structural elements visible from the ground.
Principal Inspection	6 Years	Close visual inspection which utilises the suitable and necessary inspection techniques. It reports on all inspectable structural areas.
Special Inspection	When required or programmed	Detailed inspection of particular areas causing concern after a specific event.
Acceptance Inspection	When required	A formal inspection for exchanging information before a change of responsibility of the structure.
Inspection for Assessment	When required	Inspection to provide information to allow for structural assessment.

Table 1 – Types of Highway Inspections [1]

2.1.3 Planning and Preparing

Planning and preparing provides the information for planning an inspection and any factors that need to be considered. This element also gives information on how to prepare for risk assessments and the methods used in the inspection. It is broken down into ten planning and

preparing sections: Method Statement; Health and Safety; Risk Assessment; Access; Equipment, Structure Records; Type of Testing; Competence of Staff; Work Notification and Environmental Impacts. Table 2 shows a brief description of each section.

Planning and Preparing Section	Description
Method Statement	A statement of method intent to be produced with reference to risk assessment.
Health and Safety	The appropriate Health and Safety analysis should be undertaken.
Risk Assessment	A risk assessment should be undertaken to reduce or avoid hazards before the work is started.
Access	How will access be obtained to inspect the structure?
Equipment	What equipment will be required for the inspection and its availability?
Structure Records	Previous records or structural diagrams, inspection etc.
Type of Testing	The types of testing undertaken in the inspection, their location and intensity with reference to health and safety.
Competence of Staff	The staff undertaking the work is suitably trained.
Work Notification	To notify other parties and if necessary gain approval to undertake the inspection.
Environmental Impacts	The work must be assessed to assess if the work will affect the public or wildlife.

Table 2 – Pre–inspection planning areas [1]

2.1.4 Performing Inspections

This section of the inspection process provides the details of performing inspections on structures and any related materials or special structures. This area is highly focussed on the type of structure being inspected, and gives the inspector instruction on how to undertake the inspection method accurately and safely. This section may list examples of the type of structures the inspector may encounter and also the type of defects associated with the structure's material. Examples of these are cracking to brickwork, corrosion of metal work, damp, subsidence, water ingress, animal infestation and smoke or fire damage. This enables the inspector to have a clear understanding of what they are inspecting and what to expect when undertaking the inspection.

2.1.5 Recording and Reporting

This section of the inspection process provides a generic process for recording and rating defects to the condition of the inspected areas. A grading scheme is used to assess an inspection area which relates to its condition in the Highways Agency inspection [1]. Another proposed method is to grade an area on a scale of 0-9 with 9 being in excellent condition and 0 being failed, beyond repair and out of service similar to that proposed by N. Hamzah et al.[2]. This provides a quantitative guide to the building's condition. Notes can be taken to aid the understanding of the assessment along with images, recordings or any other type of appropriate methods of reporting the data collected. Although not discussed directly in [1], suitable storage of this collected data also needs to be considered in this section as repeated inspections allow for a case history of the structure to be documented, which can be used to create a profile of the change in structure condition over time as shown in[3][4]. This section also details the evaluation methods for the data collected. The inspection results collect evidence to assess if the structure is fit for purpose and safe for use, and if the defects observed within the inspection are classed as serious, urgent action is triggered in order allow for corrective action and future maintenance.

2.1.6 Input to Maintenance Planning Process

This section of the inspection process provides guidance on how to incorporate the findings of the inspection report into a maintenance program in order to resolve or avoid defects. Using the data collected from inspections a profile of the structure is established and a maintenance plan devised to monitor the condition of the structure over a period of time. Using this maintenance plan

preventative and corrective work can be undertaken to ensure the continued use and safety of the structure.

2.2 Discussion of the Highways Agency Method

2.2.1 Discussion of Access Method

The process of performing a building inspection requires the inspection engineer to inspect all areas of the building. The areas that the engineer can inspect on foot can be inspected relatively easily, but for inspection above head height or in an enclosed space, a different approach shall be adopted in order to ensure the safety of the engineer and the accuracy of the inspection. The Highways Agency method uses equipment to allow engineers access to inaccessible areas and is discussed below.

The use of Mobile Elevating Work Platforms (MEWP) is a method of inspecting enclosed areas at height and is mentioned in [1]. An example of a MEWP is a lorry mounted telescopic machine which provides a working platform at variable heights. The platform can be raised or lowered as required and can be positioned below an inspection area. The inspector can then be lifted up to the area for inspection in safe working environment. An engineer enters the basket of a MEWP on site and is moved around the inspection area whilst conducting a visual assessment. This method has several problems associated with it.

An issue with using a MEWP is that it may physically be too large to fit into areas to allow an engineer access, such as enclosed areas. This means that there are areas that the engineer cannot inspect fully.

A problem with the current methods of inspection is the risks involved while working at heights. The Health and Safety Act at Work 1974 [5]requires an employer to “make further provision for securing the health, safety and welfare of persons at work, for protecting others against risks to health or safety in connection with the activities of persons at work”. Specifically the Working at Height Regulations 2005 [6] require extensive health and safety assessments, training and equipment in order to ensure that the inspection engineer is kept safe. Areas with a high risk factor require higher mitigation measures in order to protect the employee. The increase in risk means that a detailed analysis is completed on site identifying the risks and ensuring sufficient safety measures are in place to reduce the risks before any inspection can begin. However if suitable measures to reduce the risk are implemented, they may impede the ability of the inspector or the equipment to

complete the inspection. In some cases it may be impractical to implement the measures to reduce the risk of injury or the risk is deemed too great and not safe for an employee to work in. This means that certain areas of a building may not be suitable for inspection and can result in an incomplete building inspection.

Although a lack of access for a visual inspection can affect the ability to detect defects, another limitation of the current inspection method is due to the subjective nature of the inspection. The next subsection discusses the current method of performing visual inspections and highlights some of the drawbacks this method presents when performing indoor building inspections and in particular on high and enclosed areas.

2.2.2 Discussion of Issues with Inspection

Generally inspection engineers have to be qualified professionals with training and experience in detecting building defects, each engineer can have a different subjective opinion on what is considered to be a major or insignificant defect. This can lead to defects not being recorded as defects depending on the inspector's training and experience. Extensive training and preplanning are undertaken to ensure that the inspector knows what type of defects to expect and also how to correctly and accurately assess the condition of buildings. Kletz [7] discusses how these errors can be defined. Kletz defines errors into three categories; errors are made due to poor training or instruction, errors that are beyond the mental or physical ability of the person performing the task and errors in not following a specific instruction or accepted practice.

The repetitive task of visually assessing similar areas can lead to defects being missed due to a lack of concentration by the inspector due to a lack of external stimuli. This error is classed by Kletz as being beyond the mental capability of the person, due to the inability to sustain a high level of concentration for an extended period of time. A different example of this is a sonar watchmen in Second World War ships as described in [8]. The sonar watchman is a highly skilled and important job aboard a ship. To aid the sonar watchman they are given a very comfortable seat to sit in, a quiet environment to work in and dimmed lights in order to help the watchman concentrate and observe the sonar screen. Even with a highly skilled professional with comfortable surroundings on the ship the sonar watchman is found asleep an alarming number of times. As there are no external stimuli in the cosy, dark room the sonar watchman with all the good intent cannot concentrate on the same task for long periods of time without becoming bored or falling asleep. Similar conditions are encountered when conducting an inspection. The inspector is working by himself in poorly lit areas repeating a task over a large period of time. McRobbie [8] argues that defects are inevitably be

missed due to the lack of external stimuli to keep their concentration focussed on the task at hand. The fact that the engineer's judgement can be impaired may then lead to structural defects being missed.

A final problem with using the same engineer to repeatedly assess a building over a period of time can lead to the inspector making assumptions before the inspector have even seen the current state of the building as discussed by McRobbie [8] based on work by Estes [9]. This expectation of results can influence the outcome of the structural assessment without the engineer realising and important defects can be missed and minor defects can be made unduly important if they are not expected.

The access limitations of the Highways Agency inspection method do not allow the engineer to carry out a full inspection of an enclosed high space, as the access and inspection methods used by [1] are not specifically designed to deal with high and enclosed areas whilst performing an indoor building inspection. There is clearly a limitation to the Highways Agency's method when applied to indoor building inspections. From the review of the Highways Agency's method [1]for performing building inspections comparisons can be drawn to that of performing an indoor building inspection. The Highways Agency method is therefore not suitable for performing indoor building inspections due to the indoor working access issue, inspection engineers' subjectivity and fallibility in repetitive work.

2.2.3 Conclusions about Limitations of using the Highways Agency Inspection Method

Using the Highways Agency inspection method as an example for performing inspections parallels can be drawn for use in indoor building inspections. An indoor inspection requires inspections to be made at regular intervals, with methodical planning and preparation being put in place to allow for detailed inspections. These inspections are recorded and reports on the condition of the building prepared, which allow the end users to take appropriate remedial action. It can be seen from the Highways inspection method that any inspection process is a large undertaking and has different critical areas which need to be performed to gather information from which a buildings condition can be evaluated.

The aim of this research is to look at an alternative method to provide indoor building inspections whilst overcoming the limitations the Highways Agency method[1]. In the next section alternative inspection methods and access methods of access and inspection methods are discussed.

From these discussions and measured against the aims in chapter 1 a suitable inspection method is selected in order to provide indoor building inspections.

2.3 Alternative Inspection Methods

Several alternative inspection methods for indoor building inspection are described in this section. They are broken down into two categories, Sensor Types and Alternative Deployment Methods. The inspection methods is discussed in this section and compared to other inspection methods.

2.3.1 Remote Scene Reconstruction

Alternative solutions for gathering data currently exist and are used in different applications. This section will show some of the current methods for gathering data via a robot.

An example of a robot gathering data from a difficult to reach areas was seen in [10] where a robot for under floor inspection of a house was developed. Ohya, A et al. explains that the work being undertaken for inspecting Japanese house under floor areas is tough due to the size restraints of the building. The paper proposed using a crawling robot fitted with a camera and LRS to record information about the condition of the concrete foundations of the house. The work showed an interesting alternative approach to documenting the condition of building defects in hard to reach areas, as the system is remotely controlled by a human. The work by Ohya, A et al. showed that it is possible to document building defects in difficult to reach areas using remote robotic methods.

Work done by Abderrahim, M et al. [11] uses a similar approach to automate bridge inspection, but there is not a size limitations of the area being inspected, but due to safety concerns of the human performing the bridge inspection. As bridges are generally high above the ground, the risk of injuring is increased when compared to performing an inspection at ground level. To overcome this Abderrahim, M et al. developed ROMA, to perform bridge inspections. The ROMA robot used two grippers to enable it to climb the bridges and perform visual inspections using a camera. The recorded data is then sent back to the operators for analysis. The work done by Abderrahim, M et al. showed that in high risk environments robots can be used to gather data instead of human inspectors.

Both of the previous two methods for gathering data have primarily used cameras for data collection. The work done by Montemerlo, M and Thrun,S presented an alternative method for

remote scene reconstruction using LIDAR called Segbot. Using a Segway mounted with a SICKLMS200 data was recorded from urban environments. The LIDAR produced a 3D point cloud of the environment it scanned which used a localisation algorithm to allow it to record the position it recorded the data from. The 3D point cloud data collected was then processed into a mesh which detailed the surface of the environment allowing the user to view the urban environment remotely. The use of LIDAR to gather data it allowed the Segbot to build up a data set describing the position and orientation of urban environment relative to itself and a world coordinate system. The Segbot could be considered as an alternative for building inspection instead of a human, as can gather 3D data from a building using the LIDAR.

2.4 Sensor Types

This section focuses on the types of sensors which can be deployed to gather data for an indoor building inspection. The types of inspection performed can be described as either destructive testing or non-destructive testing and examples of each can be seen in Table E.2 in the Highways Agency Inspection Manual [1]. Destructive testing refers to the object being tested to the point of failure such as Breakout and Coring or partial demolition. Non-destructive testing is described in [12] as “Techniques that are based on the application of physical principles employed for the purpose of determining the characteristics of materials or components of systems and for detecting and assessing the inhomogeneities and harmful defects without impairing the usefulness of such materials or components or systems.” An example of this would be surveys, thermography or endoscopic investigation. This research is interested in observing, measuring and monitoring the state of a building using indoor building inspections using non-destructive testing rather than testing the structure to destruction.

2.4.1 Camera for Visual Information

The Highways Agency [1] use cameras to gather visual information while performing inspections. A camera is a device that creates a single image of a target and records it on a medium by allowing light to enter an enclosed box and pass through a lens. The image is recorded on a light sensitive medium. The next two subsections focus on two types of digital recording medium for storing visual data.

- CMOS
- CCD

2.4.2 CMOS

The CMOS light sensor in a camera has a light sensitive medium which is divided up into small areas called pixels. Each individual CMOS pixel has circuitry that converts the level of light energy into a voltage, which is then read from the circuitry. The voltage can then be converted into a digital representation. CMOS technology uses less power than Charge Coupled Devices (CCD) technology and due to the nature of its construction CMOS device tend to be cheaper to produce than CCD [13][14].

2.4.3 CCD

The light sensitive medium is divided up into small areas called pixels. Each CCD pixel uses a capacitor to convert the charge into a voltage which is read off from an output node. In order to get the voltages to the output node the CCD chip sequentially transports the voltage across the chip to the node. CCD devices produce “high-quality low noise images” [14] compared to CMOS devices which can be more susceptible to noise [14][13].

2.4.4 Light Detection And Ranging (LIDAR)

An alternative system than the current method used by the Highways Agency [1] is to gather physical dimensions using a LIDAR system. A LIDAR range scanner is a device that measures the distance a target is away from the device by emitting pulses of light towards the target. The distance from the LIDAR scanner to the target is determined by the time taken for the emitted pulse of light to reflect from the target and be detected by the optics in the scanner. The time taken for the round trip of the light is converted into an electrical signal proportional to the range value. Once a number of samples are taken, the samples of the electrical signal can then processed into a suitable visual representation such as a point cloud. Using computer aided design software a 3D model of the scanned target such as those seen in [15] can be made. A LIDAR range scanner such as the URG-04LX or SICK LMS both described below can be suitably mounted, deployed quickly, with an operating

range from meters to kilometres [16]–[20] and have scan times that range from tens of milliseconds as seen in the SICK LMS200 [21] to hundreds of milliseconds as seen in the URG-04LX [17] with typical accuracies better than 1cm [17][18] [21].

An advantage of using a typical LIDAR for indoor building inspections is that the device can scan large areas quickly and accurately without physical contact. This can increase the speed at which a survey is completed. A problem with using larger LIDAR range scanners is that they require space for a suitable stand to be set up in. This is an issue if trying to scan areas that are above head height, as the LIDAR requires a platform to be set up on in order to scan. A current method used by the Highway agency to inspect areas above head height is to use a MEWP[1]. As one of the aims outlined in chapter 1 is to develop a system to work within confined spaces, the size of MEWP can be too large to allow the LIDAR unit access to enclosed areas. This can result in incomplete inspections due to the size and position of the MEWP preventing certain areas from being surveyed.

Smaller LIDAR units are used in robotic applications [10], [22], [23] and are relatively lightweight and small, such as the Hokuyo URG-04LX [24] whilst still providing the same functionality as the larger devices. The main features when comparing LIDARs are the accuracy, range, size, weight, power consumption and cost of the device.

A comparison of two LIDARs is undertaken by [25] and shows that the accuracy of the small LIDARs compared is around 10-20mm, and that different materials have different effects on this accuracy.

The work done in [26] shows the development of a small laser range scanner. It has a high accuracy of ±10mm, a 4m operating range, a compact 70mm x 50 mm size, having a light weight of 170g with low power requirements 5V and 500mA.

LIDAR scanners can have their raw data processed to produce a point cloud of the data scanned, this can be used to create a 3D model which can help the user visualise the output of the building inspection and also detect defects.

A disadvantage of using a LIDAR scanner is that the data collected by the device requires post processing before presenting the information to the end user. This may require an external company or trained individual to analyse the data collected which can also increase inspection costs.

2.4.5 Structured Lighting

Projecting a narrow band of light onto a 3D object will produce a line pattern on the 3D object, the surface changes of the 3D object distort the line of illumination when observed from different perspective than that of the source of the illumination. To create a distinct light when surrounded by ambient light a visible red laser or infrared laser is used [27] and by observing the distortions of the

illumination geometric data can be reconstructed from the 3D object. Some currently commercial products that use structured light are the Dave Laserscanner SLS2 [28], NextEngine [29]or the Artec Eva [30] to list a few.
The generation of the light pattern can generally be categorised into two sections

Projected
The projection method uses non-coherent light to display the line pattern onto a 3D object, in a similar way to a projector. The line pattern is limited to the size of the pixels and also to the camera optics. Therefore a high amount of pixels on the projectors display and the ability to focus the light are highly desirable.

Laser Interference
The laser interference method uses planar laser beams to create a regular interference pattern of equidistant line patterns. Different pattern sizes can be created by changing the angle between the laser beams. As the pattern size can be adjusted to fit the nature of the 3D object being scanned the laser interference offers a wide ranged depth of field.
A disadvantage is the high cost required to maintain the level of accuracy over the lasers[27]. The amount of Speckle noise and potential self-interference with laser beams reflected from 3D objects also presents a problem when using this method of light pattern generation[27].

One of the major challenges of using this method is that reflective, transparent and semi-transparent surfaces cause the light pattern to be either reflected away from the optics or directly back into the optics from where it was emitted. A simple solution to overcome this problem would be to place a thin no reflective surface over the 3D object being scanned, but in some situations this would not be practical, such as working at height or in small and enclosed areas where allow access to humans is not practicable.

2.4.6 Photogrammetry

Photogrammetry allows the reconstruction of an object and the analysis of its characteristics without physical contact with it [31]. For the scope of this project gathering data in the form of visual images so that visual assessments of the object can be undertaken as well as gathering its physical dimensions as stated in the aims in Chapter 1 is a requirement. To use photogrammetry an image of the target is taken with a camera, the distance between two points of interest on a plane parallel to

the photographic image plane can then be determined. This is achieved by measuring the distance between the points of interest on the image. The requirement for this method is that there is an object in the visual image that has known physical dimensions. The physical dimensions of the known object in the image allow the calculation of scale of the image, and from those other distance measurements can be gathered.

Three dimensional (3D) data can be created using Stereophotogrammetry [31] which uses multiple overlapping images which are been taken from different positions around the target. Common points in each of these images are identified on each individual image. Using these common points an imaginary line of sight can be drawn from the camera to the target object. For this method to work requires multiple images of the target from different positions, which create at least two or more lines of sight. Where these lines of sight intersect with each other it allows for triangulations, this in turn allows for a 3D coordinate system to describe the location of the target object.

The multiple lines of sight may give the position of the point of interest on the object. If the geometric measurements of two different points are required from multiple images then known dimensions are required of part of an image usually common to several images taken at different positions. Once there is a suitable reference to an object's size within the images other dimensions of different targets can be calculated by scaling the known size in one image with the target image.

2.4.7 Structure from Motion

Structure from motion is photogrammetric method to determine the depth of an object from a series of images taken by multiple cameras at different perspectives.
Structure from motion uses the same basic principles as stereoscopic photogrammetry, in which depth can be resolved from a series of overlapping offset images. It differs from conventionally photogrammetry as camera positions, geometry of the target scene and orientation are solved without any need to specify a network of targets which have known 3D positions[32]. Camera pose and scene geometry can be reconstructed using feature tracking in multiple images. To do this the images are collated together and a feature detection algorithm is used to find corresponding points within the images. Two examples of such feature detectors are SURF (Speeded Up Robust Features) and SIFT (Scale Invariant Feature transform). The features that are tracked from one image to another allow for estimates of the position of the camera and object coordinates. To remove any

incorrectly matched images a RANSAC (Random Sample Consensus) to remove outlying images. The camera positions and object coordinates are then refined iteratively using non-linear minimisation [32].

As structure from motion does not require a known control point to generate the camera position the data it produces lacks the scale and orientation provided by known control points. The 3D point clouds generated are relative to the image space coordinate system, which must be aligned to a real world object space coordinate system[32]. To transform the image space coordinate system into a real world system known control points must be used as a reference. If such control points are not available or if the area for inspection is difficult to reach and gathering multiple visual images from different positions can be difficult to achieve. If these known control points and images cannot be gathered then structure from motion would not be an effective way to gather range data.

An advantage of using photogrammetric methods to estimate geometric values compared to that used by the Highways Agency which requires the engineer to physically measure the target is that it is a very quick method of capturing the required images using cameras. An object or area can be relatively quickly photographed by a relatively un-skilled camera operator, as the requirements are that there need to be several photographs and they need to share some common points. Another advantage of this method in that the images of the target object can also be suitably archived for future reference, comparisons and suitable maintenance plans. A disadvantage with photogrammetry is that it needs several common points within multiple images. If the area for inspection is also difficult to reach gathering multiple visual images from different position can be difficult to achieve. This method is non-destructive as a camera is used to gather data without any need to interact physically with the target. This means that as long as the person taking the photographs can see the object in the camera's view finder then the object can be visually assessed without any invasive procedures. Another advantage of this method is that part of the accuracy of the photogrammetric analysis is determined by the resolution of the camera that the images are captured on[33]. The higher the resolution of the camera the better the chance of achieving a high accuracy as the objects can be located in the image more precisely.
Technological developments allow commercially available cameras to have higher pixel resolutions at a lower cost, which has enabled commercially available cameras to be used to gather images accurately.
A problem with photogrammetric analysis of any kind is the amount of lighting available when the images are captured. The amount of light can affect what the user can see in the image when

looking for defects in the object. If a typical camera flash is used it may cast shadows on the images which may occlude certain areas from visual analysis, which can result in defects that are in shadows being overlooked when visual analysis is performed on the images. The only way to overcome this problem is to have suitable lighting that is portable and can be set up to create a situation in which the target object is fully illuminated. This can then limit the use of this method to users who are trained to set up the lighting of the object so as to avoid the problems previously mentioned.

If this method is also to be used for indoor building inspection then again the problems of access to enclosed space are considered. The Highways inspection method shows how it suffers from the inability of the inspector to access enclosed spaces. Increasing the amount of lighting equipment to overcome the lighting problem may further compound the difficulty in accessing enclosed spaces.

2.4.8 RGB-D Sensor

RGB-D sensors use cameras to gather RGB images, and also a depth sensor to gather individual pixel depth data. The RGB-D sensor uses either time of flight sensing or active stereo sensing to estimate the depth of a large number of pixels.

A time of flight sensor resolves the distance to a target by measuring the amount of time of flight of an emitted light signal between the sensor and a target. By knowing the speed of light and the time taken for it to reflect off the target and be detected by the sensor the distance can be measured. The principles of time of flight sensors are discussed in Chapter 4.

Stereo sensing uses two cameras with known physical relationships, such as how far apart in physical space their focal points are and their base line optical axis positions for example. Mapping common pixel values and calculating how far apart the common areas are in pixel space provides the user with a depth map, similar to human vision. The principles of triangulation are discussed in Chapter 4. One problem using stereo sensing is finding a set of corresponding points in both cameras. This is known as the correspondence problem and limits the stereo sensing to create depth maps of corresponding points only.

The RGB-D sensor produces dense depth estimates, but a drawback is the amount of noise that is produced with the depth estimates and the limited field of view ($\sim 60^{\circ}$) [34]. It is also shown by Henry et al.[34] that RGB-D sensors are not as robust at collecting 3D point cloud data and have a

depth estimation precision of 3cm at a range of 3m[34].It can also be seen that the power consumption of these devices becomes prohibitive for mobile use as shown in the commercially available SR4000 [35]. An example of an RGB-D sensor used in a domestic setting is an Xbox Kinect. The first generation Kinect was released in November 2010 and allowed users to interact with the Xbox 360 games console. By measuring the body position and hand gestures of the user they could perform in game actions and control on screen characters[36][37]. In 2014 a second version of the Kinect was released for the Xbox One which featured an increased FOV, 1080p digital camera, ability to track gestures made with an Xbox controller and can also track up to six people shaped objects at once[38].

2.5 Current Inspection method vs. LIDAR and Photogrammetry

After discussing several alternative sensor types, a comparison between the alternative methods and also the current inspection method is shown in Table 3.

Current Inspection	LIDAR	Photogrammetry	RGB-D Sensor
Health and safety concerns	Remotely operated	Remotely operated	Remotely operated
Requires lighting equipment to perform inspection	Can operate in the dark	Requires lighting equipment to perform inspection	Dependant on method of sensing if extra lighting is required
Needs to physically touch an object to measure it	No need to physically touch the object to measure it	No need to physically touch the object to measure it	No need to physically touch the object to measure it
Accurate as long as it can be measured by an inspector. Also prone to inspector errors	Accurate up to mms [25]	Accurate up to mms using commercially available cameras [39]	Accurate up to cm's [34]
Data is collected by highly trained engineers	Data can be gathered by non-skilled user	Data can be gathered by non-skilled user	Data can be gathered by non-skilled user

Table 3 – Comparison of Current and alternative inspection methods

All four of the methods shown above have advantages and disadvantages concerning their suitability for use in an indoor building inspection system. All four methods have similar deployment speeds as they use similar high access methods. The current method requires a qualified engineer to gather the data, which both LIDAR, RGB-D sensor and photogrammetry do not. One major drawback with all three methods is their inability to manoeuvre themselves remotely into suitable positions from which to gather inspection data from high and enclosed areas.

As one of the aims of this research is to find alternative methods to deploy a sensor to gather the indoor building inspection data ease of access is taken into account when selecting suitable sensors for the sensor suite. If an engineer requires access to high and enclosed areas, it requires more time and attention being paid to ensure that the health and safety of the engineer is ensured. If after reviewing the possible threats to the trained engineers health and safety and the inspection is deemed too dangerous then the inspection cannot be undertaken. If the LIDAR and photogrammetry systems can be remotely operated without the need for any engineer it negates the need for the engineer to be in the risky and dangerous environment and allow the inspection to continue unimpeded.

A LIDAR or RGB-D sensor that uses an IR light source has a clear advantage of the current method and photogrammetry as it can operate in the dark and means that no other lighting equipment is needed to gather range data for an inspection. Another advantage with LIDAR, RGB-D and photogrammetry is that they physically don't have to touch the object to be measured unlike the trained engineer. This can be advantageous in certain enclosed situations where access is restricted, as data can still be collected without the requirement to physically touch the object. A flaw with the current method of human inspection is that the trained engineer can become "bored" with the repetitive and sometimes monotonous task of visually inspecting a large area and make errors as discussed in subsection 2.1.6. This specific "bored" problem does not affect the LIDAR and photogrammetry methods for gathering data as they can gather and store large sections of data automatically. This can allow the trained engineer to view the gathered data at a later date, and through the use of appropriate rest periods, conduct accurate analysis. An issue with photogrammetry and RGB-D sensors are that they also needs several common points within several images to calculate distance successfully. This can be an issue if there are not several common points between the images. The two last points in Table 3 shows that the Highways Agency method requires a higher amount of skilled workers to gather and analyse the data collected from the inspection. LIDAR, RGB-D sensors or photogrammetry can be deployed to collect the data by a "non-skilled" person, and then the data collected evaluated by a trained engineer at a later date. The

LIDAR and photogrammetry methods also have large scanning areas which can increase the speed at which the data is gathered.

2.5.1 Conclusion

LIDAR, RGB-D sensors and photogrammetry are discussed above and have the potential to gather inspection data accurately and quickly, when compared to the Highways Agency inspection method.

LIDAR, RGB-D sensors and photogrammetry can gather the data remotely without the need for physical contact with the target. This is advantageous where engineer access is not possible, such as high, enclosed or dangerous areas. The advantage that LIDAR, RGB-D sensors and photogrammetry has over the current inspection method is that the system is automated, reducing the possibility of user error associated with humans. The level of automation and speed at which the data can be gathered by LIDAR, RGB-D sensors and photogrammetry is greater than the current method, reducing the amount of time spent in the field gathering and storing data. An area in which the LIDAR is different to the other two methods is that it does not require lights to gather data as it works in the infrared frequency. This advantage may be useful if the areas being inspected had low light levels, enclosed and or high which can make it difficult to use external lights. Another point that is considered is how to get the alternative data gathering methods to access to high and or enclosed areas.

However the increased functionality of the alternative methods by themselves does not offer enough of an advantage to outweigh the current inspection method as it doesn't address the problems associated with how to inspect difficult to reach, high or enclosed areas.

An alternative to any one of the methods proposed is to use data fusion to show multisensory data. The use of multisensory data fusion is not a new idea, as humans and animals have evolved to perform this ability in order to survive. An example of this multisensory ability being commonly used is to detect possible dangers. The danger may not be visible, but the smell or sounds that the danger makes, allows for some evaluation of the possible danger. Data fusion has been researched by others such as S. Gernhardt et al.[40], D. Klimentjew and J. Zhang [41]and by Hall and Llinas[42] who define it as "Techniques that combine data from multiple sensors, and related information from associated databases, to achieve improved accuracies and more specific inferences than could be achieved by the use of a single sensor alone".

In [41] it shows that data fusion is used to gather both range data from the Laser Range Scanner LRS and also photographic images from a camera. The data from both of the sensors is then fused to create a data set that is more useful than each individual set.

Multisensory data fusion can analyse both the physical dimensions and the visual images gathered by the UAV in one representation. A graphical user interface (GUI) can then allow the user to view the visual image and highlight areas of visual defect, whilst allowing the user to gather physical dimensions from the point cloud by selecting the areas of interest of the visual image.

2.6 Alternative Deployment Methods

Developments in electronics such as brushless motors have allowed designers to create new robotic devices that can have decreased size and power consumptions, reduced cost. Robots can be designed to be relatively small and highly manoeuvrable in a large variety of environments, a suitable replacement for the current method of indoor building inspection may be possible using robots. The aim is to mount a suitable sensor suite on a robot that can be positioned on to any part of an indoor building and then use the robot to manoeuvre the sensor suite to gather the information required.

2.6.1 Climbing Robots

One method of positioning a sensor in a high place or inspecting is to use a climbing robot. These robots use several different method of locomotion in order to climb up the walls of a structure. These types of robots are used in industry for many different tasks that range from underground building inspections, bridge inspections , welding joints and vessel interior inspections [10][11][43][44]. An example of this locomotion method can be seen in [45], where a robot climbs up obstacles such as walls in order to position sensors. The Alicia systems use a pneumatic adhesion system in order to climb up non-porous materials, but in certain situations such materials may not be available to the system and so other methods of climbing without the need for pneumatic adhesion have been created[11] [43][44]. For example, the authors of [11] developed a different system that uses “grippers” to enable the robot to grab onto materials in order to climb the structure using a “caterpillar” concept. This system overcomes the need for pneumatic suction to climb a structure, but instead require so called “hard points” on which the robot can grip in order to

safely climb without the risk of falling or damaging the structure. This becomes a problem if the system is used indoors, as not all buildings have such hard points built in.

One of the main drawbacks with these methods of locomotion for deploying the sensor is that they require certain conditions in order to climb the structure. For this reason the use of these devices is limited for indoor building inspections. Another problem with this type of system is the amount of power the devices need in order to maintain their ability to climb a structure. As mentioned in both [11] and [15] cables are required in order to recharge the batteries or act as a power supply in order to keep the robots attached to the inspection area. This is a concern as the robot's intended function is to work in enclosed areas where cables may not reach or be appropriate.

2.6.2 Flying Robots

Flying robots provide a relatively stable platform from which to position sensors and conduct inspections. There are several classifications of flying robots which can generally be split into lighter than air and heavier than air aircraft, Figure 1 according to [46].

The lighter than air aircraft can then be generalised into motorised such as (blimps) and non-motorised aircraft such as (balloons). Bouabdallah et al. summaries that lighter than air aircraft can only carry very low mass payloads when miniaturised [46] and are highly susceptible to any air movement [47], making them difficult to control and for the scope of this project they provide very limited use.

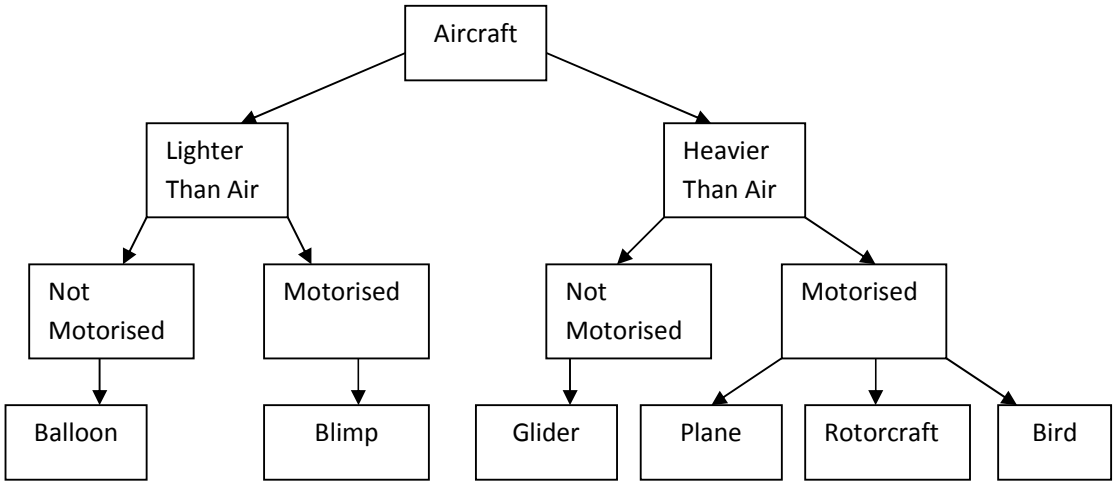

Figure 1 – Aircraft Locomotion Types [46]

Heavier than air aircraft are generalised into two main categories, motorised and non-motorised. An example of a non-motorised aircraft is a glider. These aircraft fall into a similar problem as encountered in the lighter than air aircraft. The need to launch the glider from an elevated position in order for it to fly make the use of such devices unfeasible within the scope of this project. Motorised aircraft can be subcategorised into plane, bird and, rotorcraft each representing a different method for sustaining flight[46]. The plane can describe any fixed wing aircraft that is powered by propellers or jets and has one major drawback when compared to the bird and rotorcraft methods of flight, is that it cannot reproduce vertical take-off, stationary and low speed flights easily. This drawback suggests that planes have limited use within the scope of the project. A Bird aircraft tries to copy the type of flight seen by birds and other flying animals and tend to be very small (less than 100g) and have very small payloads around 20g [48] [46]. The maximum payload the bird aircraft can carry is smaller than the sensors discussed in chapter 4. For this reason the use of bird based aircraft is also not a viable option for the scope of the project. The final classification discussed is rotorcraft. Helicopters are used for teleoperation tasks such as costal imaging as presented by [49] and also in external building inspections as shown in [50]. Quadrotors also have been used in similar situations, as described in [51]. Both types of aerial vehicle can be miniaturised and have similar payload carrying capacities, which makes both vehicle types very interesting to this research as possible alternative platforms to mount the sensor suite on in order to perform indoor building inspections in order to overcome the high access and enclosed space issues previously mentioned. The major difference between a helicopter and a quadrotor is the way in which they fly. A helicopter adjusts a the pitch of the rotor blade in order to generate thrust, horizontal force and control attitude and position[52], whereas a quadrotor changes the speed of specific motors required to manoeuvre [53]. Another difference is the size of the rotor blades used. The increased size of the rotor blades in the helicopter mean that the rotor blades store more kinetic energy as they rotate, if the rotor blades strike any object or obstacles whilst flying the impact may damage not only the helicopter but also the object. This causes a problem if the helicopter is working in a highly cluttered environment or where people are working, as the risk of injury or damage may be increased. A quadrotor has four rotors blades which are enclosed in the frame to prevent rotor blade strikes. The size of each of the rotors blades is smaller when compared to those used in a helicopter, but as there are more of them they create the same amount of lift.

There are several drawbacks to using flying robots to position the sensor, the main is the need for the robot to perform Simultaneous Localisation and Mapping (SLAM)and is defined by [54] as “the problem of building a map while at the same time localizing the robot within that map.” Before a

robot can begin to describe what the environment looks like from a set of gathered observations, it needs to know from where these observations have been made. In parallel to this, it is hard to estimate the current position of a robot without a map to reference against. SLAM can then be thought of as a chicken and egg problem because: A good map is needed for localization of the robot while accurate pose estimation is needed to build a map from the observations. As the use of Global Navigation Satellite System (GNSS) is not available to the robot indoors another solution must be used in order for the robot to know where it is in relation to its environment whilst exploring unknown and unmapped environments. There is not one uniform solution to this problem as each individual robot has unique requirements, which has lead to different ideas being developed and deployed[15][47][55][56][57] [58][59]. A method explored by P.Rudol, M.Wzorek, and P.Doherty [60] and also by G.Jang, S.Kim, W.Lee, and I.Kweon in [61] is to overcome the need for GNSS uses pre-described landmarks. Before the UAV is deployed unique landmarks are positioned in the area that the UAV is operating in. As the landmarks are placed at known positions the UAV can localise. The drawback with this method is that some prior knowledge and set up time are required in order to use this method, and also the camera needs to keep the landmarks within its vision is order to localise accurately. This can be a problem if the UAV is required to inspect areas which are enclosed and suitable landmarks cannot be deployed.

An alternative method to accurately measuring the UAVs orientation is proposed in [62]. This method uses velocity and gravitational forces, which allows an estimate of camera motion from pixel space apparent motion without explicit 3-D reconstruction. An Inertial Measurement Unit (IMU) can be used but over a period of time its accuracy is rapidly reduced due to accuracy errors [63]. The alternative method suggested in [62] to overcome this issue is to use a visual odometer which determines the position and orientation of the UAV by analysing the gathered images. The authors of [62] draw the conclusions that it can be used as an effective back up to GPS. This odometer method can be useful in a situation where there are uniquely identifiable objects that can be used in two or more consecutive images, however one of the drawbacks of this method encountered in indoor inspection is areas such as walls which may not have any of these objects available to analyse and localise accurately.

2.6.3 Discussion

The alternative sensor deployment methods of climbing and flying discussed above allow sensors to gather inspection data. When compared to the current inspection method, it can be seen

that having a sensor that can be positioned at varying heights is a big advantage while performing indoor building inspections on high and enclosed areas. The increase in speed and accuracy at which the inspection when using automated sensors is an improvement on the current inspection method as discussed above. Each alternative deployment method has advantages at positioning sensors to gather data such as being able to climb or fly to the area of interest. The disadvantages to these two alternative methods are that climbing robots require changes to the physical structure being inspected to create “hard points” and flying robots require accurate map making algorithms.

2.7 Conclusion

In section 2.1 a current practice has been reviewed and its suitability for use in indoor building inspections discussed. In section 2.3 alternative methods for gathering inspection data such as using LIDAR or photogrammetry have been investigated and discussed. From a review of the highways agency method for indoor building inspection, it has been shown that this method for gathering inspection data can be improved upon in areas by using automated sensors to remove the need to use a human inspector to be sent to physically inspect. Using LIDAR or photogrammetry instead can allow for a reduction of possible errors, an ability to operate in darkness, remote sensing and millimetre accuracy. From the review of the literature, performing indoor building inspections using remote sensors is a viable alternative to the Highways Agency method of using trained engineers. An area which has been highlighted as an area for investigation in chapter 1 has been that of how to access high and enclosed areas. Several alternative solutions have been presented.

It has also been seen that both LIDAR and cameras can be used to gather large amounts of data quickly and accurately and are an improvement on the current method of inspection. To gather data for the inspection a suitable sensor suite shall be created using LIDAR and cameras. In chapter 4 a specification is defined to allow for suitable sensors to be selected to operate in the sensor suite.

It has been decided that, flying robots are the best alternative deployment method, as they can move quickly and access high and enclosed areas easier than the current method. From the literature review it has been decided that a quadrotor is to be the method of sensor suite deployment.

2.8 References

[1] Highways Agency, *Inspection Manual for Highway Structures*, vol. 1. TSO, 2007.

[2] N. Hamzah, M. Mahli, A. I. Che-Ani, M. M. Tahir, N. A. G. Abdullah, and N. M. Tawil, "The Development of a Condition Survey Protocol (CSP) 1 Matrix for Visual Building Inspection," in *The Construction , Building and Real Estate Research Conference of the Royal Institution of Chartered Surveyors*, 2010.

[3] S. Ahluwalia and T. Hegazy, "Towards A 3-D CAD System For Accurate Condition Assessment Of The Building Infrastrucutre," in *1st Annual Inter-university Symposium on Infrastructure Management (AISIM)*, 2005, no. 519, pp. 1–11.

[4] H. N. Rad and F. Khosrowshahi, "Visualisation of building maintenance through time," in *Information Visualization, 1997. Proceedings., 1997 IEEE Conference on*, 1997, pp. 308–314 ST – Visualisation of building maintenanc.

[5] UK Government, *Health and Safety at Work Act 1974*. UK Government, 1974.

[6] UK Government, *The Work at Height Regulations 2005*, no. 735. UK Government, 2005, pp. 1–20.

[7] T. Kletz, *An Engineer's View of Human Error*, Third. Institution of Chemical Engineers, 2008, pp. 4 – 6.

[8] S. McRobbie, "Automated inspection of highway structures," *Automated inspection of highway*. IHS Inc., pp. 1–31, 2008.

[9] A. Estes, "A system reliability approach to the lifetime optimization of inspection and repair of highway bridges.," Colorado, 1997.

[10] A. Ohya, S. Yuta, T. Yoshida, E. Koyanagi, T. Imai, S. Kitamura, A. Takeuchi, and T. Minamikawa, "Development of inspection robot for under floor of house," in *Robotics and Automation, 2009. ICRA '09. IEEE International Conference on*, 2009, pp. 1429–1434.

[11] M. Abderrahim, C. Balaguer, A. Gimenez, J. M. Pastor, and V. M. Padron, "ROMA: a climbing robot for inspection operations," in *Robotics and Automation, 1999. Proceedings. 1999 IEEE International Conference on*, 1999, vol. 3, pp. 2303–2308 vol.3 ST – ROMA: a climbing robot for i.

[12] R. Raj, T. Jayakumar, and M. Thavasimuthu, *Practical Non-Destructive Testing*, 2nd ed. Woodhead Publishing, 2002, p. 196.

[13] A. Lustica, "CCD and CMOS image sensors in new HD cameras," in *ELMAR, 2011 Proceedings*, 2011, no. September, pp. 133 – 136.

[14] R. deGaris Doble, *The Everything Digital Photography Book*, 2nd ed. Everything Books, 2008, pp. 100 – 101.

[15] M. Montemerlo and S. Thrun, “Large Scale Robotic 3D Mapping of Urban Structures,” in *Experimental Robotics IX*, vol. 21, M. H. Ang and O. Khatib, Eds. Berlin/Heidelberg: Springer-Verlag, 2006, p. pp 141–153.

[16] M. Alwan, M. B. Wagner, G. Wasson, and P. Sheth, “Characterization of Infrared Range-Finder PBS-03JN for 2-D Mapping,” in *Proceedings of the 2005 IEEE International Conference on Robotics and Automation*, 2005, pp. 3936–3941.

[17] L. Hokuyo Automatics Co, “Scanning Laser Range Finder Documentation,” *Hokuyo Automatic LTD*, 2005. [Online]. Available: http://www.hokuyo-aut.jp/02sensor/07scanner/download/products/urg-04lx/data/URG-04LX_spec_en.pdf. [Accessed: 02-May-2010].

[18] J. W. Weingarten, G. Gruener, and R. Siegwart, “A state-of-the-art 3D sensor for robot navigation,” in *2004 IEEE/RSJ International Conference on Intelligent Robots and Systems (IROS) (IEEE Cat. No.04CH37566)*, 2004, vol. 3, pp. 2155–2160.

[19] A. Mora, K. Nagatani, K. Yoshida, and M. Chacin, “A Path Planning System based on 3D Occlusion Detection for Lunar Exploration Rovers,” in *2009 Third IEEE International Conference on Space Mission Challenges for Information Technology*, 2009, pp. 106–113.

[20] D. Malchow, J. Battaglia, R. Brubaker, and M. Ettenberg, “High speed Short Wave Infrared (SWIR) imaging and range gating cameras,” in *Thermosense XXIX, Soceity of Photo-Optical Instrumentation Engineers*, 2007, vol. 6541, pp. 654106–654106–12.

[21] SICK, “LMS200/211/221/291 Laser Measurement Systems Technical Description,” 2012. [Online]. Available: www.sick.com/group/EN/home/products/product_portfolio/laser_measurement_systems/Pages/laser_measurement_technology.aspx. [Accessed: 03-Feb-2010].

[22] S. Hussmann, D. Schauer, and B. MacDonald, “Integration of a 3D-TOF camera into an autonomous, mobile robot system,” in *Instrumentation and Measurement Technology Conference, 2009. I2MTC ’09. IEEE*, 2009, pp. 547–552 ST – Integration of a 3D–TOF camera into .

[23] H. Yoshitaka, K. Hirohiko, O. Akihisa, and Y. Shin’ichi, “Mobile Robot Localization and Mapping by Scan Matching using Laser Reflection Intensity of the SOKUIKI Sensor,” in *IEEE Industrial Electronics, IECON 2006 - 32nd Annual Conference on*, 2006, pp. 3018–3023 ST – Mobile Robot Localization and Mapp.

[24] L. Hokuyo Automatics Co, “URG-04LX Home Page.” [Online]. Available: http://www.hokuyo-aut.jp/02sensor/07scanner/urg_04lx.html. [Accessed: 03-Feb-2010].

[25] K.-H. Lee and R. Ehsani, “Comparison of two 2D laser scanners for sensing object distances, shapes, and surface patterns,” *Comput. Electron. Agric.*, vol. 60, no. 2, pp. 250–262, Mar. 2008.

[26] H. Kawata, a. Ohya, S. Yuta, W. Santosh, and T. Mori, “Development of ultra-small lightweight optical range sensor system,” in *Intelligent Robots and Systems, 2005. (IROS 2005). 2005 IEEE/RSJ International Conference on*, 2005, no. 42 50, pp. 1078–1083.

[27] S. Yi, “Active ranging system based on structured laser light image,” in *Proceedings of SICE Annual Conference 2010*, 2010, pp. 747 – 752.

[28] David, “SLS-2.” [Online]. Available: http://www.david-3d.com/en/products/sls-2. [Accessed: 15-May-2015].

[29] NextEngine, “NextEngine Scanner.” [Online]. Available: http://www.nextengine.com/products/scanner/features/accurate. [Accessed: 15-May-2015].

[30] Artec, “Artec Eva,” *Artec Group*. [Online]. Available: http://www.artec3d.com/hardware/artec-eva/. [Accessed: 15-May-2015].

[31] K. Kraus, *Photogammetry: Geometry from Images and Laser Scans*. Walter de Gruyter, 2007, pp. 2–3.

[32] M. J. Westoby, J. Brasington, N. F. Glasser, M. J. Hambrey, and J. M. Reynolds, “‘Structure-from-Motion’ photogrammetry: A low-cost, effective tool for geoscience applications,” *Geomorphology*, vol. 179, pp. 300–314, Dec. 2012.

[33] PhotoModeler, “Factors Affecting Accuracy in Photogrammetry.” [Online]. Available: http://www.photomodeler.com/kb/entry/63/. [Accessed: 15-Jan-2012].

[34] P. Henry, M. Krainin, E. Herbst, X. Ren, and D. Fox, “RGB-D Mapping: Using Depth Cameras for Dense 3D Modeling of Indoor Environments,” in *The 12th International Symposium on Experimental Robotics*, 2014, pp. 477–491.

[35] Mesa Imaging, “SR4000.” [Online]. Available: http://www.mesa-imaging.ch/products/sr4500/. [Accessed: 15-May-2015].

[36] S. Totilo, “Natal Recognizes 31 Body Parts, Uses Tenth Of Xbox 360 ‘Computing Resources,’” 2010. [Online]. Available: http://kotaku.com/5442775/natal-recognizes-31-body-parts-uses-tenth-of-xbox-360-computing-resources. [Accessed: 01-Jun-2015].

[37] B. Dudley, “E3: New info on Microsoft’s Natal -- how it works, multiplayer and PC versions,” *The Seattle Times*, 2009. [Online]. Available: http://old.seattletimes.com/html/technologybrierdudleysblog/2009296568_e3_new_info_on_microsofts_nata.html. [Accessed: 01-Jun-2015].

[38] T. O’Brien, “Microsoft’s new Kinect is official: larger field of view, HD camera, wake with voice,” *Engadget UK*, 2013. [Online]. Available: http://www.engadget.com/2013/05/21/microsofts-new-kinect-is-official/. [Accessed: 01-Jun-2015].

[39] A. Guarnieri, A. Vettore, and F. Remondino, “Photogrammetry and Ground-based Laser Scanning : Assessment of Metric Accuracy of the 3D Model of Pozzoveggiani Church,” 2004.

[40] S. Gernhardt, X. Cong, M. Eineder, S. Hinz, and R. Bamler, “Geometrical Fusion of Multitrack PS Point Clouds,” *IEEE Geosci. Remote Sens. Lett.*, vol. 9, no. 1, pp. 38–42, Jan. 2012.

[41] D. Klimentjew and J. Zhang, “Adaptive sensor-fusion of depth and color information for cognitive robotics,” in *2011 IEEE International Conference on Robotics and Biomimetics*, 2011, pp. 957–962.

[42] D. Hall and J. Llinas, “An introduction to multisensor data fusion,” *Proc. IEEE*, vol. 85, no. 1, 1997.

[43] M. Eich and T. Vogele, “Design and control of a lightweight magnetic climbing robot for vessel inspection,” *2011 19th Mediterr. Conf. Control Autom.*, pp. 1200–1205, Jun. 2011.

[44] L. P. Kalra, J. Gu, and M. Meng, “A Wall Climbing Robot for Oil Tank Inspection,” *2006 IEEE Int. Conf. Robot. Biomimetics*, pp. 1523–1528, 2006.

[45] D. Longo and G. Muscato, “The alicia3 climbing robot: A three-module robot for automatic wall inspection,” *Robot. Autom. Mag. IEEE*, vol. 13, no. 1, pp. 42–50, 2006.

[46] S. Bouabdallah, P. Murrieri, and R. Siegwart, “Design and control of an indoor micro quadrotor,” *IEEE Int. Conf. Robot. Autom. 2004. Proceedings. ICRA ’04. 2004*, pp. 4393–4398 Vol.5, 2004.

[47] B. Steder, G. Grisetti, C. Stachniss, and W. Burgard, “Visual SLAM for Flying Vehicles,” *IEEE Trans. Robot.*, vol. 24, no. 5, pp. 1088–1093, Oct. 2008.

[48] D. Prosser, T. Basrai, J. Dickert, J. Ratti, A. Crassidis, and G. Vachtsevanos, “Wing kinematics and aerodynamics of a hovering flapping Micro Aerial Vehicle,” in *2011 Aerospace Conference*, 2011, pp. 1–10.

[49] C. Delacourt, P. Allemand, M. Jaud, P. Grandjean, A. Deschamps, J. Ammann, and V. Cuq, “DRELIO: An Unmanned Helicopter for Imaging Coastal Areas,” *J. Coast. Res.*, vol. 2009, no. 56, pp. 1489–1493, 2009.

[50] J. R. M.-D. Dios and A. Ollero, “Automatic Detection of Windows Thermal Heat Losses in Buildings Using UAVs,” in *2006 World Automation Congress*, 2006, pp. 1–6.

[51] A. Jaimes, S. Kota, and J. Gomez, “An approach to surveillance an area using swarm of fixed wing and quad-rotor unmanned aerial vehicles UAV(s),” *2008 IEEE Int. Conf. Syst. Syst. Eng.*, pp. 1–6, Jun. 2008.

[52] J. G. Leishman, *Principles of Helicopter Aerodynamics*. Cambridge University Press, 2006, p. 55.

[53] L. Rodolfo García Carrillo, A. Enrique Dzul López, R. Lozano, and C. Pégard, *Quad Rotorcraft Control*. Springer, 2013, pp. 23–25.

[54] C. Stachniss, U. Frese, and G. Grisetti, “What is Slam?” [Online]. Available: http://www.openslam.org/. [Accessed: 27-Sep-2012].

[55] Z. Zhang, G. Nejat, and Z. Zhe, “Robot-assisted intelligent 3D mapping of unknown cluttered search and rescue environments,” *2008 IEEE/RSJ Int. Conf. Intell. Robot. Syst.*, pp. 2115–2120, Sep. 2008.

[56] M. Achtelik, A. Bachrach, and R. He, “Autonomous navigation and exploration of a quadrotor helicopter in GPS-denied indoor environments,” *IEEE ICRA*, 2008.

[57] R. C. Luo, L. Shih-Chi, and L. Chun Chi, “Indoor autonomous mobile robot localization using natural landmark,” in *Industrial Electronics, 2008. IECON 2008. 34th Annual Conference of IEEE*, 2008, pp. 1626–1631.

[58] G. Zunino, “Simultaneous Localization and Mapping for Navigation in Realistic Environments,” University of Stockholm, 2002.

[59] L. Iocchi and S. Pellegrini, “Building 3d Maps With Semantic Elements Integrating 2d Laser, Stereo Vision And IMU On A Mobile Robot,” in *Proc. 2nd ISPRS Intl. Workshop 3D-ARCH*, 2007.

[60] P. Rudol, M. Wzorek, and P. Doherty, “Vision-Based Pose Estimation For Autonomous Indoor Navigation Of Micro-Scale Unmanned Aircraft Systems,” in *Robotics and Automation (ICRA), 2010 IEEE International Conference on*, 2010, pp. 1913–1920.

[61] G. Jang, S. Kim, W. Lee, and I. Kweon, “Color landmark based self-localization for indoor mobile robots,” *Proc. 2002 IEEE Int. Conf. Robot. Autom. (Cat. No.02CH37292)*, vol. 1, no. May, pp. 1037–1042, 2002.

[62] F. Caballero, L. Merino, J. Ferruz, and A. Ollero, *A visual odometer without 3D reconstruction for aerial vehicles. Applications to building inspection*, no. April. Barcelona: IEEE, 2005, pp. 4673–4678.

[63] G. Xu and X. Meng, “The MEMS IMU Error Modeling Analysis Using Support Vector Machines,” *2009 Second Int. Symp. Knowl. Acquis. Model.*, pp. 335–337, 2009.

Chapter 3 Representation of an Object's 3D Position and Orientation

In the previous chapter it was concluded that a quadrotor would be used as the method of deployment for a sensor suite to perform an indoor building inspection. The sensor suite requires a method for describing the position and orientation of a target in 3D space relative to a known coordinate system. The work in this chapter is based upon the work by J. J. Craig [1].

The first section explains how the position and oreintation of an object in 3D space can be represented. Two types of representation are then discussed and one method is then selected for use in the project.

3.1 Using 3D Data

A 3D sensor suite can gather range data by using a 2D (LRS). This leads to the question of how to locate and represent mathematically an object in 3D space. In order to describe an object in 3D space its position and orientation need to be described relative to a known coordinate system. To describe the position and orientation of the 2D laser range scanner in space, a coordinate system has to be attached to the LRS. The LRS can be described in terms of its position and orientation with respect to a reference coordinate system.
Figure 2 (a) shows the LRS has a reference coordinate system attached to it. The LRS in Figure 2 has a forward facing side that the laser beam originates from and is denoted by an arrow. The top side of the LRS is coloured purple and the bottom side yellow. Figure 2(a) shows the LRS in a starting orientation and position relative to the reference coordinate axis applied to the LRS. Figure 2 (b) shows the LRS is rotated around the X axis of the coordinate system, showing the yellow bottom side of the LRS. Figure 2(c) shows the LRS is rotated around the Z axis of the coordinate system, as the forward facing side of the LRS is facing the opposite way to the original Figure 2(a). Figure 2 shows that regardless of the orientation and position of the LRS, the position and orientation of the LRS can be described relative to the reference coordinate system attached to the LRS.

As any frame can serve as a reference system which can express the position and orientation of an object then transforming and changing the description of these object attributes can be expressed as changing from one frame to another.

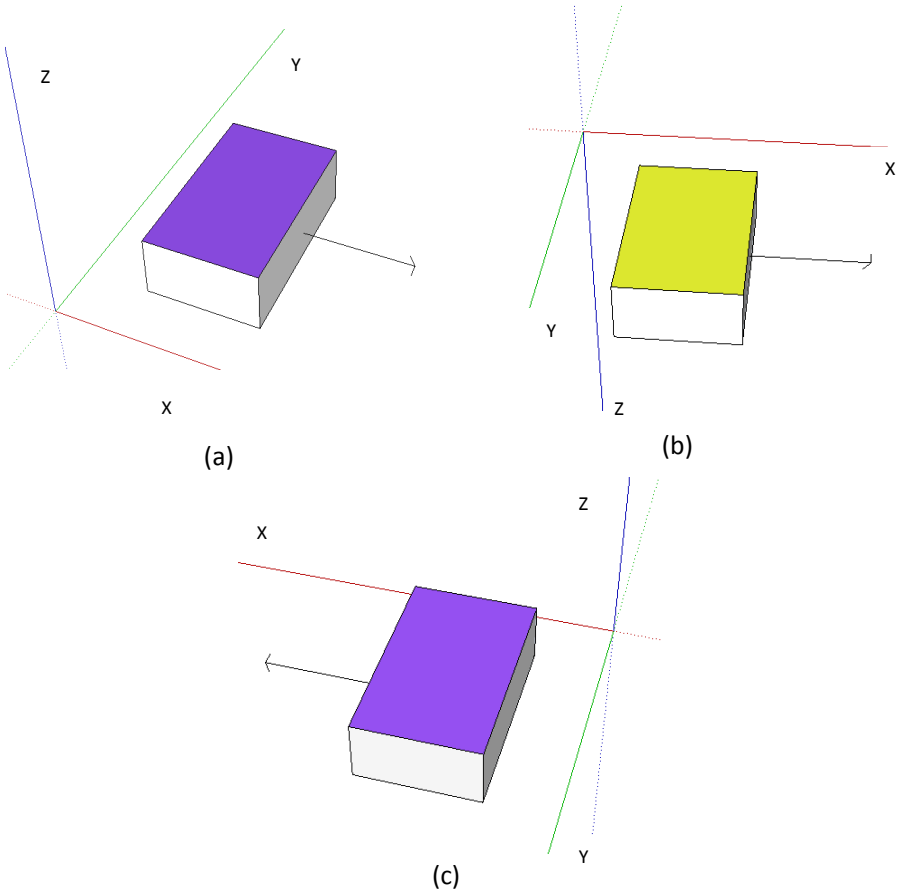

Figure 2 – LRS with reference coordinate system applied (a), LRS rotated around axis (b) and (c)

3.1.1 Description of a Position

Once the coordinate system around an object is created any point in space can be located with a three element position vector. As many different coordinate systems are used in the project the vectors must be identifying information defining which coordinate system they are defined in. In this vectors are defined by having a leading superscript which indicates the coordinate system to which they are referenced. For example and using a Cartesian coordinate system $^{A}\boldsymbol{B}$, indicates that its components indicate the distances along the axes of the frame of reference A, denoted $\{\boldsymbol{A}\}$. The point $^{A}\boldsymbol{B}$ can be represented by a vector of which can be thought of as an ordered set of numbers where the individual elements of the vector are given subscripts x, y and z. Equation 1.

$$^{A}\mathbf{B} = \begin{bmatrix} \boldsymbol{p}_x \\ \boldsymbol{p}_y \\ \boldsymbol{p}_z \end{bmatrix} \qquad \mathbf{1}$$

Homogeneous Coordinates

Based on the work by Szeliski [2]it can be seen that homogeneous coordinates can be used to represent 2D and 3D coordinates.

2D points can be described using a pair of values as shown in Equation 2. 2D points can also be represented using homogeneous coordinates, Equation 3 where the vectors that differ by scale only are considered to be equivalent as shown in Equation 4[2].

$$\boldsymbol{x} = \begin{bmatrix} \boldsymbol{x} \\ \boldsymbol{y} \end{bmatrix} \quad \textbf{2}$$

$$\tilde{\boldsymbol{x}} = (\tilde{\boldsymbol{x}}, \tilde{\boldsymbol{y}}, \tilde{\boldsymbol{z}}) \in \boldsymbol{P^2} \quad \textbf{3}$$

$$\boldsymbol{P^2} = \boldsymbol{R^3} - (\boldsymbol{0}, \boldsymbol{0}, \boldsymbol{0}) \quad \textbf{4}$$

The homogeneous vector $\tilde{\boldsymbol{x}}$ can be converted back into an inhomogeneous vector $\boldsymbol{x}$ by dividing through by the last element $\tilde{w}$ as shown in Equation 6. Where the augmented vector is

$$\bar{\boldsymbol{x}} = (\boldsymbol{x}, \boldsymbol{y}, \boldsymbol{1}) \quad \textbf{5}$$

$$\tilde{\boldsymbol{x}} = (\tilde{\boldsymbol{x}}, \tilde{\boldsymbol{y}}, \tilde{\boldsymbol{z}}) = \tilde{\boldsymbol{w}}(\boldsymbol{x}, \boldsymbol{y}, \boldsymbol{1}) = \tilde{\boldsymbol{w}}\bar{\boldsymbol{x}}, \quad \textbf{6}$$

In situations where the last element of a homogeneous is $(\tilde{w} = 0)$ they do not have an equivalent inhomogeneous representation and are called points at infinity.

3D points can be written in inhomogeneous coordinates as shown in Equation 7 or as homogeneous coordinates Equation 8

$$\boldsymbol{x} = (\boldsymbol{x}, \boldsymbol{y}, \boldsymbol{z}) \in \boldsymbol{R^3} \quad \textbf{7}$$

$$\tilde{\boldsymbol{x}} = (\tilde{\boldsymbol{x}}, \tilde{\boldsymbol{y}}, \tilde{\boldsymbol{z}}, \tilde{\boldsymbol{w}}) \quad \textbf{8}$$

The augmented vector shown in Equation 9 can be used to represent a 3D point, Equation 10

$$\bar{\boldsymbol{x}} = (\boldsymbol{x}, \boldsymbol{y}, \boldsymbol{1}) \quad \textbf{9}$$

$$\tilde{\boldsymbol{x}} = \tilde{\boldsymbol{w}}\,\bar{\boldsymbol{x}} \quad \textbf{10}$$

3D Transformations

Translation

A 3D translation can be written as

$$\boldsymbol{x}' = \boldsymbol{x} + \boldsymbol{t} \quad \textbf{11}$$

Or using the 3*3 identity matrix where 0 is the unit vector

$$\boldsymbol{x}' = [\boldsymbol{R}\ \boldsymbol{t}]\,\overline{\boldsymbol{x}} \quad \textbf{12}$$

Rotation and Translation

Rotation and translation also known as 3D Euclidean transformation can be described by

$$\boldsymbol{x}' = \boldsymbol{R}\boldsymbol{x} + \boldsymbol{t} \quad \textbf{13}$$

Or

$$\boldsymbol{x}' = [\boldsymbol{R}\ \boldsymbol{t}]\overline{\boldsymbol{x}} \quad \textbf{14}$$

R is a 3*3 orthonormal matrix where $\boldsymbol{R}\boldsymbol{R}^T = \boldsymbol{I}$ and $|\boldsymbol{R}| = 1$

Three rotation transforms are present below, scaled, affine and projective.

The scaled rotation transform preserves the angles between lines and planes. Using the 3D similarity transform $\boldsymbol{x}' = s\boldsymbol{R}\boldsymbol{x} + \boldsymbol{t}$ where s is an arbitrary scale factor it can be shown as

$$\boldsymbol{x}' = [s\boldsymbol{R}\ \boldsymbol{t}]\overline{\boldsymbol{x}} \quad \textbf{15}$$

The affine rotation transform preserves parallel lines and planes. The transform can be describes as $\boldsymbol{x}' = \boldsymbol{A}\boldsymbol{x}$ where $\boldsymbol{A}$ is a 3*4 matrix Equation 16

$$\boldsymbol{x}' = \begin{bmatrix} \boldsymbol{a_{00}} & \boldsymbol{a_{01}} & \boldsymbol{a_{02}} & \boldsymbol{a_{03}} \\ \boldsymbol{a_{10}} & \boldsymbol{a_{11}} & \boldsymbol{a_{12}} & \boldsymbol{a_{13}} \\ \boldsymbol{a_{20}} & \boldsymbol{a_{21}} & \boldsymbol{a_{22}} & \boldsymbol{a_{23}} \end{bmatrix} \overline{\boldsymbol{x}} \quad \textbf{16}$$

The projection transform operates on homogeneous coordinates as shown in Equation 17, where $\tilde{\boldsymbol{H}}$ is a 4*4 homogeneous matrix.

$$\tilde{\boldsymbol{x}}' = \tilde{\boldsymbol{H}}\tilde{\boldsymbol{x}} \quad \textbf{17}$$

The perspective transform preserves straight lines, but the homogeneous coordinates produced, $\tilde{\boldsymbol{x}}'$ have to be normalised in order to obtain an inhomogeneous result $\boldsymbol{x}$.

3D rotations

Using Homogenous coordinates rotation can be represented by a rotation of the $\hat{\boldsymbol{n}}$ and an angle θ.

The vector $\boldsymbol{v}$ is projected onto the $\hat{\boldsymbol{n}}$ axis to get

$$\boldsymbol{v}_{||} = \hat{\boldsymbol{n}}(\hat{\boldsymbol{n}} \,.\, \boldsymbol{v}) = (\hat{\boldsymbol{n}}\hat{\boldsymbol{n}}^{\boldsymbol{T}})\boldsymbol{v} \quad \textbf{18}$$

Which is the component of $\boldsymbol{v}$ that is not affected by the rotation. The next stage is to calculate the perpendicular residual of $\boldsymbol{v}$ from $\hat{\boldsymbol{n}}$

$$\boldsymbol{v}_{\perp} = \boldsymbol{v} - \boldsymbol{v}_{||} = (\boldsymbol{I} - \hat{\boldsymbol{n}}\hat{\boldsymbol{n}}^{\boldsymbol{T}})\boldsymbol{v} \quad \textbf{19}$$

The vector can be rotated by 90°, where $[\hat{\boldsymbol{n}}]_{\times}$ is the matrix form of the cross product operator with the vector $\hat{\boldsymbol{n}} = (\hat{\boldsymbol{n}}_{\boldsymbol{x}}, \hat{\boldsymbol{n}}_{\boldsymbol{y}}, \hat{\boldsymbol{n}}_{\boldsymbol{z}})$

$$\boldsymbol{v}_{\times} = \hat{\boldsymbol{n}} \times \boldsymbol{v} = [\hat{\boldsymbol{n}}]_{\times}\boldsymbol{v} \quad \textbf{20}$$

Rotating the vector by another 90° is equivalent of taking the cross product again

$$\boldsymbol{v}_{\times\times} = \hat{\boldsymbol{n}} \times \boldsymbol{v}_{\times} = [\hat{\boldsymbol{n}}]_{\times}^{2}\,\boldsymbol{v} = -\boldsymbol{v}_{\perp} \quad \textbf{21}$$

Which allows for

$$\boldsymbol{v}_{||} = \boldsymbol{v} - \boldsymbol{v}_{\perp} = \boldsymbol{v} + \boldsymbol{v}_{\times\times} = (\boldsymbol{I} + [\hat{\boldsymbol{n}}]_{\times}^{2})\boldsymbol{v} \quad \textbf{22}$$

The in plane component or the rotated vector $\boldsymbol{u}$ can now be calculated as

$$\boldsymbol{u}_{\perp} = \boldsymbol{cos\theta v} + \boldsymbol{sin\theta v}_{\times} = \left(\mathbf{sin\theta}[\hat{\boldsymbol{n}}]_{\times} - \boldsymbol{cos\theta}[\hat{\boldsymbol{n}}]_{\times}^{\mathbf{2}}\right)\boldsymbol{v} \quad \mathbf{23}$$

When all of the terms are collected the form the final rotated vector

$$\boldsymbol{u} = \boldsymbol{u}_{\perp} + \boldsymbol{v}_{||} = (\boldsymbol{I} + \boldsymbol{sin\theta}[\hat{\boldsymbol{n}}]_{\times} + (\mathbf{1} - \boldsymbol{cos\theta})[\hat{\boldsymbol{n}}]_{\times}^{\mathbf{2}})\boldsymbol{v} \quad \mathbf{24}$$

A rotation can matrix corresponding to the a rotation by θ around an axis $\hat{\boldsymbol{n}}$ as

$$\boldsymbol{R}(\hat{\boldsymbol{n}}, \boldsymbol{\theta}) = \boldsymbol{I} + \boldsymbol{sin\theta}[\hat{\boldsymbol{n}}]_{\times} + (\mathbf{1} - \boldsymbol{cos\theta})[\hat{\boldsymbol{n}}]_{\times}^{\mathbf{2}} \quad \mathbf{25}$$

Which is known as Rodriguez's formula.

A rotation matrix can be formed as the product from three rotations around three cardinal axes, such as x, y, z and z, y, x. Depending on the order in which the rotations are applied can produce different results. A single matrix can be used to calculate the rotation and translation around an axis by an angle. This is particularly useful in this research as by expanding the Cartesian coordinates into Homogeneous coordinates allows us to apply the rotation and translation matrix and then convert the resulting vector back into a Cartesian coordinate. For simplicity section 3.1.2 shows two Cartesian coordinate systems using Euler angles which can be used to describe the orientation of a body in 3D space.

Homogeneous and Cartesian Coordinates

The range and angle data gathered from a range sensor can be used to create 3D point cloud from the origin of the target to the world axis using several coordinate frames. The data collected from a sensor could be a mixture of Polar and Cartesian coordinates. Homogeneous coordinates are required to homogenise the inhomogeneous coordinates to allow for rotation and translations. To do this each element in a Cartesian coordinate matrix is multiplied by a non-zero value called a scalar element which is added to the matrix. The Cartesian coordinates have then been converted into a Homogeneous coordinates. After the rotation and translation matrices have been applied the homogeneous coordinates can be converted back into inhomogeneous coordinates. To convert the Homogeneous coordinates back into inhomogeneous coordinates the elements in the matrix have to be divided by the scalar and then discard the scalar element. Chapter 5 uses Homogeneous coordinates which allows rotations and translations required to describe the position and

orientation of 3D points. The 3D point data is then converted back into Cartesian coordinates and graphically represented.

3.1.2 Description of Orientation

It can also be necessary to describe the orientation of an object in space as well as its position. If for example ${}^{A}B$ describes the centre point of a robotic hand, then complete location of the robotic hand is not described until its orientation is also described. To describe the orientation of the body a coordinate system is attached to the body and then give a description of this new coordinate system relative to the reference system (Figure 3). A description of the coordinate system $\{\boldsymbol{A}\}$ relative to the body attached to coordinate system $\{\boldsymbol{B}\}$ which has been offset by ${}^{\boldsymbol{A}}\boldsymbol{B}$ now gives the position an orientation of the body.

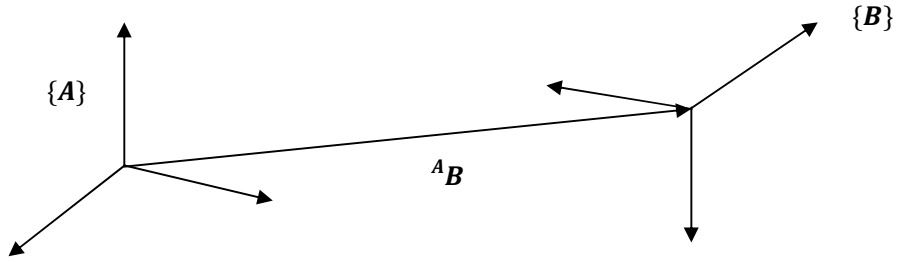

Figure 3 – $\{\boldsymbol{A}\}$ **coordinate system relative to coordinate system** $\{\boldsymbol{B}\}$

One way in which to describe the body attached coordinate system $\{\boldsymbol{B}\}$ is to express the unit vectors of its three principle axis in terms of if the coordinate system$\{\boldsymbol{A}\}$. We can write the principal directions of coordinate system $\{\boldsymbol{B}\}$ as unit vectors $\hat{\mathbf{X}}_{\mathbf{B}}$, $\hat{\mathbf{Y}}_{\mathbf{B}}$, $\hat{\mathbf{Z}}_{\mathbf{B}}$. When written in terms of the coordinate system $\{\boldsymbol{A}\}$ they are ${}^{\boldsymbol{A}}\hat{\mathbf{X}}_{\mathbf{B}}$, ${}^{\boldsymbol{A}}\hat{\mathbf{Y}}_{\mathbf{B}}$, ${}^{\boldsymbol{A}}\hat{\mathbf{Z}}_{\mathbf{B}}$. These three unit vectors can be conveniently stacked together as columns in a 3 x 3 matrix in the order ${}^{\boldsymbol{A}}\hat{\mathbf{X}}_{\mathbf{B}}$, ${}^{\boldsymbol{A}}\hat{\mathbf{Y}}_{\mathbf{B}}$, ${}^{\boldsymbol{A}}\hat{\mathbf{Z}}_{\mathbf{B}}$. This matrix is called a rotation matrix and in this case describes the orientation of the frame $\{\boldsymbol{B}\}$ relative to $\{\boldsymbol{A}\}$, and we can represent it by ${}^{A}_{B}R$.

$$ {}^{A}_{B}\boldsymbol{R} = \left[{}^{\mathrm{A}}\hat{\mathbf{X}}_{\mathbf{B}} \;\; {}^{\mathrm{A}}\hat{\mathbf{Y}}_{\mathbf{B}} \;\; {}^{\mathrm{A}}\hat{\mathbf{Z}}_{\mathbf{B}} \right] = \begin{bmatrix} \boldsymbol{r11} & \boldsymbol{r12} & \boldsymbol{r13} \\ \boldsymbol{r21} & \boldsymbol{r22} & \boldsymbol{r23} \\ \boldsymbol{r31} & \boldsymbol{r32} & \boldsymbol{r33} \end{bmatrix} \qquad \mathbf{26} $$

As the components of a vector are the projections of that vector onto the unit directions of its reference frame, an expression for the scalars r_{ij} in Equation 26 can be written. Thus each component in ${}^{A}_{B}\boldsymbol{R}$ can be written as the scalar product of a pair of unit vectors as shown in Equation 27. The leading subscripts have been omitted for brevity. It follows that ${}^{B}_{A}\boldsymbol{R}$, (description of frame $\{\boldsymbol{A}\}$ relative to $\{\boldsymbol{B}\}$) is given by the transpose of Equation 27 as shown in Equation 28. Now that the rotation matrix and its transpose matrix have been described, methods that use only three numbers to describe the orientation are developed.

$$ {}^{A}_{B}\boldsymbol{R} = \begin{bmatrix} {}^{A}\hat{\mathbf{X}}_{\mathbf{B}} & {}^{A}\hat{\mathbf{Y}}_{\mathbf{B}} & {}^{A}\hat{\mathbf{Z}}_{\mathbf{B}} \end{bmatrix} = \begin{bmatrix} \hat{\mathbf{X}}_{\mathbf{B}} \cdot \hat{\mathbf{X}}_{\mathbf{A}} & \hat{\mathbf{Y}}_{\mathbf{B}} \cdot \hat{\mathbf{X}}_{\mathbf{A}} & \hat{\mathbf{Z}}_{\mathbf{B}} \cdot \hat{\mathbf{X}}_{\mathbf{A}} \\ \hat{\mathbf{X}}_{\mathbf{B}} \cdot \hat{\mathbf{Y}}_{\mathbf{A}} & \hat{\mathbf{Y}}_{\mathbf{B}} \cdot \hat{\mathbf{Y}}_{\mathbf{A}} & \hat{\mathbf{Z}}_{\mathbf{B}} \cdot \hat{\mathbf{Y}}_{\mathbf{A}} \\ \hat{\mathbf{X}}_{\mathbf{B}} \cdot \hat{\mathbf{Z}}_{\mathbf{A}} & \hat{\mathbf{Y}}_{\mathbf{B}} \cdot \hat{\mathbf{Z}}_{\mathbf{A}} & \hat{\mathbf{Z}}_{\mathbf{B}} \cdot \hat{\mathbf{Z}}_{\mathbf{A}} \end{bmatrix} \quad \textbf{27} $$

$$ {}^{B}_{A}\boldsymbol{R} = {}^{A}_{B}\boldsymbol{R}^{T} \quad \textbf{28} $$

3.1.3 X-Y-Z Fixed Angles

Using X-Y-Z fixed angles allow for representations of spatial orientation of any frame as composed of a series of rotations from a frame of reference. This only requires three numbers to describe its orientation. It should be noted that the addition of “primes” indicates that the rotation is performed by Euler angles.

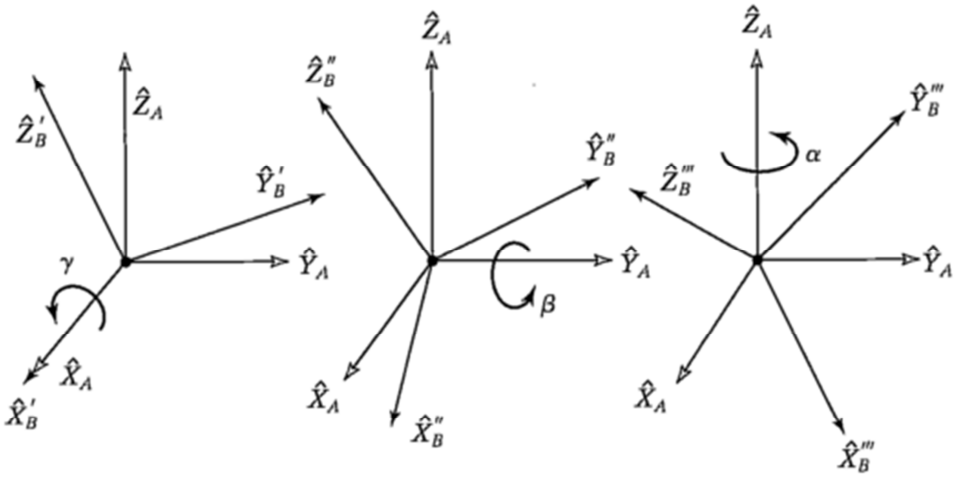

Figure 4 – X-Y-Z Fixed angles [1]

To describe the orientation of frame $\{\boldsymbol{B}\}$ with reference to a known frame $\{\boldsymbol{A}\}$, the origin of both frames need to be coincident to the known reference frame $\{\boldsymbol{A}\}$. By rotating frame $\{\boldsymbol{B}\}$ around $\hat{\mathrm{X}}_{\mathrm{A}}$ by an angle γ, Equation 29 is produced which describes roll.

$$\boldsymbol{{}^{A}_{B}R_{X}(\gamma) = R_{X}(\gamma) = \begin{bmatrix} 1 & 0 & 0 \\ 0 & cos\gamma & -sin\gamma \\ 0 & sin\gamma & cos\gamma \end{bmatrix}} \qquad \textbf{29}$$

Rotating $\{\boldsymbol{B}\}$ around $\hat{\mathbf{Y}}_{\mathbf{A}}$ by an angle β , Equation 30 is produced which describes pitch.

$$\boldsymbol{{}^{A}_{B}R_{Y}(\beta) = R_{Y}(\beta) = \begin{bmatrix} cos\beta & 0 & sin\beta \\ 0 & 1 & 0 \\ -sin\beta & 0 & cos\beta \end{bmatrix}} \qquad \textbf{30}$$

Rotating $\{\boldsymbol{B}\}$ around $\hat{\mathbf{Z}}_{\mathbf{A}}$ by an angle α, Equation 31 is produced which describes yaw.

$$\boldsymbol{{}^{A}_{B}R_{Z}(\alpha) = R_{Z}(\alpha) = \begin{bmatrix} cos\alpha & -sin\alpha & 0 \\ sin\alpha & cos\alpha & 0 \\ 0 & 0 & 1 \end{bmatrix}} \qquad \textbf{31}$$

Each of the rotations happens around an axis in the fixed reference frame $\{\boldsymbol{A}\}$ and are called the X-Y-Z fixed angles. The "fixed" part of the name refers to the fact that the rotation is described with respect to the origin. As all of the rotations occur around the axes of the reference frame the final compound rotation matrix ${}^{A}_{B}\boldsymbol{R}_{X\,Y\,Z}(\boldsymbol{\gamma},\boldsymbol{\beta},\boldsymbol{\alpha})$ is shown in Equation 32

$$\boldsymbol{{}^{A}_{B}R_{X\,Y\,Z}(\gamma,\beta,\alpha) = R_{Z}(\alpha)R_{Y}(\beta)R_{X}(\gamma)}$$

$$\boldsymbol{= \begin{bmatrix} cos\alpha & -sin\alpha & 0 \\ sin\alpha & cos\alpha & 0 \\ 0 & 0 & 1 \end{bmatrix} \begin{bmatrix} cos\beta & 0 & sin\beta \\ 0 & 1 & 0 \\ -sin\beta & 0 & cos\beta \end{bmatrix} \begin{bmatrix} 1 & 0 & 0 \\ 0 & cos\gamma & -sin\gamma \\ 0 & sin\gamma & cos\gamma \end{bmatrix}} \qquad \textbf{32}$$

By multiplying out the intermediate steps Equation 33 is observed.

$$
{}^{A}_{B}R_{X\,Y\,Z}(\gamma,\beta,\alpha) =
$$

$$
\begin{bmatrix} cos\alpha cos\beta & cos\alpha sin\beta sin\gamma - sin\alpha cos\gamma & cos\alpha sin\beta cos\gamma + sin\alpha sin\gamma \\ sin\alpha cos\beta & sin\alpha sin\beta sin\gamma + cos\alpha cos\gamma & sin\alpha sin\beta cos\gamma - cos\alpha sin\gamma \\ -sin\beta & cos\beta sin\gamma & cos\beta cos\gamma \end{bmatrix} \qquad \textbf{33}
$$

Equation 33 is only correct if the rotations are performed in the order as mentioned above.

This method of describing the orientation of an object in 3D space is most useful when dealing with a fixed reference frame $\{\boldsymbol{A}\}$. In the field of robotics however it is common to have the rotations performed about the axis of a moving reference frame which this method cannot describe. In this case another system must be used to describe the orientation of an object in 3D space.

3.1.4 Z-Y-X Euler Angles

In the Z-Y-X Euler Angles representation each rotation is performed around an axis of the moving coordinate system $\{\boldsymbol{B}\}$ instead of the fixed axis reference $\{\boldsymbol{A}\}$. To describe the orientation of frame $\{\boldsymbol{B}\}$ we need to begin with a known frame $\{\boldsymbol{A}\}$. By rotating frame $\{\boldsymbol{B}\}$ around $\hat{\mathbf{Z}}_{\mathbf{B}}$ by angle α gives yaw, then rotating around $\hat{\mathbf{Y}}_{\mathbf{B}}$ by angle β gives pitch, and then rotating around $\hat{\mathbf{X}}_{\mathbf{B}}$ by angle γ gives roll (Figure 5).

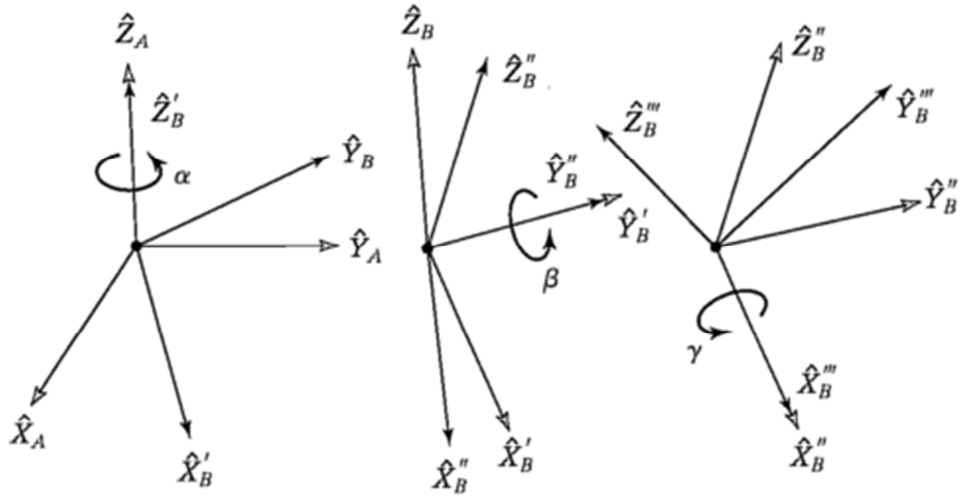

Figure 5 – Z -Y-X Euler angles [1]

The three rotation angles are a set of Euler angles. In this representation the three rotations of the axis depends on the preceding rotation occurring in order about the $\hat{\mathbf{Z}}_\mathbf{B}\ \hat{\mathbf{Y}}_\mathbf{B}\ \hat{\mathbf{X}}_\mathbf{B}$ axes. This representation is called Z-Y-X Euler angles. Figure 5 shows that rotating by an angle α around $\hat{\mathbf{Z}}_\mathbf{B}$ causes $\hat{\mathbf{X}}_\mathbf{B}$ to rotate into $\hat{\mathbf{X}}_\mathbf{B}{}'$, and $\hat{\mathbf{Y}}_\mathbf{B}$ rotate into $\hat{\mathbf{Y}}_\mathbf{B}{}'$ etc. and with the other fixed angles β and γ an additional "prime" is added to each axis to indicate that it is an intermittent frame. There are several intermediate frames {B'}, {B''} and {B''} used in order to express ${}^{\boldsymbol{A}}_{\boldsymbol{B}}\boldsymbol{R}_{\boldsymbol{X\,Y\,Z}}(\boldsymbol{\alpha},\boldsymbol{\beta},\boldsymbol{\gamma})$. Using these intermediate frame descriptions we can express ${}^{\boldsymbol{A}}_{\boldsymbol{B}}\boldsymbol{R}$ as shown in Equation 34 with each descriptor expressed by the Z-Y-X Euler angle convention [1]. This describes the final orientation of $\{\boldsymbol{B}\}$ relative to $\{\boldsymbol{A}\}$ and can be seen in Equation 35.Once we multiply out Equation 35 we obtain Equation 33 and can see that the result is the same as that obtained by three fixed angle rotations in the opposing order about the fixed axis. It can then be seen that in "general that three rotations taken about a fixed axes yield the same final orientation as the same three rotations taken in opposite order about the axis of the moving frame."[1]

$$ {}^{\boldsymbol{A}}_{\boldsymbol{B}}\boldsymbol{R} = {}^{\boldsymbol{A}}_{\boldsymbol{B'}}\boldsymbol{R}\ {}^{\boldsymbol{B'}}_{\boldsymbol{B''}}\boldsymbol{R}\ {}^{\boldsymbol{B''}}_{\boldsymbol{B}}\boldsymbol{R} \tag{34}$$

$$ {}^{\boldsymbol{A}}_{\boldsymbol{B}}\boldsymbol{R}_{\boldsymbol{Z\,Y\,X}} = \boldsymbol{R}_{\boldsymbol{Z}}(\boldsymbol{\alpha})\boldsymbol{R}_{\boldsymbol{Y}}(\boldsymbol{\beta})\boldsymbol{R}_{\boldsymbol{X}}(\boldsymbol{\gamma}) = \begin{bmatrix} \boldsymbol{cos\alpha} & \boldsymbol{-sin\alpha} & \mathbf{0} \\ \boldsymbol{sin\alpha} & \boldsymbol{cos\alpha} & \mathbf{0} \\ \mathbf{0} & \mathbf{0} & \mathbf{1} \end{bmatrix} \begin{bmatrix} \boldsymbol{cos\beta} & \mathbf{0} & \boldsymbol{sin\beta} \\ \mathbf{0} & \mathbf{1} & \mathbf{0} \\ \boldsymbol{-sin\beta} & \mathbf{0} & \boldsymbol{cos\beta} \end{bmatrix} \begin{bmatrix} \mathbf{1} & \mathbf{0} & \mathbf{0} \\ \mathbf{0} & \boldsymbol{cos\gamma} & \boldsymbol{-sin\gamma} \\ \mathbf{0} & \boldsymbol{sin\gamma} & \boldsymbol{cos\gamma} \end{bmatrix} \tag{35}$$

One of the main advantages of using Euler angles is that they offer a minimal representation of orientation of a coordinate frame that can be described by three angles(α, β, γ). A drawback when using Euler angles is that they can suffer from gimbal lock. Gimbal lock is the loss of one degree of freedom in a three dimensional system and occurs when two of the three axis of the gimbal become parallel to each other and rotate at the same time. An example of this would be if a UAV pitches up to 90°, the roll axis becomes parallel to the yaw axis and no axis can perform any yaw rotations and a degree of freedom is lost.

3.2 Conclusion

Two methods of expression of orientation of an object in 3D space have been discussed. The methods discussed for describing orientation are only two of many possible descriptions that could be used. The XYZ fixed angles show how to describe an object in 3D space in a very simple manner, but as they only deal with a single fixed reference frame they cannot describe objects within a moving system. The use of ZYX Euler angles allows the description of an object in a moving system. As no complex manoeuvres are being performed as the simulation of the UAV is operating at fixed positions, there will be no gimbal lock present on the test rig and also in the final system. The work that follows will use ZYX Euler angles as this method lends itself to describing the orientation of the sensor with respect to the UAV, which itself is referenced to the UAV orientation with respect to an external world frame.

3.3 References

[1] J. J. Craig, *Introduction to Robotics : Mechanics and Control*, 2nd Editio. Addison-Wesley, 1989.

[2] R. Szeliski, “Geometric primitives and transformations,” in *Computer Vision: Algorithms and Applications*, 2010, pp. 32–42.

Chapter 4 Sensor Suite Design

4.1 Introduction

This chapter describes methods used by different laser range scanners to gather range data. The advantages and disadvantages of these methods are discussed. A method to use a 2D laser range scanner to gather 3D range data is also discussed .Two laser range scanners and two cameras are then compared and evaluated against the requirements of the UAV system which are also reviewed. The selection of a suitable laser range scanner and camera is then discussed.

After discussions with the company it was decided that a suitable laser range scanner for use in this system would have accuracy in the region of ±1cm with an operating range under 5 meters, low weight (under 1Kg) and small size to meet the brief outlines relating to enclosed high access areas as stated in chapter 1 and discussed in chapter 2. The UAV will need to be airborne for around 15 – 20 minutes, so low power consumption is a priority. The sensor suite should have several in flight functions, such as the ability to visually observe defects and measure physical dimensions.

To meet the need to visually observe defects, a comparison of two cameras for the senor suite is performed.

4.2 Range Measurement Methods

Range measurements using laser light are broken down into two main method categories: Time of Flight and Triangulation.

4.2.1 Time Of Flight (TOF)

4.2.2 Pulsed Time Of Flight (PTOF)

These devices emit pulses of light towards the target. The light travels towards the target at the speed of light and hits the target, at which point some of the light is absorbed by the object and some of it reflected back. The reflected light is then detected by the device and the round trip time taken from emission to detection is recorded (Figure 6). As the speed of light is constant (c) and the

time taken for the light to reach the object and its reflection to be detected is measured (t), the distance (D) can be calculated as shown by Jain [1].

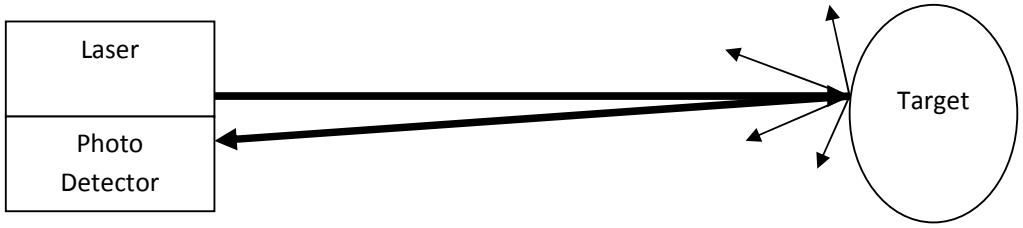

Figure 6 – PTOF mechanism

4.2.3 Phase Shift Time Of Flight (PSTOF)

These devices project a sinusoidal signal instead of a pulsed signal and the range to the target is calculated from the phase shift of the reflected signal returned. Using calculations from Jain [1] and Amann, Markus-Christian et al [2] the projected signal $s_E(t)$ where t is the time taken for the light to reach the object and its reflection to be detected and the angular frequency ω_0 is measured.

4.2.4 Advantages and Disadvantages

A single light pulse emitted from the laser range finder is not a reliable way to measure a distance as the light pulse can return erroneous data or miss the target. A large number of light pulses are emitted to mitigate these possible effects. The average distance determined by several light pulses give a more reliable and accurate target distance. The mean D_n of D approaches the true value of D in the limit as the number of samples, n becomes infinitely large. Where in this case D is the actual range to the target, and D_n is the mean of D. Barford [3] explains if the measurements taken have a frequency distribution with a narrow peak, and therefore a small standard deviation (σ) the measurements are likely to be close together and that their mean D_n is closer to the true value D. If the peak is broad, the measurements are more widely scattered and D_n less likely to be near D. The value σ or its best estimate of precision s_n must now describe the accuracy of D_n to the extent that the smaller s_n is the nearer the value of D_n is to D. If this has a narrow symmetrical peak and therefore a small value of σ the measurements are likely to be closer to their mean D_n which is

nearer the true value D. If enough measurements, n are made then D_n approaches D. Barford shows that the best estimate for the value of the standard error $\sigma(D_n)$ is the estimate S_n which is the adjusted standard error.

$$S_n = \frac{\sigma_n(D)}{(n-1)^{\frac{1}{2}}} \quad \textbf{36}$$

Which can be summarised by

$$D = D_n \pm S_n \quad \textbf{37}$$

It is important to recognise that as the number of measurements increases s_n decreases, as it can only approach closer to the fixed quantity σ which defines the precision of the experiment and which is experimentally dependant and can either be large or small. s_n does decrease as n increases as it estimates the mean deviation of D_n from D. This deviation from the true value must approach zero as n is increased towards infinity.

A single light pulse would be in the order of picoseconds to nanoseconds in duration, and as stated an accurate and reliable range reading requires the use of multiple light pulses to reduce the standard error in the mean. Therefore the more accurate the range measurement is required, the more light pulses must be emitted at the target.

One drawback with this method for gathering range data is that only the point in the laser range scanner's field of view (FOV) can be measured at any one time. To compensate for this drawback laser range scanners use an optical mirror to rotate the laser beam to create a scanning arc. An accurate measurement of the total length the laser beam travelled needs to be accounted for to reduce inaccuracies in the measurement. The accuracy of this method is dependent on its ability to detect the reflected light from the target and also the accuracy of the clock timing the round trip.

Another consideration when using a laser range scanner is that the typical distance to the target influences the type of laser device used. For short distance measurements ranging from centimetres to meters, a relatively low power (class I)[4] laser can be used such as a SICK LMS[5] or URG-04LX [6]. The higher safety class lasers require precautions to be undertaken in order to avoid injuries or damage [7]. In this research an aim is to measure targets that are less than five meters away from the Laser Range Scanner. To this point there is no need to use high powered LRS that can measure

large distances, but care must be used to select a suitable LRS that should not pose any possible health and safety concerns.

TOF and PSTOF laser range scanners are suitable for use in this project, as they can work at varying distances from 1 to 100's of meters away from the target. It has also been shown that to meet the specifications set out in the introduction a class I laser is to be used as it requires no extra precautions to be taken regarding safety.

4.2.5 Triangulation

Triangulation is the method of determining a location of a specific point by measuring angles to it from known points, instead of measuring the distance to the point directly. Active and Passive triangulation are discussed below.

4.2.6 Active Triangulation

Using work by May [8],the configuration of an active triangulation system can be seen in Figure 7. Figure 7 shows an active triangulation system that uses a light source such as a laser to illuminate a single spot on a target. The laser light hits the target and scatters in multiple directions. A position sensitive sensor is placed at a known lateral distance (b) from the light source. The (x) position where the reflected laser light hits the sensor and the focal length (f) allows the distance (d) to the object to be calculated using 2.1.1 as shown by May[8].

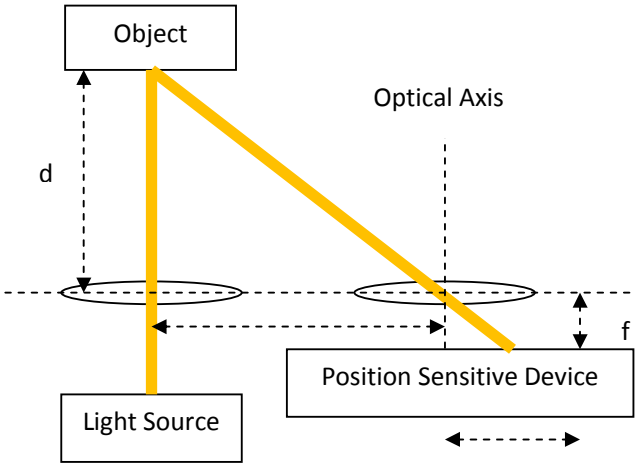

Figure 7 – Triangulation mechanism [8]

4.2.7 Advantages and Disadvantages

The system can only measure the distance to a single point at any one time similar to TOF and PSTOF. If this method were to be used in a laser range scanning system to determine the size and shape of a target, the sensor or target must be moved and several measurements taken. An advantage of this method is has a resolution in the order of millimetres.

The main drawback with the use of active triangulation is the need to move the system to gather more than one point at a time which is more time consuming.

4.2.8 Passive Triangulation

Passive triangulation is the basic method behind human eye depth perception. The method works by using two overlapping sensors focussed on a shared overlapping field of view. "If a specific object point can be seen from the perspective from both receivers, it is possible to determine the distance *d* from the sensors by means of appearance in both images and the geometric properties of the sensor"[8]. A simple version of this method is shown in Figure 8 where the optical axes are parallel to each other and the base distance *b* is parallel with the sensors. Where f is the focal length, x_l *and* x_r are the positions where the reflected light is detected by the position sensitive device and *d* is the distance to the object being investigated.[9]

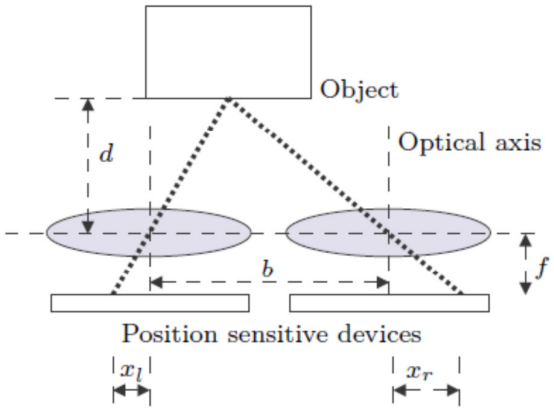

Figure 8 – Triangulation mechanism [8]

4.2.9 Advantages and disadvantages

May[8] states the two disadvantages of this method are “if the base line length increases (which is desirable for depth measurement precision) the area of overlap becomes smaller.” The converse is true of the baseline if the target being observed is close to the sensors. Also “the requirement for adjusting two exactly parallel optical axes is high”, if the base line or focal length changes while moving the two position sensitive devices the optical axes focal length will change, which can then have an effect when calculating the distance to the target [9].

The main drawback with the use of passive triangulation is the need to move the system to gather more than one point at a time which is more time consuming and also the need to constantly accurately adjust the light sensitive devices’ position exactly in order to maintain the same base distance between the two devices. If different scanning distances are required the base distances between the two light sensitive devices have to be moved accordingly. This change in base distance needs to be controlled as mentioned above and increases the amount of time taken to gather the data.

4.2.10 Conclusion

If TOF, PSTOF, active triangulation, passive triangulation are compared it can be seen that they are all possible alternatives to gathering range measurements. The TOF and PSTOF LRS do not require the emitter of the laser light and the detector to move. Passive triangulation and active triangulation requires high levels of control to correctly maintain the base distance and keep the optical axis parallel. The increase in control required to maintain the base distance would require the use of other devices on the sensor suite payload. The need for other equipment could increase the weight in the sensor suite, which one the aims in Chapter 1 was to make the payload less than 1Kg

It can be seen that all four methods suffer from not being able to gather data from multiple position and without extra equipment to reposition the LRS. One method that can be used to solve this problem is to use a rotating mirror to project the light used in these methods onto multiple surfaces while keeping the equipment stationary.

4.3 Evaluation of Sensor Technology

Several methods for gathering range data have been briefly discussed in chapter 2 and also in more detail in Section 4.2. This section begins by describing a method to gather 3D data from a 2D laser range scanner before selecting a suitable laser range scanner and camera for the sensor suite.

4.3.1 A method to gather 3D data from a 2D sensor

This section looks how 2D COTS (Commercial Of The Shelf) laser range scanners can be used as a 3D laser range scanner and how to present the data.

4.3.2 2D Laser Range Scanner

To create a 2D laser range scanner a 1D laser range scanner uses a mirror which allows the scanners laser beam to be deflected at multiple angles (θ) and returns the gathered range data (r) which now be expressed in a polar coordinate system relative to the laser range scanner and from that a set of 2D range data can be reconstructed.

A polar coordinate system Figure 9 uses the distance from a fixed point and an angle from a fixed direction to describe a point on a plane. The fixed point is the pole and emanates from the origin, and the reference ray from the pole is in the fixed direction. To describe a point or coordinate in this polar system a radial coordinate (r) is required from the origin and also an angular coordinate (Θ), and is displayed in a coordinate pair (r, Θ).The radial coordinate is generally a non-negative value and the angular coordinate can be represented in degrees or radians.

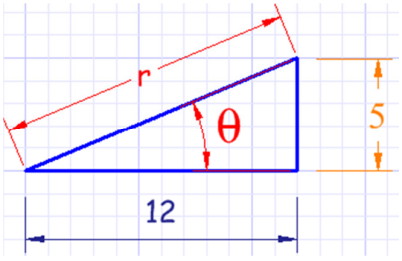

Figure 9 – Polar coordinate system

4.3.3 Discussion

A drawback when using a 2D range scanning configuration is that you can only scan in one horizontal plane. If the sensor were mounted on a UAV it requires repositioning after it scans an area, in order to gather 2D range data from a different area. A better method is to allow the sensor to scan in multiple directions (3D) from a fixed location in order for the sensor to gather as much range data before needing to be repositioned. This decrease in UAV repositioning extends the airborne inspection time allowing the UAV to inspect for longer periods of time.

4.3.4 3D Laser Range Scanner

To allow the laser range scanner to scan in multiple directions (3D) from a single location a laser range scanner is required to rotate around a specific axis. An investigation performed by Wulf and Wagner [10] in 2003 examined the possible configurations that can be used to create a 2D range scanner using a 2D range scanner rotated around an axis (Figure 10). The methods for gathering data are pitch, roll and yaw scanning. The paper shows that the rolling scan provides the most measured data points in the area of interest when compared to the pitch and yaw scans. Wulf and Wagner [10] explain that in applications the use of regular structured vertical columns and horizontal rows may be computationally easier to handle while performing segmentation and object detection. To increase the sensor suite's ability to gather large amounts of range data pitch scanning is used with yaw rotation of the sensor suite as required. The use of a yaw rotation allows the sensor suite to gather range data that can possibly be occluded from a frontal field of view. To implement the pitch and yaw rotation of the 2D LRS control of its orientation is required.

An advantage of using 3D range scanning configuration in contrast to a 2D configuration is that you are maximising the location scanning potential of the sensor by allowing the LRS to be repositioned without the need for the UAV to reposition and perform more scans. This will increase the scanning rate of the 3D sensor suite, which will be able to gather more data before needing to be repositioned. This decrease in need for the UAV to reposition can extend the airborne inspection time allowing the UAV to inspect for longer periods of time.

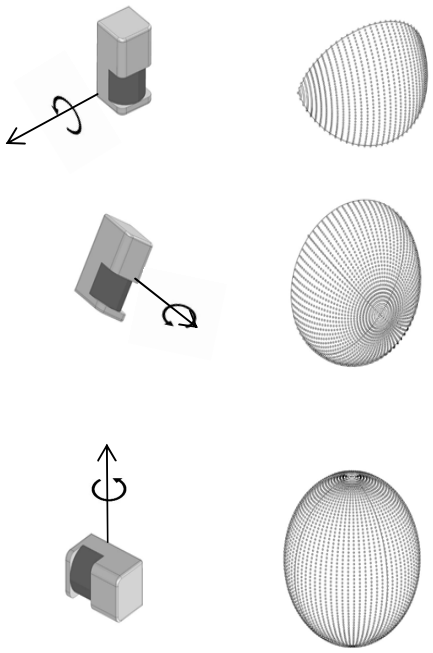

Figure 10 – Orientation of a 2D range scanner to create 3D point cloud. a) Pitch scanning, b) Roll scanning, c) Yaw scanning [10] **O. Wulf and B. Wagner (2003).**

4.3.5 LRS and Camera Selection

This subsection will define the UAV specifications to allow for suitable sensors to be selected to perform interior building inspections. After which several COTS LRS and cameras will be evaluated for use in the sensor suite. Suitable devices that meet the specifications for the sensor suite in chapter 1 and also meet the requirements of the UAV will be selected for use in the sensor suite.

4.3.6 Requirements for the UAV

To achieve the requirements for the UAV discussed below, a suitable sensor suite is required. Referring back to the aims in chapter 1, the payload of the UAV must be able to measure physical dimensions and also allow for visual defect analysis of a target. This sensor suite payload is then made up of a set of sensors that can perform the tasks described. The sensor suite is then suitably tested to ensure that it meets the aims of the project seen in chapter 1.

The sensor suite mounted on the UAV should accommodate the selected sensors to perform indoor building inspection. As well as this the sensor suite should allow for pitch and yaw degrees of freedom, to allow for 3D LRS scanning and image capturing as described in 4.3.4.

The equipment chosen to achieve the sensor suites aims is also be evaluated against the aims in chapter 1 and are briefly recapped.

- After discussions with the client, it was decided that the overall total mass of the UAV should not exceed 1Kg. The heavier the UAV is the more power the motors require to achieve lift which in turn means that there is a need to increase the battery power which in turn increases the weight. This then reduces the amount of flying time for the UAV.

- The UAV should be small to allow access to enclosed areas. The sensor suite should therefore be small to reduce the overall size of the UAV.

- The UAV should have an integrated multi modal sensor suite which can supply several in-flight functions, such as measurement of physical dimensions and provision of images to accompany the measurement data for visual analysis.
- The power consumption of the sensor suite should be low as practicable to increase airborne inspection time.

- The UAV airborne inspection time should be around 15-20 minutes. After talking with Skyonix Ltd.[11], a company specialising in aerial systems it was seen that this is an achievable average flight time for a UAV with a 1Kg load.

4.3.7 Laser Range Scanners

When selecting a suitable device for use on the sensor suite for the UAV several options were researched and considered. This section will look at this selection process for LRS.

4.3.8 SICK LMS

The SICK LMS is a 2D laser range scanner and has different potential uses [5][12][13][14] and can be seen in Figure 11. The device uses a PTOF method to measure the distance to an object. The device uses an infrared laser wavelength of λ = 905nm and an internal rotating mirror controlled by a servo motor to deflect the pulsed laser beam. The SICK LMS can then scan in a 180° semi-circle in front of itself and depending on its settings can scan and gather data at angular resolutions of 0.25°, 0.5° and 1° respectively. The measurement resolution of the a SICK LMS is 10mm with a maximum detection

range of 10m to 30m depending on the model. The data is then available in real time via RS232 and RS422 interfaces allowing the measurement to be evaluated and further post processed.
The size of the SICK LMS varies depending on the specific device. A LRS model regularly used in robotics [12][13][14]is the SICK LMS 200. It has a size of 185 x 156 x 210mm (width x depth x height) and the power supply required by this device is 24V ±15%. Due to its size, weight and power requirements this device is used by medium or large robotic systems[14][15]. Some of the specifications of the SICK LMS 200 can be seen in Table 4.

Figure 11 – SICK LMS

Angular Resolution	Step angle : 0.25, 0.5 and 1°
Accuracy	±20mm
Range	1 – 80m
Scan Time	53ms, 26ms, 13ms per scan at 0.25°, 0. 5° and 1° angular resolution, respectively.
Dimensions (WxDxH)	185mm x156mm x 210mm
Mass	4.5Kg
Power Supply	24V DC ±15% 1.8A
Light Source	Infra-red Laser (905nm)

Table 4 – Specifications of SICK LMS [5]

4.3.9 Hokuyo URG-04LX

The Hokuyo URG-04LX is a 2D scanning range finder [16] has been used in several applications [16][17] [18] and can be seen in Figure 12. The device uses a PSTOF method to measure the distance to an object. The device uses an infrared laser wavelength of λ = 785nm and an internal rotating mirror controlled by a servo motor to deflect the laser beam. The URG-04LX can then scan in a 240° semi-circle area in front of itself and has an angular resolution of 0.36° which requires 100ms to scan a line of points on the 240° semi- circle. The measurement resolution of the URG-04LX is 1mm with a maximum detection range of range 4.095m as a result of the encoding technique using a maximum of 12 bits. The data is then available in real time via RS232 and Universal Serial Bus USB interfaces allowing it to be evaluated and further post processed. The size of the URG-04LX is 50 x 50 x 70mm (width x depth x height) and has a weight of approximately 160g without any additional accessories or mountings. The power supply required for this device is 5V ±5%. Due to its low size, weight and power requirements this device is used by small or medium robotic systems[8][17][19]. Some of the specifications of the URG-04LX can be seen in Table 5.

Figure 12 – Hokuyo URG-04LX

Angular Resolution	Step angle : 0.36°
Accuracy	±10 mm (20 – 1000mm) ±2% of distance (1000mm – 4095mm)
Range	20mm – 4095mm
Scan Time	100msec per scan
Dimensions (WxDxH)	50mm x 50mm x 70mm
Mass	170g

Power Supply	5V DC ±5% 500mA
Light Source	Infra-red Laser (785nm)

Table 5 – Specifications of URG-04LX [6]

4.3.10 Comparison of SICK LMS and Hokuyo URG-04LX

Both the SICK LMS and URG-04LX each have attributes that are beneficial to undertake indoor building inspection whilst mounted on a UAV. The SICK LMS has a lower scanning time when compared to the Hokuyo URG-04LX, with the ability to change the angular resolution depending on the situation and a range of up to 80m. The Hokuyo URG-04LX on the other hand has advantages over the SICK LMS. The amount of power required by the Hokuyo URG-04LX is lower than the SICK LMS, the physical dimensions of the Hokuyo URG-04LX are also lower than the SICK LMS, and the mass of the Hokuyo URG-04LX is 5% of the SICK LMS. The mass, physical dimensions and the sensor suites sensor functions in the specification along with power requirements are some of the key factors to take into account when selecting the device to be mounted on the UAV. When the URG-04LX is compared to the SICK LMS the differences in operating range and resolution are clear, but the advantages in the SICK LMS require better internal optical devices to achieve the increased range and accuracy. These internal devices require more power to work and an increase in power supply demand is required by the SICK LMS. The increase in internal optical devices and required power supply increase the mass of the SICK LMS by a significant amount. This increase in mass can lead to a greater amount of thrust being required to keep the UAV airborne while undertaking the indoor building inspection. The motors which provide the upward thrust would have to spin quicker in order to overcome the increase in weight of the UAV, the battery would then be more quickly expended in trying to keep the UAV airborne as well as the SICK LMS powered, reducing the amount of flying time available for inspection before a battery change would be required.
From the comparisons drawn above it is clear that the URG-04LX is the best choice for a LRS in the sensor suite that is to be mounted on a UAV for this project, this is due to its smaller mass, smaller physical dimensions, lower power consumption, and an operating range of less than 5M.

4.4 Camera Selection

When selecting a suitable camera for use on the sensor suite for the UAV several options were researched and considered. This section will look at this selection process for cameras.

4.4.1 Microsoft LifeCam VX-500

The VX-500 camera is a small and lightweight digital camera capable of providing still and moving images. The camera uses CMOS technology. CMOS technology uses less power than CCD technology and due to the nature of its construction CMOS device tend to be cheaper to produce than Charge Coupled Devices (CCD)[20][21]. The physical dimensions are similar to that of the URG-04LX, with the VX-500 (Table 6) having a small mass meets the requirements of the UAV.

Sensor Type	CMOS Technology
Resolution	640 x 480
Physical Dimensions (L x D x H)	45mm x 45mm x 15mm
Mass	45 grams
Interface	High Speed USB with USB 2.0

Table 6 – Specifications of Microsoft LifeCam VX-500

Figure 13 – Microsoft LifeCam VX-500

4.4.2 Fire-i

The Fire-i is a small and lightweight digital camera capable of providing still and moving images. The Fire-i has a low weight and small physical dimensions both meet the requirements of the UAV. The resolution (Table 7) is the same as the Microsoft LifeCam VX-500 and uses CCD technology.

Sensor Type	CCD Technology
Resolution	640 x 480
Physical Dimensions (L x D x H)	62mm x 62mm x 35mm
Mass	60 grams
Interface	IEEE-1394a (FireWire)

Table 7 – Specifications of Fire-i

Figure 14 – Fire-i

The cameras discussed in this chapter both have qualities suitable for use in the research as devices to capture visual images of targets while performing indoor building inspections. Both cameras have the same resolution, the Fire-i uses CCD which produces "high-quality low noise images" and the VX-500 using CMOS technology to capture the digital image. The following equation was used to score each camera to decide which one to use based on three factors, weight, volume and cost.

$$\boldsymbol{Mass(Kg)} * \boldsymbol{Volume}\left(\boldsymbol{M^3}\right) * \boldsymbol{Cost}(£) \qquad \textbf{38}$$

The VX-500 scored a value of 27 and the Fire-I a value of 532. The two main differences between the two cameras were the lower weight and also smaller size which better meet the requirements of the UAV and therefore the VX-500 was selected.

4.5 Conclusion

In this chapter methods used by laser range scanners to gather range data from a scene and the mathematical descriptions of each method have been discussed. A method for using 2D laser range finders to gather 3D range data has also been discussed.

The requirements of the UAV system have been discussed which has led to a comparison of currently available laser range scanning devices and cameras. From these discussions it has been decided to gather range data using the URG-04LX due to its smaller physical dimensions, weight and

power consumption. After reading work done by Ohya et al.[19] and Ueda et al.[17] that shows how theURG-04LX has been previously used it was decided that the URG-04LX was the most suitable LRS to use. The range data will be gathered using the URG-04LX will then be processed to create a 3D point cloud of the scanned environment.

The Microsoft LifeCam VX-500 has been selected to gather visual images to help the user detect any visual defects on the target.

4.6 References

[1] S. Jain, “A survey of Laser Range Finding,” *Unpubl. Pap. Accessed March*, pp. 1–14, 2003.

[2] M.-C. Amann, T. Bosch, M. Lescure, R. Myllylä, and M. Rioux, “Laser ranging: a critical review of usual techniques for distance measurement,” *Opt. Eng.*, vol. 40, no. 1, p. 10, 2001.

[3] N. C. Barford, *Experimental Measurements: Precision, Error and Truth*, Second. Wiley-Blackwell, 1985, pp. 37 – 39.

[4] L. I. of America, “American National Standard for Safe Use of Lasers,” *Laser Institute of America, Orlando*. Laser Institute of America, 2000.

[5] SICK, “LMS200/211/221/291 Laser Measurement Systems Technical Description,” 2012. [Online]. Available: www.sick.com/group/EN/home/products/product_portfolio/laser_measurement_systems/Pages/laser_measurement_technology.aspx. [Accessed: 03-Feb-2010].

[6] L. Hokuyo Automatics Co, “Scanning Laser Range Finder Documentation,” *Hokuyo Automatic LTD*, 2005. [Online]. Available: http://www.hokuyo-aut.jp/02sensor/07scanner/download/products/urg-04lx/data/URG-04LX_spec_en.pdf. [Accessed: 02-May-2010].

[7] Bangor University, “Occupational Health and Safety Unit Guidance note,” vol. 27, no. July, 2005.

[8] S. May, “3D Time-of-Flight Ranging for Robotic Perception in Dynamic Environments,” University Osnabruck, 2009.

[9] B. Zhang, *Three-dimensional Laser-assisted Image Analysis for Robotic Surface Operation with Camera-space Manipulation*. Paris: ProQuest, 2007, pp. 16–17.

[10] O. Wulf and B. Wagner, “Fast 3D scanning methods for laser measurement systems,” in *Proceedings of the International Conference on Control Systems and Computer Science*, 2003, no. section 2, pp. 3–8.

[11] Skyonix Ltd., “Personal communication.” 2013.

[12] S. Hussmann, D. Schauer, and B. MacDonald, “Integration of a 3D-TOF camera into an autonomous, mobile robot system,” in *Instrumentation and Measurement Technology Conference, 2009. I2MTC ’09. IEEE*, 2009, pp. 547–552 ST – Integration of a 3D–TOF camera into .

[13] C. Ye and J. Borenstein, “A Novel Filter for Terrain Mapping With Laser Rangefinders,” *IEEE Trans. Robot.*, vol. 20, no. 5, pp. 913–921, Oct. 2004.

[14] M. Montemerlo, J. Becker, S. Bhat, H. Dahlkamp, D. Dolgov, S. Ettinger, and D. Haehnel, “Junior: The stanford entry in the urban challenge,” *J. F. Robot.*, vol. 25, no. 9, pp. 569–597, 2008.

[15] M. Montemerlo and S. Thrun, “Large Scale Robotic 3D Mapping of Urban Structures,” in *Experimental Robotics IX*, vol. 21, M. H. Ang and O. Khatib, Eds. Berlin/Heidelberg: Springer-Verlag, 2006, p. pp 141–153.

[16] L. Hokuyo Automatics Co, “URG-04LX Home Page.” [Online]. Available: http://www.hokuyo-aut.jp/02sensor/07scanner/urg_04lx.html. [Accessed: 03-Feb-2010].

[17] T. Ueda, H. Kawata, T. Tomizawa, A. Ohya, and S. Yuta, “Visual Information Assist System Using 3D SOKUIKI Sensor for Blind People, System Concept and Object Detecting Experiments,” in *IEEE Industrial Electronics, IECON 2006 - 32nd Annual Conference on*, 2006, pp. 3058–3063 ST – Visual Information Assist System U.

[18] Przemysław Łabęcki, D. Rosiński, and P. Skrzypczyński, “Terrain map building for a walking robot equipped with an active 2D range sensor,” *J. Autom. Mob. Robot. Intell. Syst.*, vol. 5, 2011.

[19] A. Ohya, S. Yuta, T. Yoshida, E. Koyanagi, T. Imai, S. Kitamura, A. Takeuchi, and T. Minamikawa, “Development of inspection robot for under floor of house,” in *Robotics and Automation, 2009. ICRA ’09. IEEE International Conference on*, 2009, pp. 1429–1434.

[20] R. deGaris Doble, *The Everything Digital Photography Book*, 2nd ed. Everything Books, 2008, pp. 100 – 101.

[21] A. Lustica, “CCD and CMOS image sensors in new HD cameras,” in *ELMAR, 2011 Proceedings*, 2011, no. September, pp. 133 – 136.

Chapter 5 Range Scan Geometry and Processing

5.1 Introduction

This chapter describes a method for processing the 2D range scans into a 3D point cloud. The first section describes how the 2D range data is converted into 3D Cartesian range data. The second section describes a program which mathematically describes the position and orientation of a target with reference to a world coordinate position. The third section describes how the 3D data is displayed to the user. This chapter describes original contributions made by the author in order to process and display the range data that is gathered from the project.

5.2 Distance Measurement Processing

After the test rig has gathered data from the target and also the "simulated" UAV's position the data needs to be processed from multiple 2 dimensional scans into a single 3 dimensional multiple scan point cloud. This involves processing multiple 2 dimensional scan data to create a single point cloud based around a world coordinate system. The next stage is to use the methods discussed in chapter 3 for describing position and orientation of an object in 3 dimensional space to facilitate the processing of the gathered data. A Matlab program was created to process the data gathered from the test rig. This involves reading the data in from an external file source, converting the raw data into an array, and then creating and displaying a 3D point cloud of the data with reference to a world coordinate system. The program for processing the raw data collected directly from the LRS into an organised system that calculates the range relative to a world coordinate system is called "rfinder.m". The program for plotting the processed data from "rfinder.m" into a 3D point cloud suitable for the end user is called "PtoC.m".

5.3 Transformations from Target to World

This section describes the transformations between the target in a polar coordinate system and the world axis in a Cartesian coordinate system. This allows the post processing of the data gathered by the LRS from a 2D representation of the target into a 3D representation of the target.

5.3.1 Processing Laser Range Finder Raw Data to World Coordinate System

The aim of this program is to process the data gathered from the URG-04LX from raw data into a Cartesian coordinate system with reference to a “world” coordinate system.

From the specifications of the URG-04LX [1] each scanning arc has a range of up to 240° Figure 15 with each individual laser beam separated by 0.36°. This then gives 750 individual laser points. The beam numbered 384 is at 0° [1]in the scanning arc, which allows the angle at which the individual laser beams leave the URG-04LX to be calculated. The raw data gathered by the URG-04LX is represented by an incident angle and a range value which constitutes a Polar coordinate system. As the entire payload on the test rig can gather scans at varying yaw and pitch angles the pitch and yaw angles that the payload gathers data at is also recorded. The elevation of the UAV and its position in space around the target are also recorded.

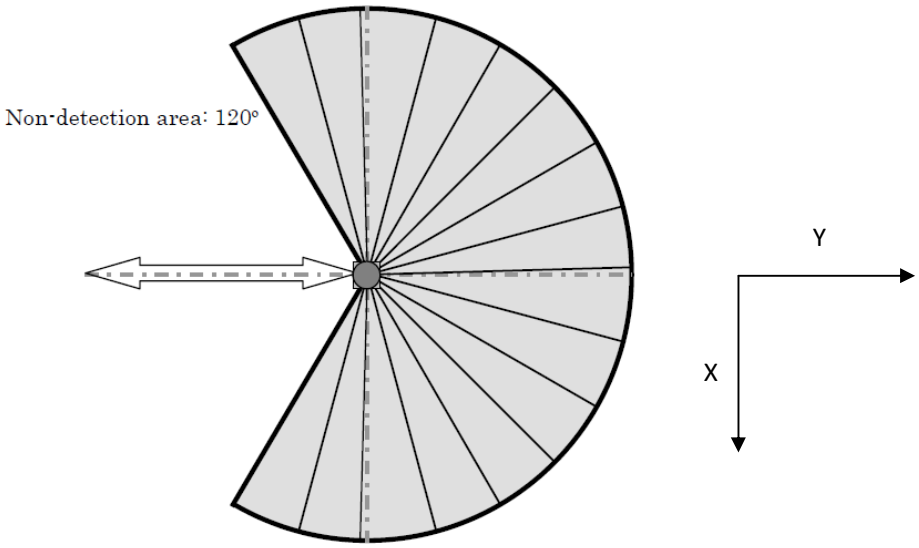

Figure 15 – URG-04LX 240° FOV [1]

Using a right handed orientation system to define a World Origin coordinate system {W}, as the X axis is positive to the right, the Z axis is positive upwards and the Y axis is positive in the forward direction and perpendicular to the X and Z axis.

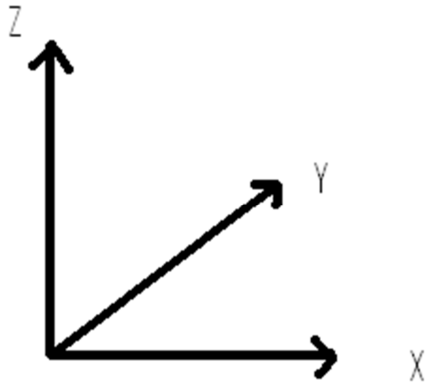

Figure 16 – {W} World Coordinate System

The target can be thought of as being described in the world coordinate system {W} by transforming the data from its own coordinate system called Target Origin {T} Figure 17.

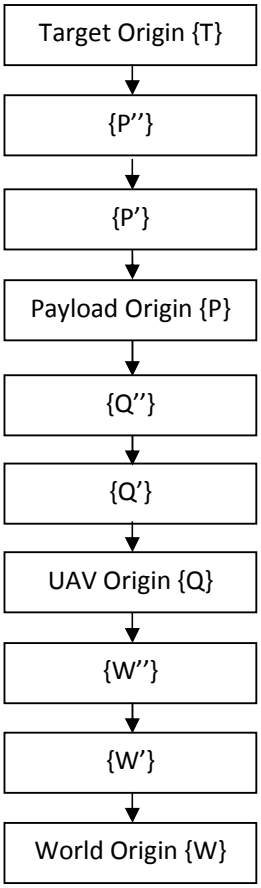

Figure 17 – Flow Diagram of Coordinate System

Where:

Target Origin {T} at the centre of the target

Payload Origin {P} at the centre of the URG-04LX

UAV Origin {Q} at the UAV centre of mass

World Origin {W} at the base of pitch goniometer

If the test rig had only the payload origin coordinate system and also the target origin coordinate system it could describe {T} with respect to {P}. As there are fixed and variable displacements that offset specific parts of the test rig which are not controlled by either {T} or {P} which in turn have an effect on {P} a more complex model describing the position of {T} relative to {W} to account for these other test rig parts is required. This system can be visualised in Figure 18.

Breaking Figure 18 into sections analysis of each coordinate system and its coincidence to other coordinate systems can be performed.

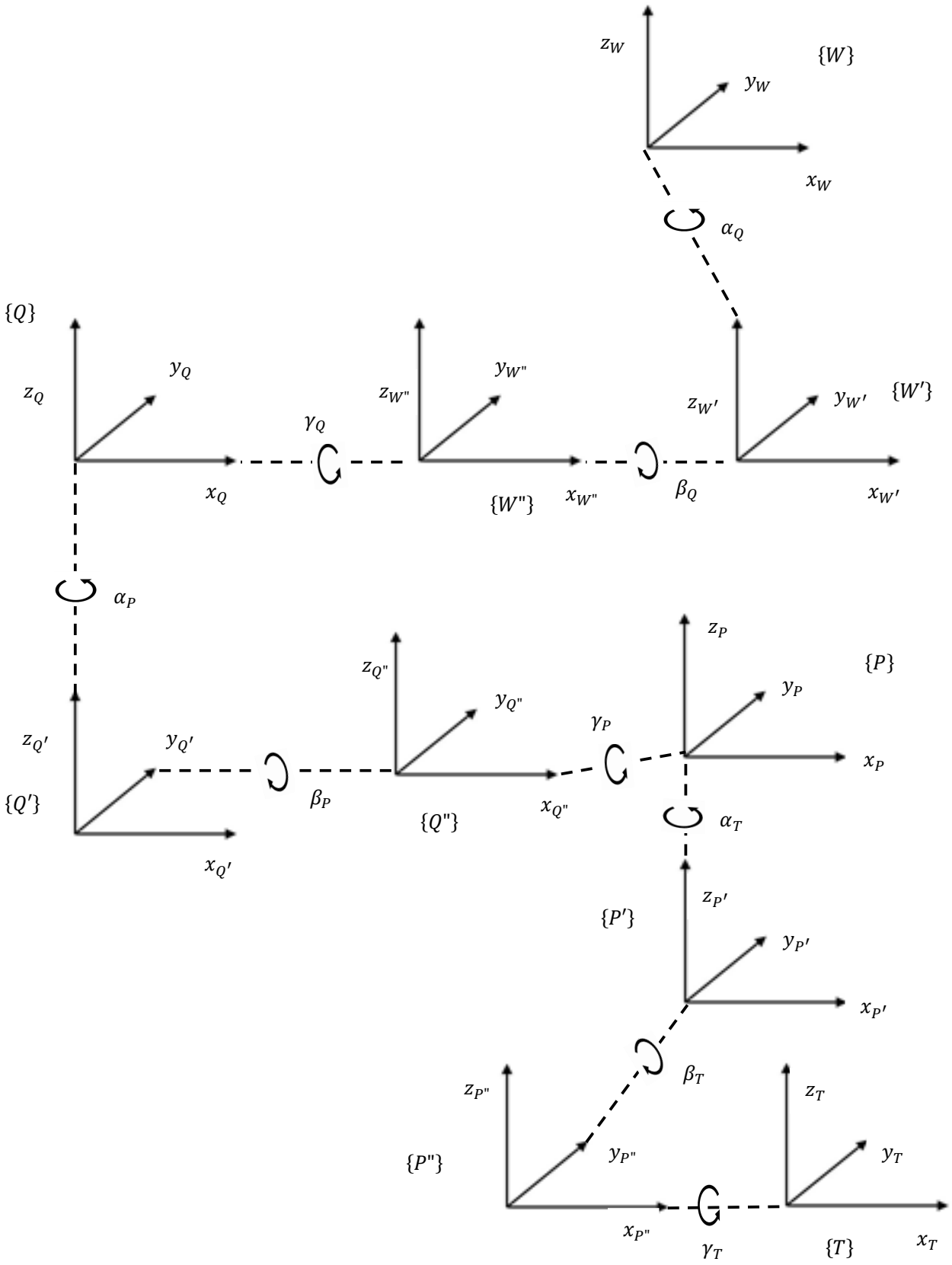

Figure 18 – Showing how to relate the Target {T} to the {W} World Coordinate System

5.3.2 {T} Target Origin to {P} Payload Origin

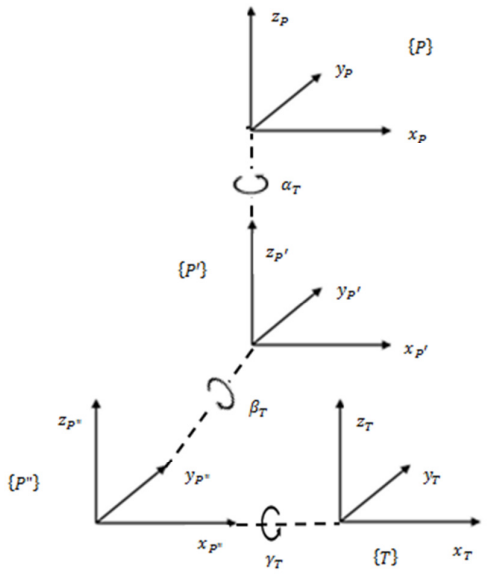

Figure 19 – {T} to {P} Coordinate System

To understand the coincidence between {P} and {T} coordinate systems some things need to be stated.

- The beam centre of the URG-04LX mounted on the payload is aligned along X_p. The scan from the URG-04LX is on the X_p, Y_p plane. The entire scan is centred around Z_p.
- The target being scanned must lie in the X_p, Y_p plane as that is the only sensitive plane of the sensor.
- α_T is the angle of the beam which is aligned with X_p, with respect to the beam centre which is aligned with X_p.
- X_p',Y_p' is rotated by α_T from X_p, Y_p but is not displaced. The displacement along Z_p is zero.
- The beam origin from the URG-04LX does not displace and the beam has only one rotational degree of freedom. $\beta_T = 0$ and displacement along Y_p is zero. As $\{P'\}$ and $\{P''\}$are coincident.
- The laser beam emitted from the URG-04LX has one rotational degree of freedom (DOF) so $\gamma_T = 0$. The translation of $\{T\}$ along X_p'' with respect to $\{P''\}$is the range measured by the sensor.

In chapter 3 methods to express position and orientation of an object in 3D space were discussed. After choosing Z-Y-X Euler angles as the preferred method the position of the target in $\{T\}$can be

described in terms of the $\{P\}$coordinate system. Using the rotation equations in chapter 3 the target's position and orientation can be described with respect to $\{T\}$.

An example of describing the position and orientation of a target can be seen below using $\{\boldsymbol{T}\}$and $\{\boldsymbol{P}\}$ as example frames. The description of the target's position vector with respect to some other frame $\{\boldsymbol{P}\}$ is known. Its description with respect to another different frame $\{\boldsymbol{T}\}$ can also be described. The original frame $\{\boldsymbol{P}\}$ is not coincident with frame $\{\boldsymbol{T}\}$ but has a general vector offset. The vector that describes $\{\boldsymbol{P}\}$'s origin is called ${}^{\boldsymbol{T}}\mathbf{Pos}_{\boldsymbol{BORG}}$. $\{\boldsymbol{P}\}$ is rotated with respect to $\{\boldsymbol{T}\}$ and is described by ${}^{\boldsymbol{T}}_{\boldsymbol{P}}\boldsymbol{R}$ as shown in chapter 3. As ${}^{\boldsymbol{P}}\mathbf{Pos}$ is know ${}^{\boldsymbol{T}}\mathbf{Pos}$ can be calculated as shown in Equation 39. The results of using Equation 39 are that the P's cancel leaving all the quantities as vectors written in terms of T (Equation 40).

$$\boldsymbol{T}_{\mathbf{Pos}} = {}^{\boldsymbol{T}}_{\boldsymbol{P}}\boldsymbol{R}\ {}^{\boldsymbol{P}}\mathbf{Pos} + {}^{\boldsymbol{T}}\mathbf{Pos}_{\boldsymbol{PORG}} \qquad \mathbf{39}$$

$$\boldsymbol{T}_{\mathbf{Pos}} = {}^{\boldsymbol{T}}_{\boldsymbol{P}}\boldsymbol{T}\ {}^{\boldsymbol{P}}\mathbf{Pos} \qquad \mathbf{40}$$

The mapping of one coordinate frame to another can then be considered as an operator in a matrix form. This allows us to write more compact equations and also is clearer than Equation 39. The use of the matrix form operator suggested in Equation 40 requires Equation 39 to be described as a $4 * 4$ matrix operator and also uses $4 * 1$ position vectors. Equation 40 can then have the structure of Equation 41. A 1 is added as the last element of the $4 * 1$ vectors and a row of [0 0 0 1] is added as the last row of the $4 * 4$ matrix.

$$\begin{bmatrix} {}^{\boldsymbol{T}}\mathbf{Pos} \\ \mathbf{1} \end{bmatrix} = \begin{bmatrix} & {}^{\boldsymbol{T}}_{\boldsymbol{P}}\boldsymbol{R} & & {}^{\boldsymbol{A}}\mathbf{Pos}_{\boldsymbol{PORG}} \\ \mathbf{0} & \mathbf{0} & \mathbf{0} & \mathbf{1} \end{bmatrix} \begin{bmatrix} {}^{\boldsymbol{P}}\boldsymbol{Pos} \\ \mathbf{1} \end{bmatrix} \qquad \mathbf{41}$$

This $4 * 4$ matrix is called a homogeneous transform and is used as a construction to cast the rotation and translation of the general transform into a single matrix form.

Starting with the target origin, which is the point at which the laser beam is reflected from the target to the URG-04LX.

$$q_T = \begin{bmatrix} 0 \\ 0 \\ 0 \end{bmatrix} in \{T\} \quad (42)$$

If we apply Equation 43, Equation 44 and Equation 45 to transform the target point into the payload coordinates using Equation 46, Equation 47 and Equation 48 where d is the measured range.

$$q_{P''} = {}^{P''}_{T}R(\gamma_T) q_T \quad (43)$$

$$q_{P'} = {}^{P'}_{P''}R(\beta_T)\, q_{P''} \quad (44)$$

$$q_P = {}^{P}_{P'}R(\alpha_T)\, q_{P'} \quad (45)$$

$${}^{P''}_{T}R(\gamma_T) = \begin{bmatrix} 1 & 0 & 0 & d \\ 0 & Cos\gamma_T & -Sin\gamma_T & 0 \\ 0 & Sin\gamma_T & Cos\gamma_T & 0 \\ 0 & 0 & 0 & 1 \end{bmatrix} \quad (46)$$

$${}^{P'}_{P''}R(\beta_T) = \begin{bmatrix} Cos\beta_T & 0 & Sin\beta_T & 0 \\ 0 & 1 & 0 & 0 \\ -Sin\beta_T & 0 & Cos\beta_T & 0 \\ 0 & 0 & 0 & 1 \end{bmatrix} \quad (47)$$

$${}^{P}_{P'}R(\alpha_T) = \begin{bmatrix} Cos\alpha_T & -Sin\alpha_T & 0 & 0 \\ Sin\beta\alpha_T & Cos\alpha_T & 0 & 0 \\ 0 & 0 & 1 & 0 \\ 0 & 0 & 0 & 1 \end{bmatrix} \quad (48)$$

As we have previously stated above that $\gamma_T = \beta_T = 0$ then Equation 43, Equation 44 and Equation 45 becomes Equation 49 to describe the vector q_T with relation to payload coordinate system.

$$q_P = {}^{P}_{P'}R(\alpha_T)\, {}^{P'}_{P''}R(\beta_T)\, {}^{P''}_{T}R(\gamma_T) q_T = {}^{P}_{T}R q_T \quad (49)$$

Where

$$\mathbf{R}(\boldsymbol{\gamma}_{\mathbf{T}}) = \begin{bmatrix} \mathbf{1} & \mathbf{0} & \mathbf{0} & \mathbf{d} \\ \mathbf{0} & \mathbf{1} & \mathbf{0} & \mathbf{0} \\ \mathbf{0} & \mathbf{0} & \mathbf{1} & \mathbf{0} \\ \mathbf{0} & \mathbf{0} & \mathbf{0} & \mathbf{1} \end{bmatrix} \quad \mathbf{50}$$

$$\mathbf{R}(\boldsymbol{\beta}_{\mathbf{T}}) = \begin{bmatrix} \mathbf{1} & \mathbf{0} & \mathbf{0} & \mathbf{0} \\ \mathbf{0} & \mathbf{1} & \mathbf{0} & \mathbf{0} \\ \mathbf{0} & \mathbf{0} & \mathbf{1} & \mathbf{0} \\ \mathbf{0} & \mathbf{0} & \mathbf{0} & \mathbf{1} \end{bmatrix} \quad \mathbf{51}$$

And since $R(\beta_T) = I$ then is simplified to Equation 52

$$\boldsymbol{{}^{P}_{T}R} = \boldsymbol{R(\alpha_T)}\ \boldsymbol{R(\gamma_T)} \quad \mathbf{52}$$

$$\boldsymbol{{}^{P}_{T}R} = \begin{bmatrix} \boldsymbol{Cos\alpha_T} & \boldsymbol{-Sin\alpha_T} & \mathbf{0} & \mathbf{0} \\ \boldsymbol{Sin\alpha_T} & \boldsymbol{Cos\alpha_T} & \mathbf{0} & \mathbf{0} \\ \mathbf{0} & \mathbf{0} & \mathbf{1} & \mathbf{0} \\ \mathbf{0} & \mathbf{0} & \mathbf{0} & \mathbf{1} \end{bmatrix} \begin{bmatrix} \mathbf{1} & \mathbf{0} & \mathbf{0} & \mathbf{d} \\ \mathbf{0} & \mathbf{1} & \mathbf{0} & \mathbf{0} \\ \mathbf{0} & \mathbf{0} & \mathbf{1} & \mathbf{0} \\ \mathbf{0} & \mathbf{0} & \mathbf{0} & \mathbf{1} \end{bmatrix} \quad \mathbf{53}$$

$$\boldsymbol{{}^{P}_{T}R} = \begin{bmatrix} \boldsymbol{Cos\alpha_T} & \boldsymbol{-Sin\alpha_T} & \mathbf{0} & \boldsymbol{dCos\alpha_T} \\ \boldsymbol{Sin\alpha_T} & \boldsymbol{Cos\alpha_T} & \mathbf{0} & \boldsymbol{dSin\alpha_T} \\ \mathbf{0} & \mathbf{0} & \mathbf{1} & \mathbf{0} \\ \mathbf{0} & \mathbf{0} & \mathbf{0} & \mathbf{1} \end{bmatrix} \quad \mathbf{54}$$

The above has shown how to calculate the rotation matrix from {T} with reference {P}.

5.3.3 Payload Origin {P} to UAV Origin {Q}

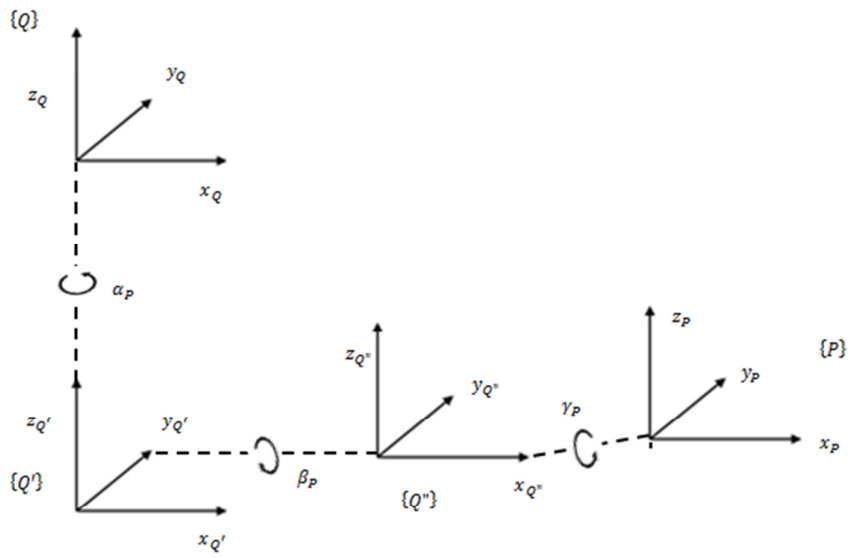

Figure 20 – {P} to {Q} Coordinate System

Using the same method as above, we can now describe the position of the target in terms of the payload origin coordinate system with reference to the UAV origin coordinate system.

$$\boldsymbol{q_Q} = {}^{Q}_{Q'}\boldsymbol{R}(\boldsymbol{\alpha_P})\ {}^{Q'}_{Q''}\boldsymbol{R}(\boldsymbol{\beta_P})\ {}^{Q''}_{P}\boldsymbol{R}(\boldsymbol{\gamma_P})\boldsymbol{q_P} = {}^{Q}_{P}\boldsymbol{R}\ \boldsymbol{q_P} \qquad 55$$

There are variables that need to be included in order to accurately describe the position of the payload.

- The centre of the URG-04LX is displaced along Z_Q from 0 $\{Q\}$
- The URG-04LX is also displaced sideways along the Y_Q, from 0 $\{Q\}$
- The URG-04LX is also displaced sideways along the $X_{Q''}$ from 0 $\{Q\}$

$$ {}^{Q''}_{P}R(\gamma_P) = \begin{bmatrix} 1 & 0 & 0 & dX_{Q''} \\ 0 & Cos\gamma_P & -Sin\gamma_P & 0 \\ 0 & Sin\gamma_P & Cos\gamma_P & 0 \\ 0 & 0 & 0 & 1 \end{bmatrix} \quad (56) $$

$$ {}^{Q'}_{Q''}R(\beta_P) = \begin{bmatrix} Cos\beta_P & 0 & Sin\beta_P & 0 \\ 0 & 1 & 0 & dY_{Q'} \\ -Sin\beta_P & 0 & Cos\beta_P & 0 \\ 0 & 0 & 0 & 1 \end{bmatrix} \quad (57) $$

$$ {}^{Q}_{Q'}R(\alpha_P) = \begin{bmatrix} Cos\alpha_P & -Sin\alpha_P & 0 & 0 \\ Sin\beta\alpha_P & Cos\alpha_P & 0 & 0 \\ 0 & 0 & 1 & dZ_Q \\ 0 & 0 & 0 & 1 \end{bmatrix} \quad (58) $$

The method above has shown how to calculate the transformation matrix from $\{P\}$ with reference$\{Q\}$.

5.3.4 UAV Origin {Q} to World Origin {W}

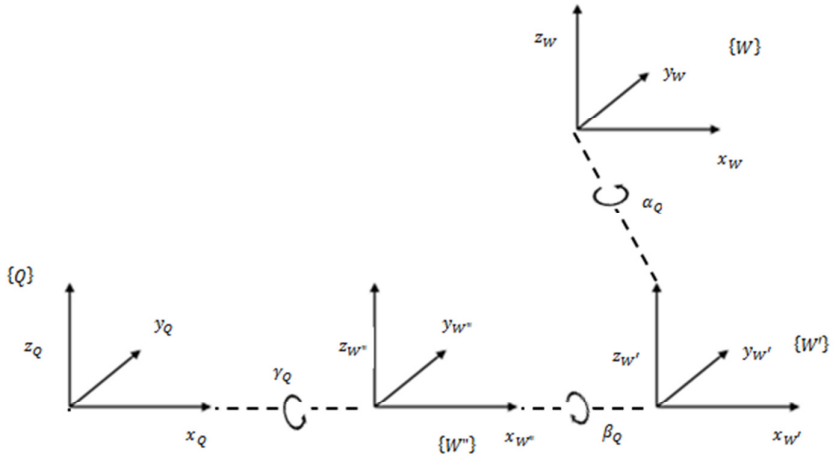

Figure 21 – {Q} to {W} Coordinate System

Using the same method as above, we can now describe the position of the target in terms of the UAV origin coordinate system with reference to the World origin coordinate system.

$$q_W = {}^{W}_{W'}R(\alpha_Q)\ {}^{W'}_{W''}R(\beta_Q)\ {}^{W''}_{Q}R(\gamma_Q)q_Q = {}^{W}_{Q}R\, q_Q \quad (59)$$

$${}^{Q''}_{P}R(\gamma_P) = \begin{bmatrix} 1 & 0 & 0 & dX_{W''} \\ 0 & Cos\gamma_Q & -Sin\gamma_Q & 0 \\ 0 & Sin\gamma_Q & Cos\gamma_Q & 0 \\ 0 & 0 & 0 & 1 \end{bmatrix} \quad (60)$$

$${}^{Q'}_{Q''}R(\beta_P) = \begin{bmatrix} Cos\beta_Q & 0 & Sin\beta_Q & 0 \\ 0 & 1 & 0 & dY_{W'} \\ -Sin\beta_Q & 0 & Cos\beta_Q & 0 \\ 0 & 0 & 0 & 1 \end{bmatrix} \quad (61)$$

$${}^{Q}_{Q'}R(\alpha_P) = \begin{bmatrix} Cos\alpha_Q & -Sin\alpha_P & 0 & 0 \\ Sin\alpha_Q & Cos\alpha_Q & 0 & 0 \\ 0 & 0 & 1 & dZ_W \\ 0 & 0 & 0 & 1 \end{bmatrix} \quad (62)$$

The method above has shown how to calculate the rotation matrix from {Q} with reference {W}.

5.4 Graphical Representation of Range Data in 3D

The aim of this program is to handle the processed data from rfinder.m and display it in a way that is useful to the user. The program will display the polar measurement data gathered on a graph filled with a 3D mesh overlaid on the data (Figure 22), this will allow the user to visualise the data before it is processed by the rfinder.m program. This view allows the user to spot any obvious anomalies in the data. The second graph the user will be presented with, is a graph with a surface mesh showing the 3D Cartesian coordinates (Figure 23) calculated by the rfinder.m program. This allows the user to visualise the target easily. The third graph the user will be presented with will display the same data as the previous graph but instead will display the data in a 3D point cloud rather than a mesh (Figure 24).

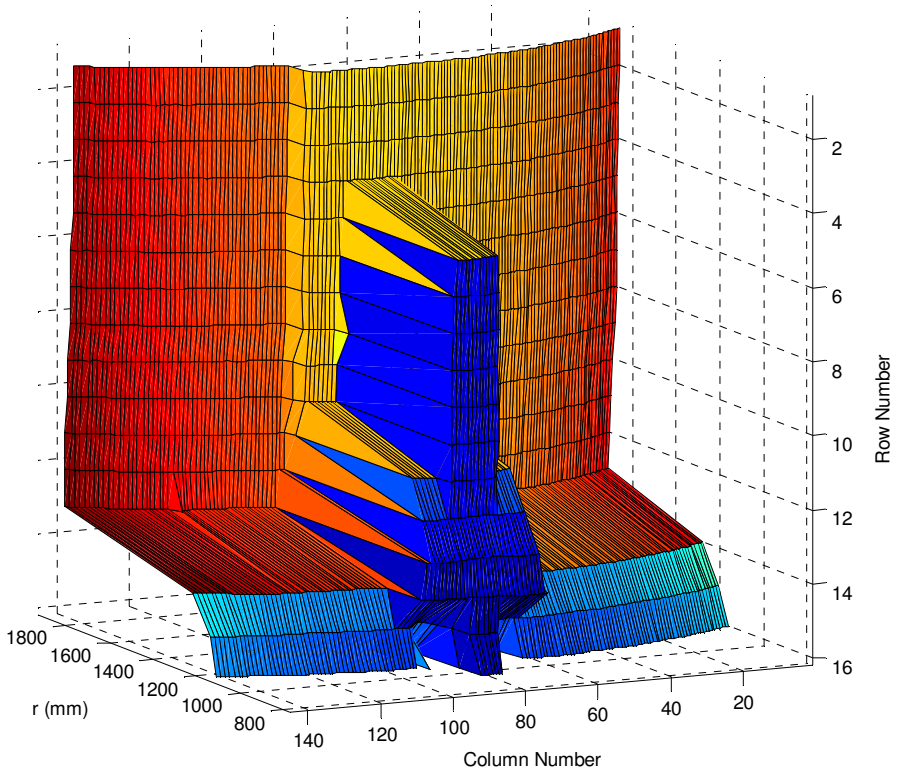

Figure 22 – Raw Range Data 3D Mesh in Columns and Rows

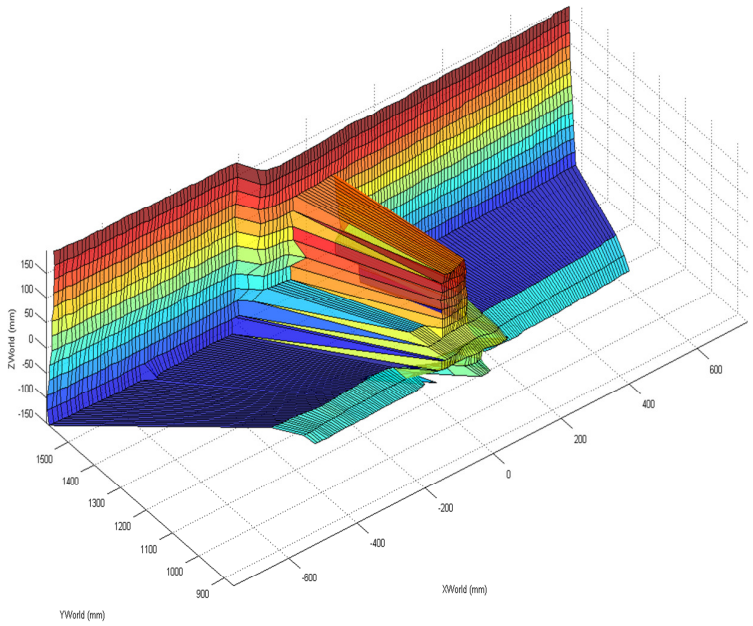

Figure 23 – Range Data 3D Mesh in Cartesian Coordinates

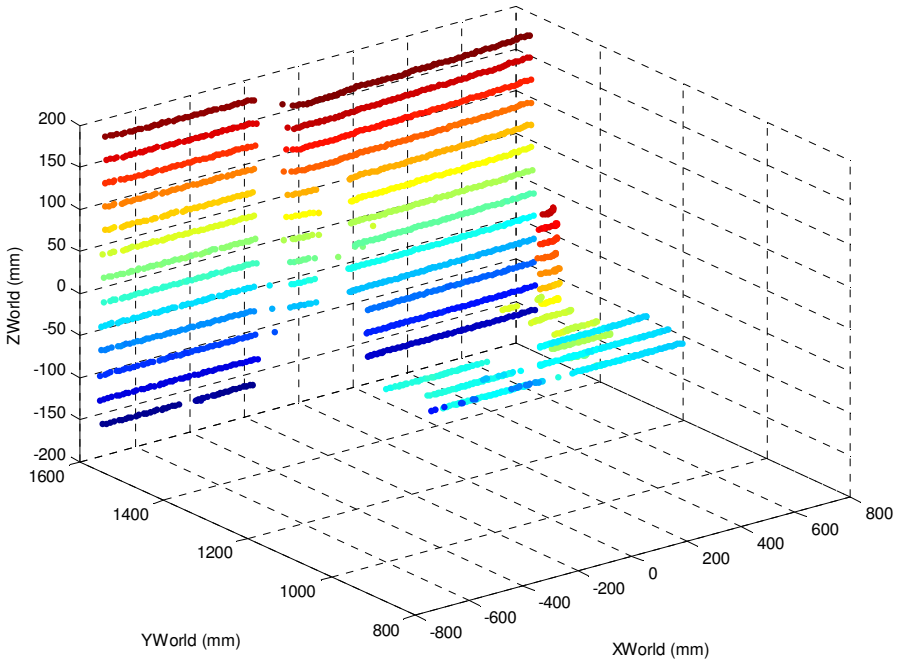

Figure 24 – Range Data Point Cloud in Cartesian Coordinates

5.5 Conclusion

This chapter has explained the how rfinder.m is used to describe the transformations between the target in a polar coordinate system and the world axis in a Cartesian coordinate system. This allowed the post processing of the data gathered by the URG-04LX to be converted from 2D representation of the target into a 3D representation of the target using PtoC.m. To check how accurately rfinder.m worked experiments are performed and the results shown in chapter 6

5.6 References

[1] L. Hokuyo Automatics Co, “Scanning Laser Range Finder Documentation,” *Hokuyo Automatic LTD*, 2005. [Online]. Available: http://www.hokuyo-aut.jp/02sensor/07scanner/download/products/urg-04lx/data/URG-04LX_spec_en.pdf. [Accessed: 02-May-2010].

Chapter 6 1st Test Rig Design

6.1 Introduction

This chapter describes the test rig constructed for the project which is used to simulate a UAV in order to perform experiments to test the laser range scanner, camera and their ability to produce three dimensional point clouds and images. This chapter begins by describing both sensors mounted on the sensor suite. The sensor suite is mounted on a test rig and an experiment is performed to assess the ability of the sensor suite to create a 3D point cloud from multiple pitched 2D range scans. A second test rig is then developed to simulate a UAV performing indoor building inspections whilst allowing the sensor suite to gather multiple 2D range scans from different positions and orientations. The mechanical and electronic design of the second test rig is discussed. The second test rig is then tested to evaluate if it can simulate a UAV performing an indoor building inspection. This chapter describes original contributions made by the author.

6.2 Overview

To test if the sensor suite could be deployed on a UAV to perform an indoor building inspection a test rig is constructed to simulate the UAV's position as if it were conducting an indoor building inspection. A simulated UAV is then mounted to the test rig carrying the sensor suite. A real UAV has six degrees of freedom (roll, pitch, yaw, X, Y, Z) it was decided that for simplicity that the simulated UAV had be limited to three degrees of freedom, X, Y and Z. The sensors were mounted onto the sensor suite which was mounted on the simulated UAV. Both laser range scanner and camera are mounted on the same pivot point on the pitch axis. The sensor suite uses the pitch and yaw axes to allow the laser range scanner and camera to scan the target area without the need to move the entire UAV. This extends the amount of time the UAV stays in the air which would increase the amount of data that the UAV can gather before needing to land and have its batteries changed.

6.3 Hokuyo URG-04LX

In chapter 4 it was decided that the Hokuyo URG-04LX scanning range finder would be used in the sensor suite to gather range data.

The Hokuyo URG-04LX as described in chapter 4 is a LRS that uses an infrared laser that uses PSTOF in order to determine the range of a target object or area. This section will cover the how the URG-04LX gathers the data and also the command communication structure of the URG-04LX and how it displays the gathered data to the user.

Figure 25 shows a representation of the sensor's measurement field of view. The laser beam rotates in an anti-clockwise direction when viewed from the top of the device. The detection range (E) is the maximum angle the sensor can accurately scan for measurements. The angular resolution is the 360° view divided by 1024, the number of steps the optical mirror can be positioned at. Measurement points on the URG-04LX are referred to as steps, with step 0 being the first measurement point and the first measurement point used in the detection range is Step A as seen in Figure 25. Step B is the "sensor front step" and is the step directly in the middle of the detection range. Step C is the end measurement point of the detection range. Step D is the last measurement point. Below Figure 25 shows a visual representation and Table 8 shows the numerical values of the measurement parameters of the URG-04LX.

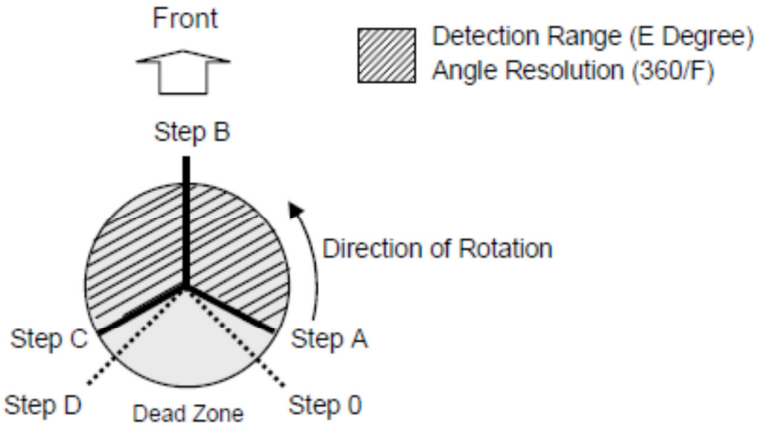

Figure 25 – FOV of URG-04LX

Step Name	Description	Step Number
Step 0	First measurement point	0
Step A	Initial measurement point in the detection range	44
Step B	Sensor front step	384
Step C	End point in the detection range	725
Step D	Last measuring point	768

Table 8 – Step measurement values

The amplitude of the laser light is modulated and the distance measurement is based on the detecting of the phase difference between the transmitted light from the source and the reflected light from the target object[1]. The range (D) to the target can be calculated using Equation 63, where the distance to the target object (*L)* is in Millimetres, phase difference (ϕ) in radians, frequency of the laser light emitted (*f*) in Hz and the speed of light (*v*) in Millimetres/Second.

$$\boldsymbol{D = \frac{1}{2} * \left\{ \frac{\phi}{\left(\frac{f}{v} * 2\pi \right)} \right\}} \qquad \textbf{63}$$

6.3.1 Data Encoding and Decoding

The URG-04LX's data is encoded to reduce the transmission time between host and sensor. The data is decoded by the host to reduce the need for more complex circuitry on the URG-04LX and keep weight, size and power requirements to a minimum. The host used was a desktop personal computer.

The URG-04LX is equipped with an RS232 and USB Communication Device Class (CDC) connection for interfacing with the host. The USB CDC connection allows the host to set up a virtual COM port to enable communications from the host to the device while offering the advantages of a USB connection, such as high speed transmission of data and a high data capacity. The test rig used the USB protocols to transmit the data from sensor to host as it is simpler to set up a good connection between host and sensor. The operating system can be told where to load the drivers for the device by the user, reducing the time taken to establish and maintain a connection to the sensor. In future systems the host would not be a personal computer, as a small microprocessor can perform the same functions on board the UAV.

The URG-04LX compares the phase shift of the transmitted and reflected waves as discussed in chapter 4 to determine the range data from a target. The phase of the light is converted from an analog signal to a digital signal using an analogue to digital converter. The data is then processed into ASCII characters to encode and transmit the host device. When the ASCII data is received at the host it can then be decoded to display the range to the target. To encode the data from the URG-04LX there are three types of encoding techniques applied depending upon the data size.

Two-Character Encoding
Three-Character Encoding
Four-Character Encoding

Two-Character Encoding is applied to data having a maximum length of 12 bits
Three-Character Encoding is applied to data having a maximum length of 18 bits
Four-Character Encoding is applied to data having a maximum length of 24 bits

In this research the commands not only receive range data, but also require extra characters telling the laser range scanner where to begin scanning from, where to stop scanning, the amount of scans to take, scan intervals and line feeds. To this extent three-character encoding is used in this research to represent all of this data. The encoding and decoding process used in the URG-04LX is discussed below.

6.3.2 Encoding

Encoding is achieved by first converting the decimal representation of the range in mm to binary. The binary data are then separated into higher, middle and lower bins which are each 6 bits long as shown in Table 9. The lower binary data set is then filled up with six bits first, with the middle data set being filled up next six bits and the higher bit last. The higher, middle and lower binary data is then converted into hexadecimal. The next step is to convert the hexadecimal data into ASCII characters for transmission to the host. This is done by the addition of 30 in Hexadecimal to each set data. This is done possibly to start at least at the zero character in ASCII which comes after the non-numerical characters. An example of encoding of range data can be seen below in Table 9.

189mm =	010111101		
Data Set	Higher	Middle	Lower
Sections in equivalent binary	0	10	111101
Convert to hexadecimal	0	2	3D
Add 30 in Hexadecimal	30	32	6D
Use look up chart to get ASCII character	0	2	m

Table 9 – Encoding conversion from 189mm in decimal to ASCII

6.3.3 Decoding

An example of decoding the range data can be seen below in Table 10. Decoding is achieved by separating the data into higher, middle and lower pieces of ASCII data which are each 1 character long and converted to their hexadecimal equivalent using the look up table. The next step is to subtract 30 in hexadecimal from each set of data. The data is then converted to its binary equivalent, and then the data was merged together as shown in Equation 64. The start of the higher data set was the most significant bit and the end of the lower data set was the least significant bit. The merged data was then converted into decimal and the value of range data was represented in mm.

$$(\mathbf{Higher} + \mathbf{Middle} + \mathbf{lower}) = \mathbf{HigherMiddleLower} \quad \mathbf{64}$$

02m =	30	32	6D
Data Set	Higher	Middle	Lower
Subtract 30 in hexadecimal	0	2	3D
Binary Equivalent	0	10	111101
Merge	010111101		
Decimal Equivalent	189 mm		

Table 10 – Example of Converting from ASCII to 189mm in decimal

6.4 Camera

To find a suitable device for the sensor suite in this project research was undertaken to compare other possible alternative methods to gather visual images as shown in chapter 4. After this research was undertaken the Microsoft LifeCam VX-500 was selected for use in the sensor suite. The Matlab Image Acquisition toolbox program "imaqtool" is used to control the VX-500. The Matlab function also allows for multiple images to be gathered based on a user input trigger and also export the visual image to a matlab workspace.

6.5 Mounting and Movement of the Sensor Suite on the UAV (1st Test Rig)

This sensor describes the first test rig created In order to create a suitable test rig to simulate the UAV performing an indoor building inspection a design for the mounting and movement of the sensor suite on the UAV was first proposed. This mounting for the sensor suite was then be evaluated.

After assessing possible mechanisms to pitch and yaw the sensor suite, it was decided to use a gimbal to pitch the sensor suite, with a goniometer to measure the angle at which the sensor suite was tilted. The gimbal allowed the sensor suite to pitch forward and backwards allowing the LRS to create a 3D point cloud. The camera has access to the same multiple pitch positions available to the LRS and allows for a visual and 3D point cloud data to be gathered. The gimbal mounting was then built to evaluate the viability of the idea with the purpose of creating a further prototype that allowed for the mounting of the gimbal onto a stepper motor in order to allow the sensor suite to perform yawing movements as well. A picture of the first test rig can be seen in Figure 26. The first test rig consisted of four pieces of stainless steel, adjustable screw gimbal and protractor. A vertical steel plate was used to provide the elevation to the gimbal to allow it to pitch freely. A 180° protractor was then mounted to the vertical steel plate and secured with a second piece of steel to act as the rotating pointer indicating the pitch angle of the sensor suite. This allowed for manual measurements of the pitch angle of the sensor suite and produces 3D point clouds with the LRS. The final pieces of metal made the mount for the sensor suite. This consisted of a piece of steel placed parallel to the floor and attached to the opposite end of the steel pointer.

The mount allows a single sensor to be mounted to the test rig in order to test its feasibility, with the aim of developing multiple mounting points for the other sensor if the first test rig works correctly.

Following the creation of the first test rig evaluation tests were performed to see if the method for pitching the sensor suite allows the sensor suite to gather multiple 2D data scans before creating a more complex test rig. An example of a 3D point cloud created from multiple 2D scans can be seen in Figure 27. The tests evaluate the ability of the test rig and LRS to create a 3D point cloud of a target object and also evaluated the camera's visual data gathered using the test rig. The data gathered using the test rig and sensors was then compared to the known dimensions by measuring the target objects.

6.5.1 1st Test Rig Specifications

- Allow for mounting of sensor suite
- Ability to pitch the sensor suite based upon a gimbal design
- Gather visual images and 2D LRS data
- Create a 3D point cloud with the multiple 2D LRS data

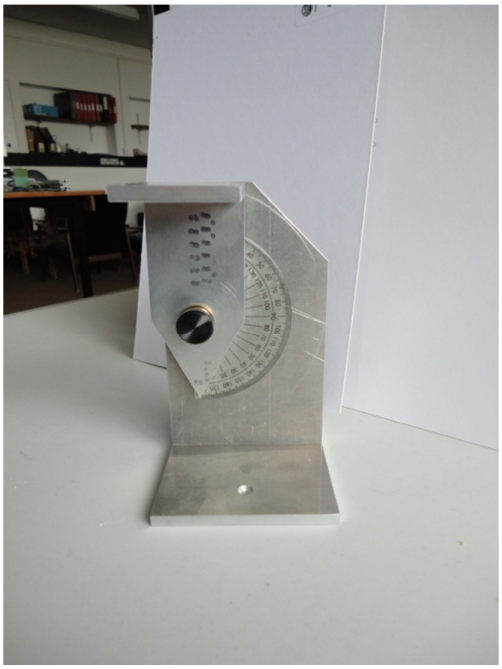

Figure 26 – 1st Test rig

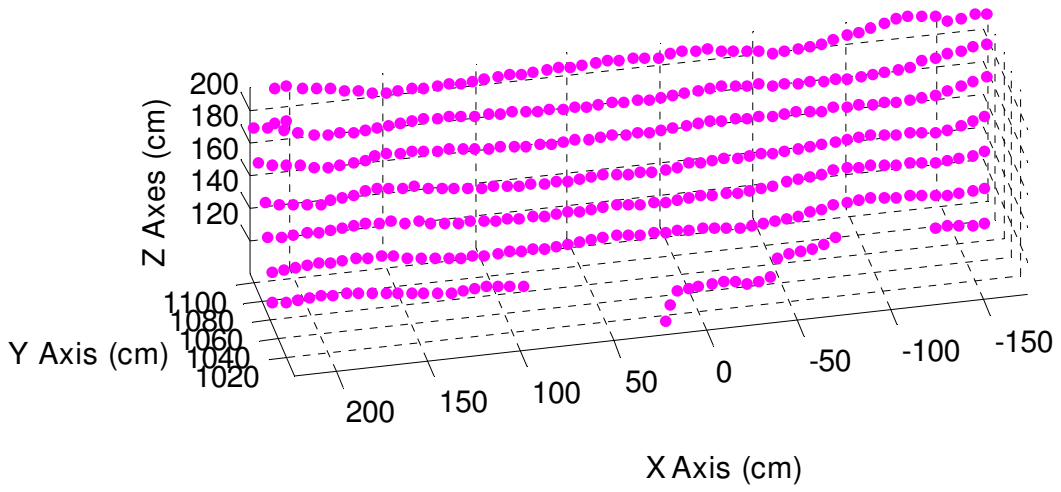

Figure 27 – An example showing LRS Measurements of a Wall in World Coordinates

6.5.2 Experimental Methods: 1st Test Rig

The experiment is designed to observe and evaluate the 1st test rig in order to test the ability of the 1st test rig to collect a series of 2D distance data and then create a 3D point cloud with the gathered data. The URG-04LX was mounted on the first test rig (Figure 28). The target used in this experiment was a card box with dimensions 140*100*90mm, (L*D*H). The test rig was then aligned to measure the distance from the device with an with a θ angle of 0°. The URG-04LX was directly in front of the target and at the starting point the pitch angle was 0°, the URG-04LX was parallel to the ground. The URG-04LX was then manually rotated in pitch using a goniometer from 0° to 14°. At each individual pitch angle the URG-04LX collected distance measurements from the target with a field of view (FOV) from the front most point of the scanner. The FOV used in this experiment was 21° from scan points 359-417 within the URG-04LX, both the FOV and pitch angle were used to provide enough measurement points to cover the width and height of the target and also a percentage of the background wall to compare the target against. The experimental set up are shown in Figure 28

Figure 28 – Experimental Set Up to Evaluate 1st Test Rig

The distance to the front face of the target is 860mm away from the front of the URG-04LX, with a wall at 1000mm behind the target. The URG-04LX is programmed to collect 1000 range data points at each pitch angle so that the average value could be used. The experiment was conducted in a room illuminated with fluorescent lamps. Before the test, the URG-04LX was turned on for a minimum of 140 minutes to allow the device a suitable warm up period as shown in chapter 8.

6.5.3 Results: 1st Test Rig

The experiment was performed as described above, the data is processed and presented in several different ways in Figure 29, Figure 30 and Figure 31.

Figure 29 shows the initial raw data collected by the URG-04LX mounted on the 1st test rig. The scan point refers to the step number within the URG-04LX that emitted the laser beam to scan the target. The pitch angle refers to the angle which the goniometer was set to while gathering the distance data. The distance data refers to the distance from the scanning point to the target, and is in polar coordinates. It can be seen that there is a large relatively flat “wall” at 1000mm, this “wall” is the back wall set behind the target so that a contrast of two different ranges could be seen easily. At 850-860mm on the Y axis a rectangular face can be seen in light blue and is the front face of the

box facing the URG-04LX. Above the front face of the box a second blue face which has a green, orange and red feature on top of a part of it. This second blue face is the top of the target box and the wave shows that there are different measurement values that have been recorded. This is a problem known as the mixed pixels problem. When the laser beam hits the very edge of a target, its range value is the combination of target in the foreground and also any target directly behind it. In this case the top of the box and the wall behind it. The range value returned then falls between the distances to the foreground and background or the target, as described in [2]. The laser scanner did not scan the entire top of the box and only scanned a small sample of it. This occurred due to the fact that there were not enough smaller pitch angles to measure the entirety of the roof of the box and instead the majority of the roof was not correctly scanned. Below the box faces there is a dark blue area which represents the parallel ground surface that the target was placed upon, this ground surface ran below the target and also all the way up to the base of the "wall" .

Figure 30 shows the data collected by the URG-04LX mounted on the 1st test rig after it was processed data by the PtoC.m program. The distance measurements, pitch angle, scan point and data about the goniometer have been used to create a Cartesian coordinate system which shows the measured distance data relative to a world axis defined by the user. The colours used in Figure 30 map to the height of the measured points. The front face of the box can be clearly seen around 860-870mm on the Y axis and the top of the box can be seen at 109mm on the Z axis stretching back to the "wall". Below the box faces there is a dark blue area which represents the parallel ground surface that the target was placed upon, this ground surface ran below the target and also all the way up to the base of the "wall" .

The values measured from the faces of the target in Figure 30 have a width of 100.21mm, height of 90.27mm taken from the front face. The depth of the target was measured from the front face of the target to the "wall" as the target was placed flat against the "wall". The measurements gathered showed that the "wall" was measured as being between 1085mm and 1127mm, and gives us a variance of 42mm which is larger than the actual "wall" distance of 1000mm by 85mm-127mm. Compared to the actual values of the target (100*140*90mm, (L*D*H)) the width and length measured values are within +0.3mm of the actual target values. The measured distance of the targets' depth was over estimated by 85-127mm compared to the actual target depth depending on which "wall" point was used. This error in the "wall" measurements has affected the depth value of the target, if the "wall" value is over the actual "wall" value then the depth of the target will be overestimated and vice versa.

The same measured data has also been displayed in a point cloud and can be seen in Figure 31. This method for displaying the data can seem redundant when compared to the mesh used in Figure 30 as it does not show the point clouds connected in a visually appealing way, but in some situations the mesh can obscure points of interest or display the data in an ambiguous manner. This is where the point cloud representation can overcome this problem as it allows the user to investigate specific areas or individual points without a “skin” or “mesh” obscuring the users view or skewing the user’s interpretation of the data.

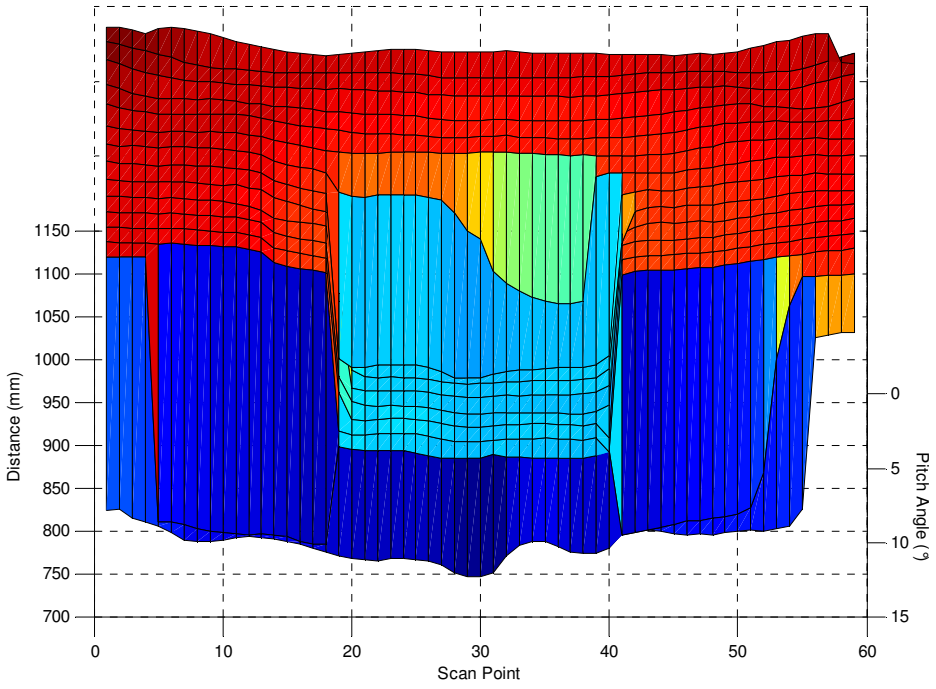

Figure 29 – Initial Scanner measurements in Polar co-ordinates

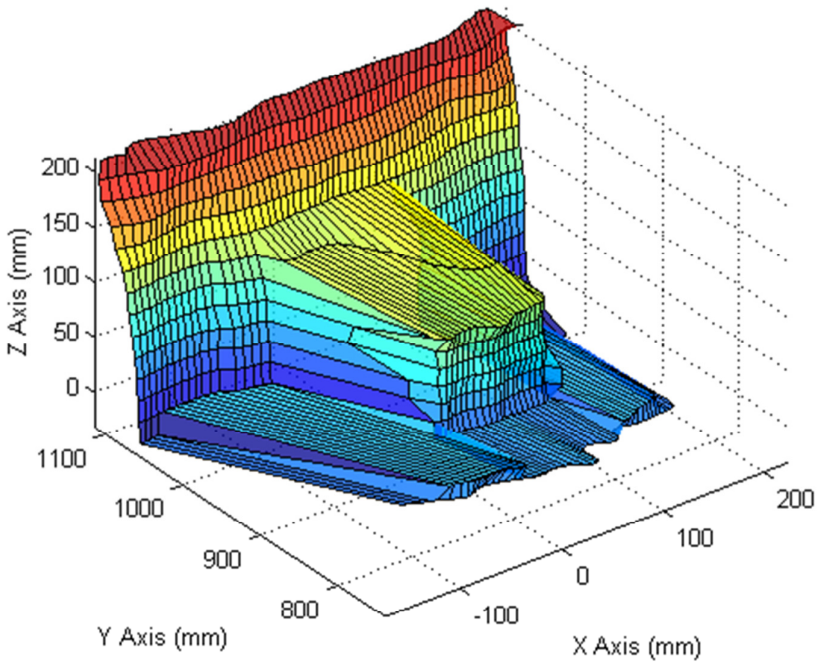

Figure 30 – LRS measurements with World Reference in Cartesian co-ordinates Surface Mesh

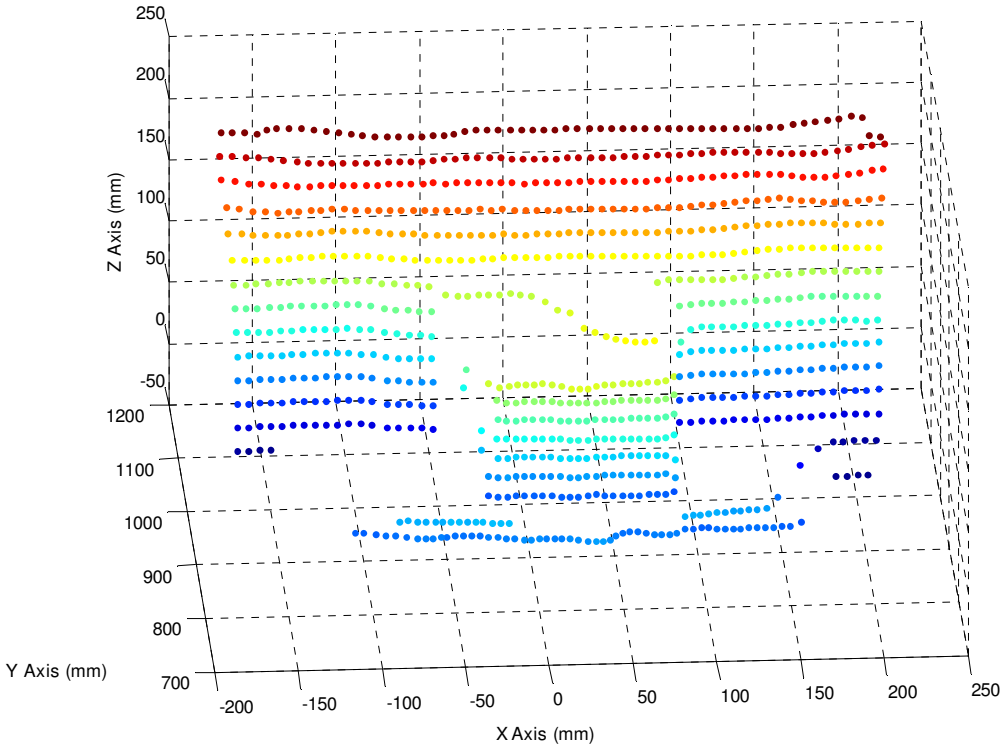

Figure 31 – LRS measurements with World Reference in Cartesian co-ordinates 3D Point Cloud

6.5.4 Discussion: 1st Test Rig

The results in Figure 30 and Figure 31 have allowed us to evaluate the 1st test rig in order to collect a series of 2D distance data and then create a 3D point cloud with the gathered data. The distance measurements gathered by the URG-04LX have allowed us to create a 3D surface mesh in Figure 30 from the point cloud created by the URG-04LX mounted on the 1st test rig. The 3D mesh provides a suitable visual representation which allows the user to visualise the target and surrounding area in 3D. A drawback with using the 3D mesh over the point cloud is that the mesh tries to connect each 3D point to another part of the mesh to create a single mesh to cover all of the point cloud. This can cause ambiguity within the image, for example the target used in this experiment was a rectangular box with uniform dimensions. The 3D mesh has connected the points from the front face of the box to the "wall" behind the target, and by doing so has made the 3D mesh look like the target is wider and taller than the target actually was. The 3D mesh in a similar way can hide points that are below the overlaid mesh hiding information that could be useful in evaluating a targets structural suitability while performing an indoor building inspection. The 3D point cloud in Figure 31does not use a 3D mesh in order to visualise the 3D data, but instead plots the individual distance points in 3D space point cloud. This visualisation has enabled us to evaluate individual points on the point cloud which may be of interest to an indoor building inspection. This type of 3D point cloud visualisation can be unappealing as without any visual cues the user may not clearly understand what they are looking at.

The measurements gathered from this experiment show that the measured length and height of the target was measured to within 0.2% and 0.3% of its actual value respectively. These values are within the ±10mm from the specification of the URG-04LX. The measurements of the depth of the target calculate the targets depth by subtracting the range measurements from the "wall" to the front face of the target. The measurements gathered showed that the "wall" was measured as being between 1085mm and 1127mm, and gives a difference of 42mm and would explain why the depth value calculated was larger than the actual target depth distance.

6.5.5 Conclusion: 1st Test Rig

Both 3D mesh and point clouds provide useful distance and visual information about the target we a observing and so both will be used to aid visual understanding and data collection of the targets in future experiments. It can also be seen that the 1st test rig can collect a series of 2D distance data

and then create a 3D point cloud with the gathered data. It was seen that the LRS can scan an area determined by size of the spot projected by the LRS onto the target. This limits the LRS to accurately describe targets bigger than the size of the projected laser spot. Based on the results shown the first test rig met the requirements in subsection 6.5.1. The next stage was to design a test rig which can collect 3D point data using a 2D range scanner. To simulate the movement of a UAV while performing scans was also required. This led to a second test rig being designed to incorporate these requirements.

6.6 References

[1] H. Kawata, A. Ohya, S. Yuta, W. Santosh, and T. Mori, “Development of ultra-small lightweight optical range sensor system,” in *Intelligent Robots and Systems, 2005. (IROS 2005). 2005 IEEE/RSJ International Conference on*, 2005, pp. 1078–1083 ST – Development of ultra–small lightwe.

[2] C. Ye and J. Borenstein, “Characterization of a 2-D Laser Scanner for Mobile Robot Obstacle Negotiation,” *2002 IEEE International Conference on Robotics and Automation*, vol. 3. Washington, pp. 2512–2518, 2002.

Chapter 7 2nd Test Rig Design

7.1 Introduction

This chapter describes the development of the 2nd test rig to simulate a UAV performing indoor building inspections whilst allowing the sensor suite to gather multiple 2D range scans from different positions and orientations. The mechanical and electronic design of the second test rig is discussed. The second test rig is then tested to evaluate if it can simulate a UAV performing an indoor building inspection. This chapter describes original contributions made by the author.

7.2 Overview

To test if the sensor suite could be deployed on a UAV to perform an indoor building inspection a 2nd test rig was constructed to simulate the UAV's position as if it were conducting an indoor building inspection. A simulated UAV was then mounted to the test rig carrying the sensor suite. A real UAV has six degrees of freedom (roll, pitch, yaw, X, Y, Z). The sensors were mounted onto the sensor suite which was mounted on the simulated UAV. Both laser range scanner and camera were mounted on the same pivot point on the pitch axis. The sensor suite uses the pitch and yaw axes to allow the laser range scanner and camera to scan the target area without the need to move the entire UAV. This extends the amount of time the UAV stays in the air which would increase the amount of data that the UAV can gather before needing to land and have its batteries changed.

7.2.1 2nd Test Rig

The test rig used in this project is a custom built optical rail which provides linear adjustments of the spacing between the simulated UAV and the target. The simplified CAD design for the test rig can be seen in Figure 32 and the built test rig can be seen in Figure 33.

At one end the optical rail pivots directly beneath the target, while the other end of the optical rail is mounted on a moveable support. The optical rail allows the simulated UAV to be positioned accurately a specific distance away from the target, and as it is mounted on a moveable support with a fixed pivot under the target the simulated UAV can be positioned to gather data from

the target at any required incident angle in a 180° arc. Mounted on the optical rail is the simulated UAV, this part of the test rig simulates the UAV that the sensor suite is to be mounted to. The simulated UAV can be adjusted to varying distances on the optical rail from the target up to the limit of the optical rail, while the height of the simulated UAV can also be controlled via the use of a scissor lift attached to the base of the simulated UAV. The optical rail and the simulated UAV allow the simulation of the positions that the simulated UAV can achieve while undertaking an inspection. The sensor suite is mounted rigidly to the simulated UAV directly above its centre, and has dedicated pitch and yaw control. Using the pitch adjustment the sensor suite can pitch through a large arc, allowing data to be gathered from multiple pitch angles while not requiring the simulated UAV to reposition itself. The yaw control also allows for the sensor suite to yaw through a large arc allowing data to be gathered from multiple yaw angles while also not requiring the simulated UAV to reposition itself.

The X, Y axes of the simulated UAV are originally described in terms of polar coordinates (r, θ) and are then converted to a set of Cartesian coordinates relative to the world axis as discussed in chapter 5. The test rig has manual control of the r, θ of the simulated UAV in order to simulate the movement of the simulated UAV. The pitch of the sensor suite uses custom built software and hardware to control the yaw of the sensor suite and also to monitor, gather and process the data from the laser range scanner and camera.

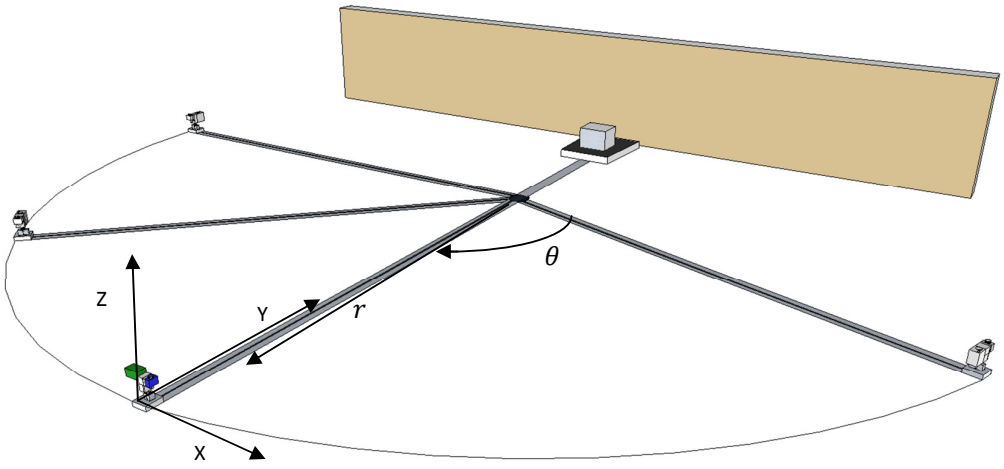

Figure 32 – CAD of Simulated UAV at Different Scanning Positions

Figure 33 – 2nd Test Rig

Figure 34 – 2nd Test rig pivoting around target

7.3 Mechanical Design

The test rig was designed by the author and the in house mechanical workshop carried out the construction.

7.3.1 Optical Rail

To simulate the *r* positioning of the simulated UAV an optical rail was the simplest design to use. The optical rail allowed for the simulated UAV to slide along the rail and with the use of a ruler positioned along its length, the *r* positioning of the simulated UAV could be set accurately to within 1mm. The optical rail is made from aluminium profile and is 2m in length. Figure 33 shows the optical rail described above.

7.3.2 *r* and θ Positioning

The θ positioning requires that the optical rail be pivoted under the target and then rotated around the target as shown in Figure 34. This was achieved by mounting each leg of the table with swivel castors which allowed the table to be moved in any direction freely. The optical rail was secured to the pivot point and also the moveable table which allowed 180° rotation around the target. The reason for using such a wide rotational arc around the target was to simulate the type of scanning a real UAV might perform. A real UAV could travel parallel to the wall while scanning a target to collect as much data as possible. This would be done from as many different angles as possible while maintaining an efficient flight path. The position of the simulated UAV used in the test rig is described in a polar coordinate system (*r*, θ), care is required when converting these positions into a world Cartesian coordinate system in order to accurately describe the simulated UAV's position.

7.3.3 Simulated UAV

The simulated UAV as mentioned above is adjusted to various positions along the optical rail. The simulated UAV is an aluminium plate mounted onto the optical rail by a steel nut set into one of the aluminium profile's grooves Figure 35. The simulated UAV can be positioned along the optical rail and the nut tightened to allow the simulated UAV to remain in a fixed position and then slackened to allow the simulated UAV to be reposition. The simulated UAV can repositioning itself vertically using a scissor lift attached to its base plate which allows for manual height (Z-axis) adjustments Figure 36.

7.3.4 Sensor Suite

The sensor suite's position is simulated by mounting it directly to the simulated UAV Figure 37, Figure 36. A stepper motor attached to the sensor suite which controls the yaw of the sensors. The stepper motor used is a MY701 hybrid model with a step angle of 1.8°.This model was chosen as it provided a small step angle, has a high torque output and as it is a bipolar motor it can be used to rotate bidirectionally by setting an appropriate current controlled by a microcontroller. Using a PIC32 microcontroller the stepper motor is controlled and is programmed to rotate automatically allowing the sensor suite to rotate in a large arc which allows it to gather data from a large range of yaw angles without the simulated UAV having to reposition as described in chapter 4 .

Pitch control of the sensor suite is achieved by using a custom built goniometer. The sensors are mounted around a single pivot point on a square piece of Perspex which is aligned with a protractor to measure the pitching angle of the sensor suite to an accuracy of 1°. As the pitch angle changes, both of the sensors pitch at the same rate, which allows for the creation of multiple data representations of the target, such as camera images or point clouds. As the pitch angle is known from the goniometer, the point clouds gathered in two dimensions can be used to create a 3D point cloud.

Figure 35 – Second test rig with Sensor suite mounted on simulated UAV

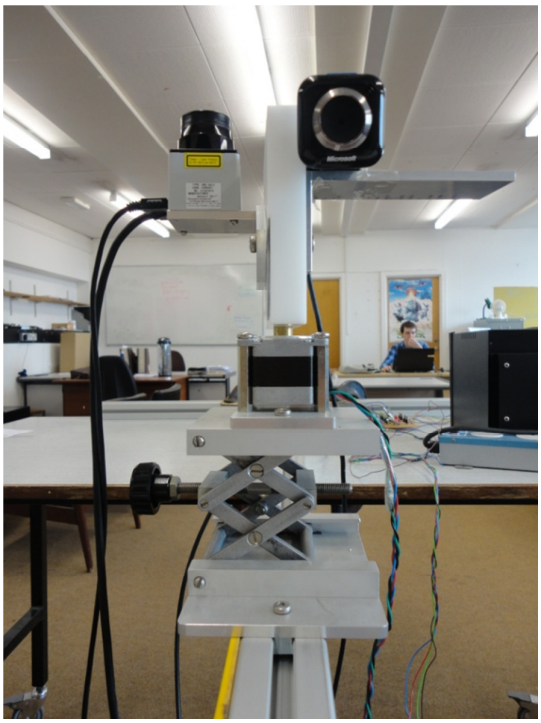

Figure 36 – Second test rig with Sensor suite mounted on simulated UAV

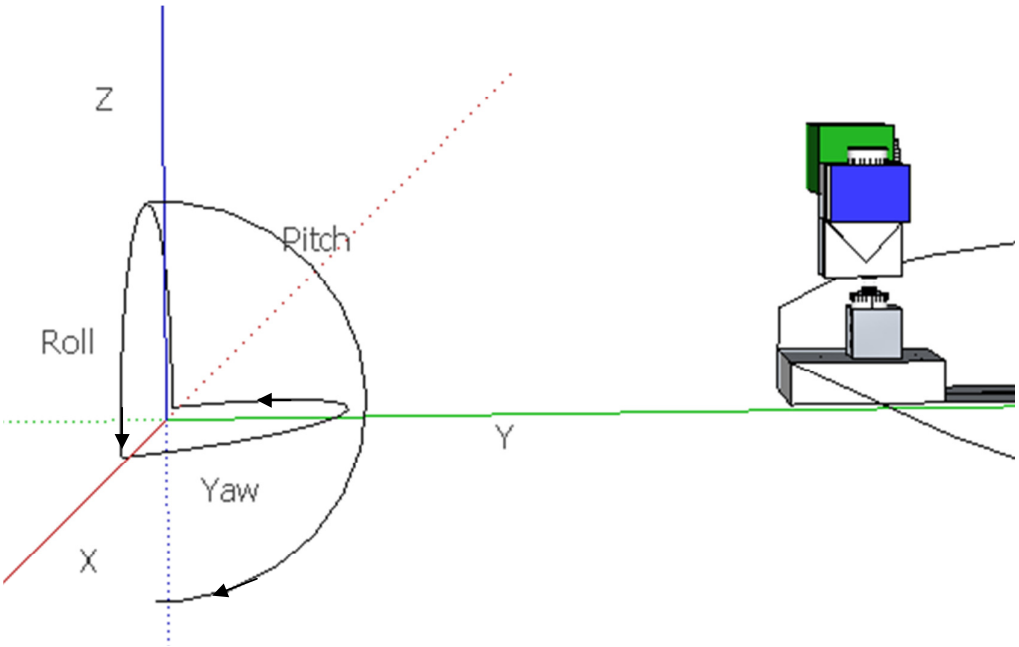

Figure 37 – Sensor Suite 6 Axis Layout

7.3.5 Mounted Sensor Suite Specifications

The sensor suite that the URG-04LX and VX-500 are mounted on can be seen in Figure 36. The sensor suite can pitch 180° to allow the collection of 2D range data and images at varying pitch angles. The URG-04LX is mounted to the right of the sensor suite and the VX-500 to the left. The VX-500 has been mounted further forward as the white Perspex mount which holds the sensor suite blocked the VX-500 FOV.

7.4 2nd Test Rig Testing

To test the suitability of the 2nd test rig to simulate the positioning of the simulated UAV whilst allowing the sensor suite to gather 2D range data and visual images a suitable test target was chosen. The values of the gathered data were then compared measurements of the target and the test rig.

7.4.1 2nd Test Rig Specifications

- Allow for mounting of sensor suite
- Ability to pitch and yaw the sensor suite based upon a gimbal design and stepper motor
- Gather visual images and 2D LRS data
- Create a 3D point cloud with the multiple 2D LRS data
- Simulate the UAV moving around the target

7.4.2 2nd Test Rig Experiment 1

The experiment is designed to observe and evaluate the 2nd test rig in order to test the ability of the 2nd test rig to collect a series of 2D distance data and then create a 3D point cloud with the gathered data. The target used in this experiment was a wooden block with dimensions 88*75*125mm, (L*D*H). The test rig was then aligned to measure the distance from the device with a θ of 0°. The URG-04LX was directly in front of the target and at the starting point the pitch angle was 0°, the URG-04LX was parallel to the ground. The URG-04LX was then manually rotated in pitch about a constant point using a goniometer from 0° to 14°. At each individual pitch angle the URG-04LX collected distance measurements from the target with a field of view from the front most point of the scanner. This FOV used in this experiment was 21° from scan points 359-417 within the URG-

04LX, both the FOV and pitch angle were used to provide enough measurement points to cover the width and height of the target and also a percentage of the background wall to compare the target against. The UAV is then moved to another known position in order simulate the UAV repositioning the sensor suite. This allows the simulated UAV to gather distance data from different angles in the same method the UAV would perform if this were a real inspection. The 2nd test rig allows the simulated UAV to be positioned around a target from -170° to +170° as seen in Figure 38. Data is gathered from 15 different positions at 10° intervals, while maintaining the same distance to the target from the UAV. The experimental set up can be seen in Figure 33 and Figure 34.

The distance from the front of the target to the front of the URG-03LX is 980mm , with a wall at 1500mm behind the target. The URG-04LX was then programmed to collect 1000 range data points at each pitch angle so that the average value could be used. The experiment was conducted in a room illuminated with fluorescent lamps. Before the test, the URG-04LX was turned on for a minimum of 140 minutes to allow the device a suitable warm up period.

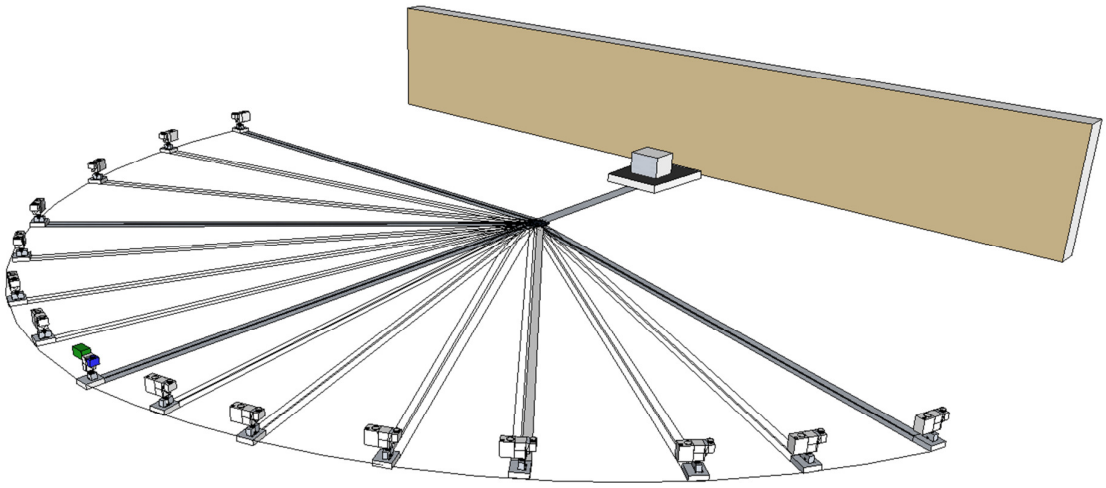

Figure 38 – -170° to 170° Scan Positions

7.4.3 Results 2nd Test Rig Experiment 1

The experiment was performed as described above, the data was processed and is presented in Figure 39. Figure 39 shows the processed data collected by the URG-04LX mounted on the 2nd test rig. The distance measurements, pitch angle, scan point data, and position of the simulated UAV have been used to create a Cartesian coordinate system which shows the measured distance data relative to a world axis defined by the user. The colours used in Figure 39 refer to the height of the

measured points. The front face of the box can be clearly seen around 970-980mm on the Y axis and the top of the box can be seen at 139mm on the Z axis stretching back to the "wall". Below the box faces there is a green area which represents the parallel mount that the target was placed upon, the ground surface ran below the target.

The values measured from the faces of the target in Figure 39 have a width of 86mm, height of 122mm taken from the front face. The depth of the target was measured from the front face of the target to where the LRS stopped gathering target data and jumped to 1500mm which indicated it was gathering wall data instead. The depth of the target was measured as 76mm.The measurements gathered showed that the "wall" was measured as being between 1509mm and 1526mm, and gives us a difference of 17mm which is larger than the actual "wall" distance of 1000mm by 9mm-26mm. Compared to the actual values of the target (88*75*125mm, (L*D*H)) the height, depth and length measured values are within -2mm to +1mm of the actual target values.

7.4.4 Discussion 2nd Test Rig Experiment 1

The measurements gathered from this experiment show that the measured length and height and depth of the target were measured to within 2% of their actual values. The use of the 3D mesh was not a useful visual representation to the end user. This is due to the anomalous points that have been gathered by the LRS. The anomalous data points cannot be clearly distinguished from the actual data points gathered from the target. If the anomalous data points can be removed then the mesh would be a useful representation.

7.4.5 Conclusion: 2ndTest Rig Experiment 1

The 3D point cloud provided distance and visual information about the target being observed to aid visual understanding and data collection of the targets. It can also be seen that the 2nd test rig can simulate the collection of inspection data in order to create a 3D point cloud with the gathered data. From the experiment performed on the second test rig it can be seen that the 2nd test rig simulate a UAV moving around a target, allows for a suitable mounting of the sensor suite, has the ability to provide multiple pitch and yaw angles for the sensor suite, the sensor suite can gather visual and 2D LIDAR data to create 3D point clouds. The URG-04LX gathered range values and displayed them in a useful way to the user using point clouds. The test rig is performing scans using the LRS at all of the

pitch angles (0° – 14°)at a specific UAV position angle(θ) and then repeating the procedure at a different UAV position angle. If there was an error in the positioning of the pitch angle of the sensor suite the LRS will give different distance data depending on its pitch angle. To see if this has an effect on the data gathered by the sensor suite another experiment is performed.

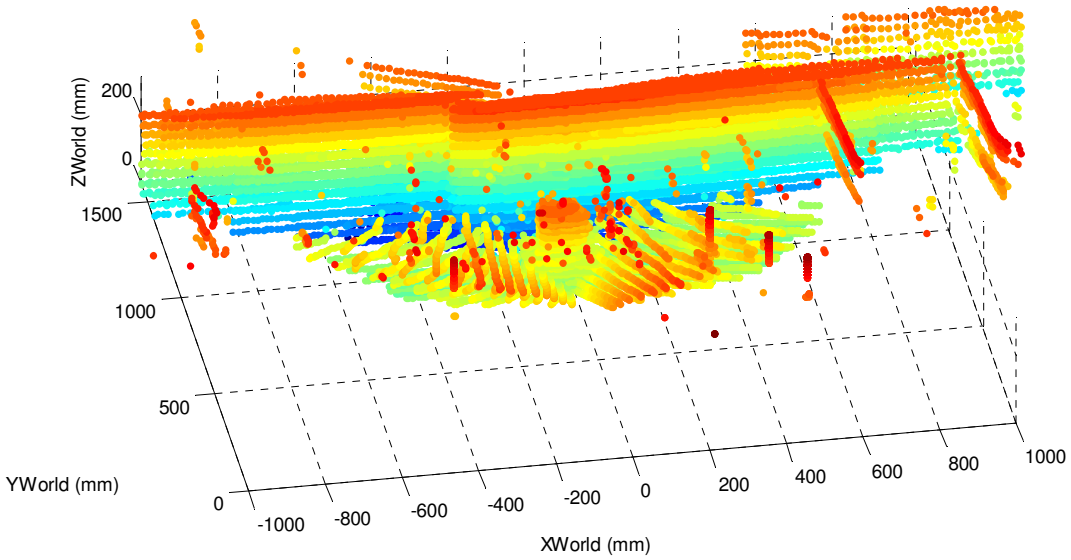

Figure 39 – Point Cloud of Wooden Block in Cartesian World Coordinates from multiple angles (θ)

7.4.6 2nd Test rig Experiment 2

This experiment investigates if performing all of the pitch scans at a specific UAV position angle has an effect on the data collected by the sensor suite. The UAV will be moved to all of the position angles around the target sequentially with the same pitch angle. The sensor suite will gather the data from the target. After all of the UAV position angles have been used to scan the target the pitch angle will be changed and the process repeated until all of the range of pitch angles have been scanned from.

7.4.7 Results: 2nd Test rig Experiment 2

The experiment was performed as described above, the data was processed and is presented in Figure 40. The use of the 3D mesh was not a useful visual representation to the end user and so was

not included. This is due to the anomalous points that have been gathered by the LRS. Figure 40 shows the processed data collected by the URG-04LX mounted on the 2nd test rig. The distance measurements, pitch angle, scan point and data about the goniometer have been used to create a Cartesian coordinate system which shows the measured distance data relative to a world axis defined by the user. The colours used in Figure 40 refer to the height of the measured points. The front face of the box can be clearly seen around 947-1000mm on the Y axis and the top of the box can be seen at 171mm on the Z axis. Below the box faces there is a green area which represents the parallel mount that the target was placed upon.

The values measured from the faces of the target in Figure 40 have a length of 89mm and a height of 107mm taken from the front face. The depth of the target was measured from the front face of the target to where the LRS stopped gathering target data and jumped to 1500mm which indicated it was gathering wall data instead. The depth of the target was measured as 83mm.The measurements gathered showed that the "wall" was measured as being between 1441mm and 1529mm, and gives us a difference of 88mm. Compared to the actual values of the target (88*75*125mm, (L*D*H)) the height, depth and length measured values are within -18mm to +8mm of the actual target values. It can also be seen that the point cloud of the target does not look exactly like the target being scanned. One side of the point cloud representing the target is curved, whereas the actual target is square.

7.4.8 Discussion 2nd Test rig Experiment2

The measurements gathered from this experiment show that the measured length and height and depth of the target were measured to within 1%, 16 % and 9% of its actual value respectively. These values are not within the ±10mm specified by the specification of the URG-04LX. When compared to the #1 method for collecting distance data using the 2nd test rig this #2 method provides data with greater errors in distance measuring. It is the opinion of the author that the problem seen is due to the way the test rig is designed as it could allow small movements of the UAV in the specific UAV position angle(θ). As the UAV was moving from each UAV angle a total of 63 times this could have affected the accuracy of the reported position of the UAV and therefore affected the results.

7.4.9 Conclusion: 2nd Test rig Experiment 2

The 3D point cloud provided distance and visual information about the target being observed to aid visual understanding and data collection of the targets. The two different ways of gathering the data showed that results gathered using the 2nd test rig should be gathered in the #1 method rather than the #2 method due to the inaccuracies observed when moving the test rig into different positions which have an effect on the accuracy of the data.

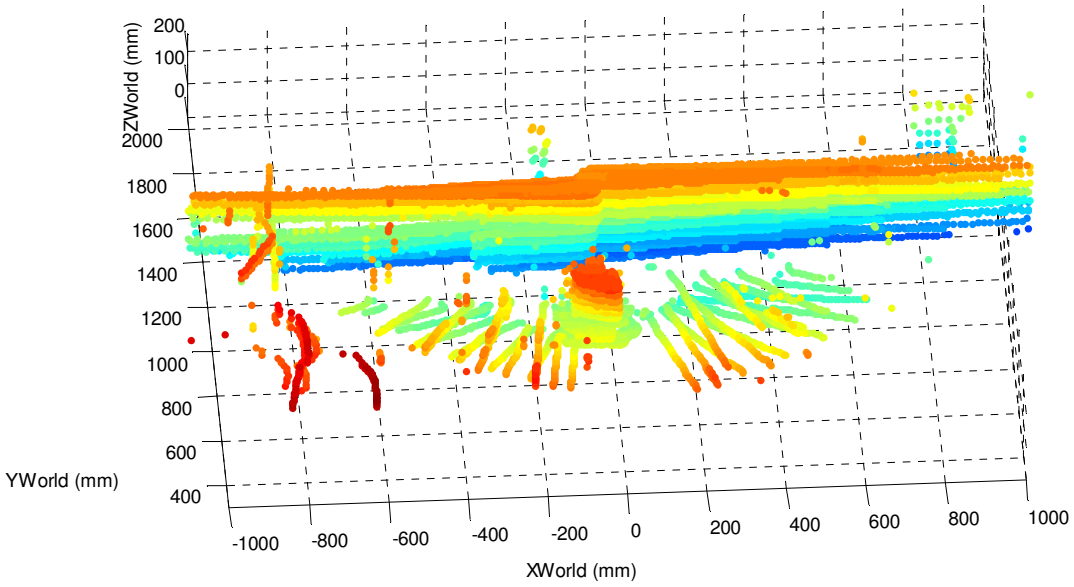

Figure 40 – Point Cloud of Wooden Block in Cartesian World Coordinates from multiple angles (θ)

7.5 Yaw Experiment

This experiment is designed to observe and evaluate the 2nd test rig in order to test the ability of the stepper motor to provide yaw control of the sensor suite. The LRF was turned on and allowed to warm up. Four scans were taken of a wooden target, two scans were taken at 0° and two at -0.9° relative to the world axis discussed in Chapter 5.

7.5.1 Results

The experiment was performed as described above, the data was processed and is presented in Figure 41. The orange and red scans were taken at -1.8° and the brown and dark brown were taken at 0°. The orange and the red scans were compared to the brown scans to see if the stepper motor

had moved accurately -1.8°. The results showed that the distance between the red and orange scans compared to the brown scans was 31.41mm further away. When this was compared to the actual value calculated it was seen that the difference between the theoretical and actual value was only 0.299mm.

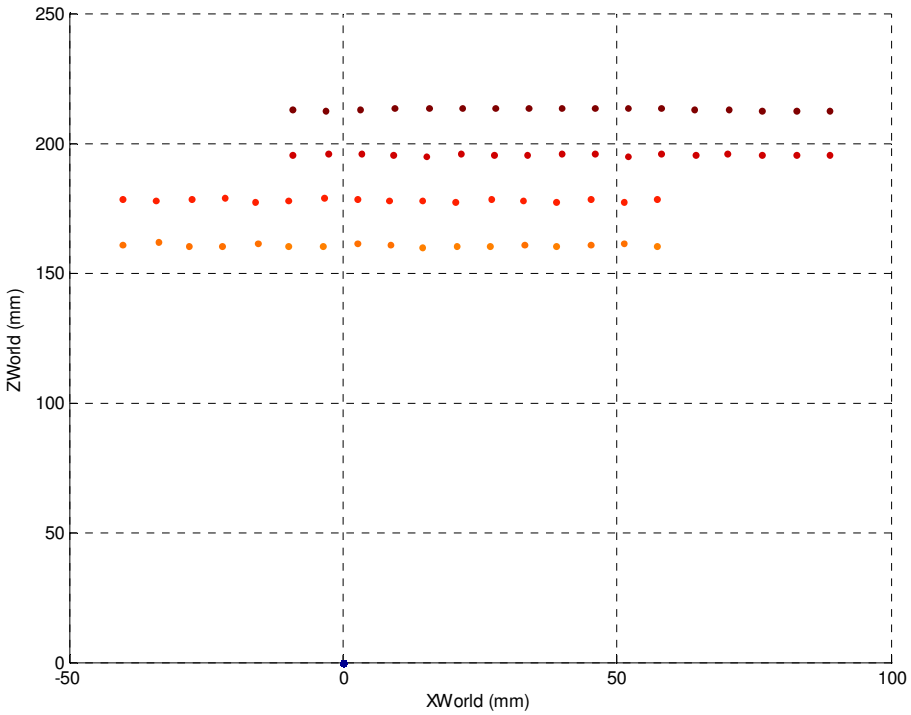

Figure 41 – Yaw Experiment Results

7.5.2 Discussion

The results from the yaw experiment show that the stepper motor can provide yaw control to within 1.8° and give a value that is 0.299mm away from the actual calculated value.

7.5.3 Conclusions

The yaw experiment showed that the stepper motor used in the test rig can provide repeatable control of the sensor suite. The stepper motor has shown that it cannot meet the exact specifications of each step being 1.8°. As the step error is 0.299mm which is small when compared to the compared to the possible errors seen with the URG-04LX it has been decided that the stepper motor can provide sufficient control of the sensor suite for use in this research.

7.6 Conclusion

This chapter has described 2nd test rig from design, construction through to testing. This was performed in order to create a suitable test rig that can simulate the movement of UAV and also the method in which the sensor suite can be used to gather multiple 2D range scans and visual images from target areas while performing indoor building inspection. The test rig allowed for measurements of r, θ *which* describe the simulated UAV's position and allowed for the calculation of the coordinates in a Cartesian coordinate system. The test rig also allowed for measurements of α, β and γ which described the sensor suites orientation in a Cartesian coordinate system. The simulated UAV could yaw at nearly 1.8° increments and adjust the sensor suite's pitch angle in degrees. This allowed the sensor suite to gather multiple 2D data scans quickly. The second test rig was tested to evaluate its ability to simulate a UAV manoeuvring whilst gathering data for an indoor building inspection.

Chapter 8 Fusion of Range and Image Data

8.1 Introduction

This chapter describes how the gathered visual and range gathered by the sensor suite was used to allow the user access to both the physical dimensions and the visual images gathered by the UAV on one consistent and useful representation. The first section discusses the how data fusion can be performed in this research. The second section discusses how to implement the data fusion using Matlab. The third section shows experimental data gathered using Matlab to evaluate mathematical transforms used to create data fusion. A program to implement the transforms automatically (value.m) and a program to calculate simple measurements from the target are also developed (ruler.m). This chapter describes original contributions made by the author.

8.2 Implementing Data Fusion with Matlab

The next sub-section shows how data fusion was implemented on the multi-modal sensor suite's data using Matlab.

Initially the 3D point cloud data was analysed from the LRS using the PtoC.m program to spot any obvious erroneous points which allowed them to be removed "manually" by editing the text file in which they were stored.

Data registration was then used to align the two data sets (3D point cloud and visual image) of the same scene. The first step was to create control points within both data sets. These control points are a subset of points whose position and location in the two data sets is known or can be selected interactively by the user. Once a sufficient number of control points have been chosen by the user the image processing toolbox in Matlab can use the function cp2tform which infers spatial transformation from control point pairs to apply a specific spatial transformation to the control points on both data sets. Combining the images and performing quantitative analysis requires that geometric deviations caused by the differences in the sensor angle, distance, sensor resolution and orientation are compensated. Data registration has been used before by S. Gernhardt et al.[1] and D. Klimentjew and J. Zhang [2]to register point clouds and visual images.

8.2.1 Cp2tform Using Control Point Registration

As mentioned above the cp2tform function in Matlab uses control points to infer spatial transforms.

The function cp2tform creates a geometric mapping based on the type of transformation selected. The mapping is dependent on control points, which are points visible in both data sets that describe the same feature. The control points are stored in a matrix which contains their coordinates. Once a sufficient number of control points are selected the geometric mapping is inferred to both data sets. The mapping is dependent on the position of control points selected, and the number of control points used.

An investigative experiment on data collected is performed to see how using different transformation types affect the physical dimensions displayed to the user.

8.2.2 Automation of Geometric Transform Creation and Simple Distance Programs

This subsection describes two custom programs written and developed by the author to automate the process of creating the geometric transform between the visual image and point cloud, and also to calculate simple distances between two points selected by the user.

8.2.3 ruler.m

This program automates the creation of the geometric transform between the visual image and point cloud data sets based on the control points inputted by the user. The program allows the user to select which data sets to use and open them to allow the control points in both data sets to be selected by clicking on the visual image and typing the point cloud values into the command console. The program then creates the geometric transform between the two data sets based on the control points and the type of transformation type required.

8.2.4 values.m

This program allows the user to select points on the visual image used in ruler.m to measure simple distances between two points selected by the user. Simple distances are defined as straight lines either horizontal or vertically between two points. The program allows the user to select the points they want to know the distance between and the program calculates the distance between them using the geometric transform calculated in ruler.m. The distance between the two points is then displayed to the user.

8.3 Fusion Data Experiments

The experiment is designed to observe and evaluate the fusion of two different sets of data into one multidimensional data set. Using the 2nd test rig to collect a series of 2D distance data using the LRS, a 3D point cloud with the gathered data and also the camera to gather 2D images from the target can be created. The target used in this experiment was a wooden block with dimensions 88*75*125mm, (L*D*H). The test rig was then aligned to measure the distance from the device with a θ of 0°. The URG-04LX was directly in front of the target and at the starting point the pitch angle was 0°, the URG-04LX was parallel to the ground. The URG-04LX was then rotated in pitch about a constant point using a goniometer from 5° to 20°. At each individual pitch angle the URG-04LX collected distance measurements from the target with a field of view (FOV) from the most front point of the scanner. This FOV used in this experiment was 52° from scan points 316-460 within the URG-04LX, both the FOV and pitch angle were used to provide enough measurement points to cover the width and height of the target and also a percentage of the background wall to compare the target against. The UAV is moved to another known position in order simulate the UAV repositioning the sensor suite. This will allow us to gather distance data from different angles in the same method the UAV would perform if this were a real inspection. The 2nd test rig allows us to position the UAV around the target at 10° intervals from -170° to +170°. For this experiment data was gathered from all of the 15 different positions, while maintaining the same distance to the target from the UAV.

The distance to the front face of the target was 980mm away from the front of the URG-04LX, with a wall at 1500mm behind the target. The URG-04LX was then programmed to collect 1000 range data points at each pitch angle so that the average value could be used. The experiment was conducted in a room illuminated with fluorescent lamps. Before the test, the URG-04LX was turned on for a minimum of 140 minutes to allow the device a suitable warm up period.

8.3.1 Results: Fusion Data

The results used in this experiment have been gathered using the Experimental Methods: 2nd Test Rig #1 with both visual images and point clouds being stored. Using the ruler.m and values.m program designed by the author the process of data fusion between the two has been performed. Using ruler.m and values.m the user is allowed to select the data sets they want to inspect. Once the appropriate data is selected by the user they can select individual images to view. Once an image of interest has been selected, the user can select control points from the image (Figure 42) and corresponding control points from the point cloud (Figure 43). Once this process has been completed the user can select points from the selected image of interest and gather data suitable for indoor building inspection using the multidimensional data. The types of data that can be accessed on one display using sensor fusion are:-

- Visual Image/Assessment
- 3D Physical Data from User Selected Points
- X Distance Target Data
- Y Distance Target Data
- Z Distance Target Data

The physical dimensions of the target in this experiment are known as they have been measured by the laser range scanner and also by hand, comparisons can be made between the point cloud data and fusion data against it. Using code developed for this research selected test points on the visual image have been selected to compare against the known physical value of the target in order to evaluate its effectiveness at representing accurate data to the user.

In these results Figure 42 is used to allow us to select suitable control points (CP)to be created between the visual image and the point cloud (Figure 43).

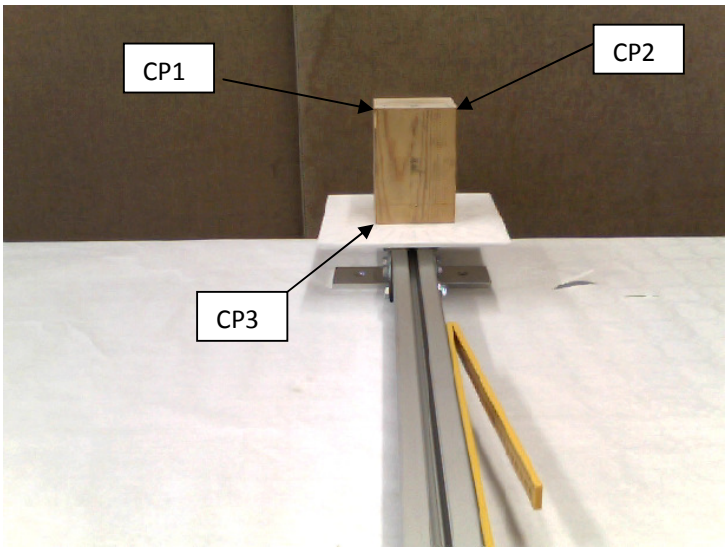

Figure 42 – Visual Image Showing Control Points

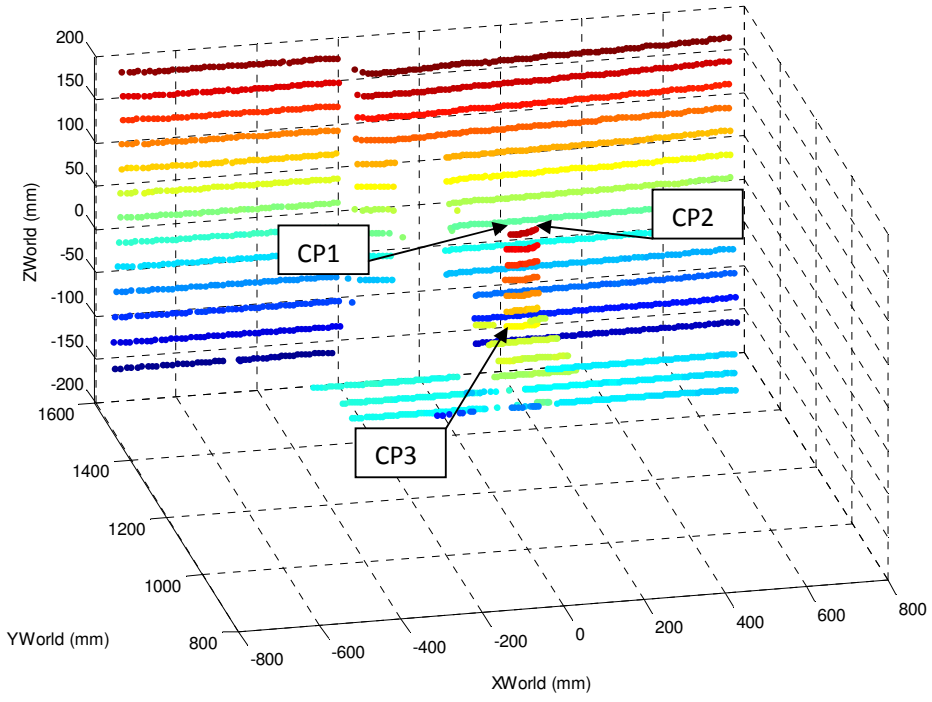

Figure 43 – Point Cloud Showing Control Points

After running the ruler.m and values.m program developed for this research and selecting suitable control points in the visual image and points cloud the user can then freely investigate the physical dimensions of the target by clicking on the corresponding point of interest on the visual image. This

will then return to the user the physical values of the target point they have selected. The user is also able to measure simple distances between two points on the visual image.

8.3.2 Control Points Results

The first tests performed on the results data have been to make sure that the custom programs returned physical dimensions that were accurate. As points CP1, CP2 and CP3 are well defined control points, the results gathered by the custom programs can then be compared to the control points to check their accuracy. The affine transform was used in this experiment.

Data Point Name	Measured Physical Position (mm)	Reading (mm)	Difference (mm)	% Error
CP1	X = -56.04	X =-56.05	0.01	0.018
	Y = 984.6	Y =984.34	0.26	0.03
	Z = 170	Z =166.90	3.1	1.82
CP2	X = 25.14	X =25.84	-0.7	2.71
	Y = 1006	Y =1006.8	-0.8	0.08
	Z = 166.7	Z =164.77	1.93	1.10
CP3	X = -46.88	X =-46.98	0.1	0.21
	Y = 987.1	Y =987.07	0.03	0.06
	Z = 45.18	Z =44.81	0.37	0.82

Table 11 – Comparison between known and calcualted control points

8.3.3 Discussion

Table 11 shows the results gathered by selecting pixels on the visual image and using the custom programs to calculate the position of the pixel on the point cloud. The table is separated into four columns, the data point name, measured physical position, reading, difference and percentage error. The data point name show the name of the point at which the results were sampled from. In this case it was over three control points. The measured physical position shows the measured physical position of the data point on the world axis by the laser range scanner. The reading column shows the calculated position of the data point using the custom programs. The difference between the

measured physical position and reading is shown in the difference column. The percentage error between the reading and measured physical position is shown in the final column.

The results show that the largest percentage error was observed at 2.71% on the CP2's X position when compared to the actual physical value. All of the values measured in Table 11 have low percentage error values and the largest error is only 3.1mm.

8.3.4 Non-Control Points

The second test has been performed on selected points in the visual image that have been measured and whose physical values are known, but are not control points. This will then allow us to compare well defined points of interest to the defined control point's results.

The control points used in this experiment were the same as those in Figure 42 and Table 11.

Instead of using these control points to gather measurements from the target non-control points have been used. Non-control points are specific points on the target that can be identified by the user and also be measured by so that any data gathered can be compared against these known quantities. The non-control points can be seen in Figure 44. The affine transform was used in this experiment.

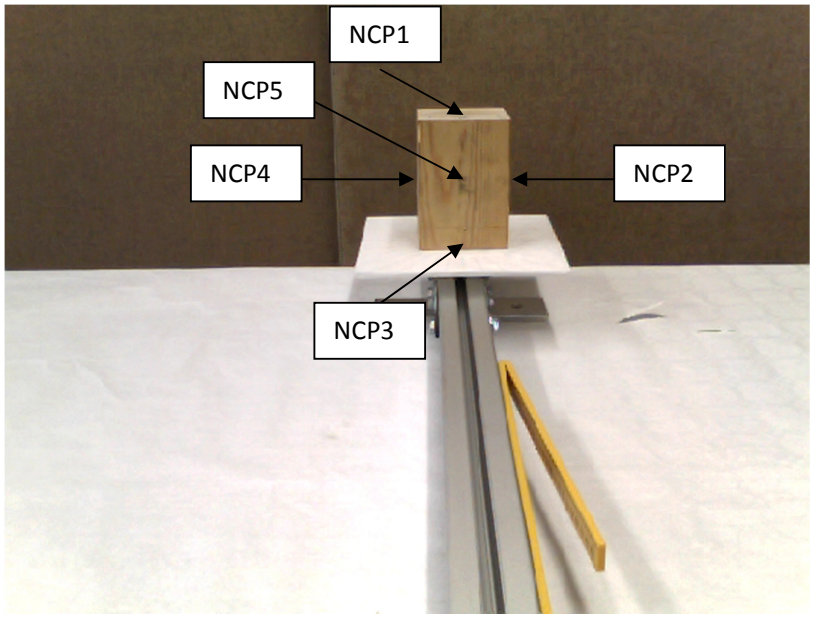

Figure 44 – Location of Non-control points

Data Point Name	Measured Physical Position (mm)	Reading (mm)	Difference (mm)	% Error
NCP1	X = -14.95	X = -15.45	-0.5	3.34
	Y = 990.21	Y =995.30	-5.09	0.52
	Z = 170	Z = 168.30	1.7	1
NCP2	X = 25.14	X = 29.16	-4.02	15.99
	Y = 1006.8	Y = 1007.1	-0.3	0.03
	Z = 107.59	Z = 104	3.59	-3.34
NCP3	X = -14.95	X = -7.42	-7.53	-50.37
	Y = 987.1	Y = 997.50	-10.4	1.05
	Z = 45.18	Z = 43.58	1.6	-3.54
NCP4	X = -56.04	X = -53.15	-2.89	-5.16
	Y = 990.21	Y = 985.40	4.81	-0.46
	Z = 107.59	Z = 107.66	-0.07	0.07
NCP5	X = -14.95	X = -11.43	-3.52	-23.55
	Y = 982.6	Y = 996.40	-13.8	1.40
	Z = 107.59	Z = 105.96	1.63	-1.52

Table 12 – Comparison between known and calcualted non-control points

8.3.5 Discussion

Table 12 shows the results gathered by selecting Non-control point pixels on the visual image and using the custom program to calculate the position of the pixel on the point cloud. The results show that the largest percentage error was observed at -50.37% on the NCP3's X position when compared to the actual physical value. The majority of the results had a percentage error value below 5%, with only three values having larger values ranging from -50.37% to 15.99%. The largest absolute error observed was -13.8mm on NCP5.

8.3.6 Fusion Data Discussion

The control points results show that the maximum percentage error observed was 2.71% with most of the errors being below 1%. When this is compared to non-control point's results it can be seen that the highest percentage error was -50.37%.

The difference in percentage error values between the two sets of data is due to the distance the sample is away from a control point. It can be seen that the closer the sample point is to the target the smaller the percentage error and absolute error.

Although the percentage error is larger in the non-control points, the size of the absolute error is at maximum -13.8mm. This can also be compared to the accuracy error in the LRS which is of similar magnitude.

Both the control points and non-control points were used to calculate the dimensions of the target. It can be seen that both control and non-control points gave similar values for both the length and height of the target.

8.3.7 Conclusion

The results from the fusion data tests have shown that the use of control points can be used to measure the physical dimensions of a target to within an accuracy of 14mm. When this is compared to the size of the target which is (L*D*H)(88*75*125mm) it can be seen that the accuracy can give possible readings of (L*D*H)(16%*18%*11%) of the targets actual values when scanned at a distance of 1m. The size of this error is small and is of similar size to that of the LRS used to gather the data at a similar range and target size.

It has been shown that the use of control points influences this accuracy. The closer the sample point is to the control point the smaller the error in calculated physical dimensions compared to the known dimensions.

It has also been shown that using data fusion allowed the user to view visual images and access user specified point to measure physical dimensions from the target in the form of X,Y and Z world coordinates.

From this it has been decided that this method for data fusion is a viable method to use for the project.

8.3.8 Fusion Data Physical Dimensions Measurements

For this experiment the data gathered from previous experiments was used as the values of the wooden target were known and the control points were already well defined (Figure 45).

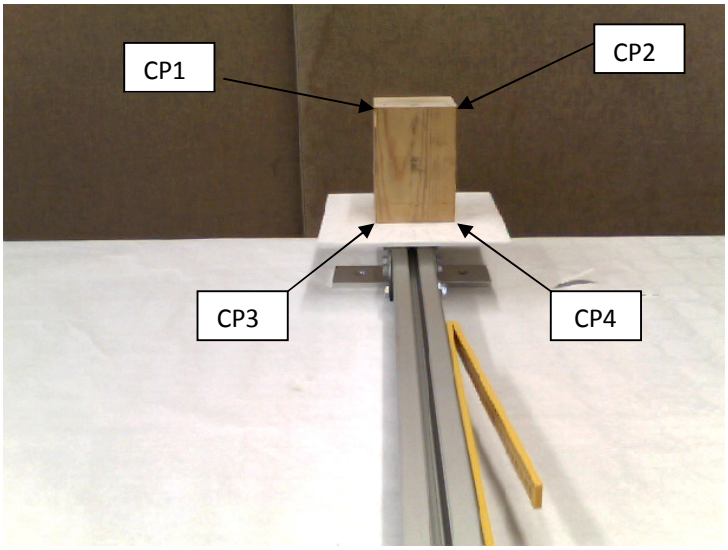

Figure 45 – Control Points

As the target's physical dimensions are known a comparison of the actual data gathered from the sensor suite can be compared to data produced by the value.m program. The experiment will sample areas on the wooden target.

8.3.9 Results

Sample Between	Known Absolute Values (mm)	Measured Values (mm)	Difference Between Known and Measured(mm)
CP1 – CP2	X =81.18	X = 78.362	2.818
	Y = 15.4	Y = 12.943	2.457
	Z = 3.3	Z = 1.053	2.247
CP1 – CP3	X = 9.16	X = 2.078	7.082
	Y = 2.5	Y = 6.903	-4.403
	Z = 123.43	Z = 123.669	-0.239
CP3 – CP4	X = 68.02	X = 70.297	-2.277
	Y = 2.9	Y = 12.837	-9.937
	Z = 1.39	Z = 0.162	1.228
CP4 - CP2	X = 4.0	X = 1.013	2.987
	Y = 2.9	Y = 7.009	-4.109
	Z = 120.13	Z = 122.454	-2.324
Middle to Right Edge	X = 40.59	X = 38.659	1.931
	Y = 23.4	Y = 20.385	3.015
	Z =1.2	Z = 0.519	0.681
Middle to Left Edge	X = 40.59	X = 37.614	2.976
	Y = 2.0	Y = 6.213	-4.213
	Z = 0.503	Z = 0.505	-0.002
Middle to Top Edge	X = 1.2	X = 2.053	-0.853
	Y = 2	Y = 3.178	-1.178
	Z =60.065	Z =60.047	0.018

Middle to Bottom Edge	X = 2.12	X = 2.053	0.067
	Y = 8.21	Y = 3.179	5.031
	Z = 61.712	Z = 60.047	1.665

Table 13 – Comparison of Physical Values Gathered Against Physical Values Calculated by value.m

The results from CP1 – CP2 sample showed a difference between the known absolute and measured values was at 2.818mm at its maximum with the lowest being 2.247mm. The results for the CP1 – CP2 sample are also of similar size in magnitude. This lower difference value could be due to the fact that the samples are being taken from control points that have been defined in the creation of the transform.

The results from CP1 – CP3 sample showed a difference between the known absolute and measured values was at 7.082mm at its maximum with the lowest being -4.403mm. The X value under measured, whereas the Y value over measured the physical dimensions of the target. The Z value also under measured the target but was smaller in size when compared to the X and Y values of the same sample.

The results from CP3 – CP4 sample showed a difference between the known absolute and measured values was at -9.937mm at its maximum with the lowest being 1.228mm. Both the X and Y value over measured the physical dimensions of the target. The Z value under measured the target..

The results from CP4 - CP2 sample showed a difference between the known absolute and measured values was at -4.109mm at its maximum with the lowest being 2.987mm. Both the Y and Z value over measured the physical dimensions of the target by 2 – 4mm. The X value under measured the target by 2.987mm.

The results from Middle to Right Edge sample showed a difference between the known absolute and measured values was at 3.015mm at its maximum with the lowest being 0.681mm. The entire sample underestimated the measured physical dimensions of the target. The X and Z values showed the smallest underestimation whereas the Y value showed the largest.

The results from Middle to Left Edge sample showed a difference between the known absolute and measured values was at -4.213mm at its maximum with the lowest being 2.987mm. Both the Y and Z value over measured the physical dimensions of the target by up to 4mm. The X value under measured the target by 2.976mm.

The results from Middle to Top Edge sample showed a difference between the known absolute and measured values was at -1.178mm at its maximum with the lowest being 0.018mm. Both the X and Y value over measured the physical dimensions of the target by around 1mm. The Z value under measured the target by 0.018mm.

The results from Middle to Bottom Edge sample showed a difference between the known absolute and measured values was at 5.031mm at its maximum with the lowest being 0.067mm. The entire sample underestimated the measured the physical dimensions of the target. The X and Z values showed the smallest underestimation whereas the Y value showed the largest.

8.3.10 Discussion

From the results it can be seen that that largest difference between the known and measured values in the experiment was on CP3 – CP4 which over estimated the value by -9.937mm. The largest difference observed in the X values was at the CP1 – CP3 sample at 7.082mm, in the Y values the largest observed difference was observed in the CP3 – CP4 sample at -9.937mm.The largest difference observed in the Z values was seen in CP4 – CP2 at -2.324mm.

8.3.11 Conclusion

The results from this experiment showed that all of the differences between known and measured points were within ±10mm accuracy value. As this is the tolerance of the LRS the values.m program can be considered to work correctly and provide accurate data on simple distances.

8.4 Data Fusion Conclusions

This chapter has described a method for data fusion of two different set of data using Matlab. The affine and linear conformal transforms were selected due to their small number of required control points. The number of control points and non-control points was also investigated. It was found that if non-control points were selected to be samples that there would be a difference between the

known and calculated values of the target. After performing experiments on both transform types and varying the amount of control points available it was shown that both transforms produced results with errors that ranged between within 0.029 mm and 16.7 mm in the worst case. The affine transform showed the smallest errors when compared to the known values of the target. The affine transform was chosen as the better transform of the two based on the size of the errors and used for the project. The final section of this chapter showed a method of measuring simple physical dimensions of a target. The program ruler.m showed that simple horizontal or vertical measurements could be taken.

8.5 References

[1] S. Gernhardt, X. Cong, M. Eineder, S. Hinz, and R. Bamler, “Geometrical Fusion of Multitrack PS Point Clouds,” *IEEE Geosci. Remote Sens. Lett.*, vol. 9, no. 1, pp. 38–42, Jan. 2012.

[2] D. Klimentjew and J. Zhang, “Adaptive sensor-fusion of depth and color information for cognitive robotics,” in *2011 IEEE International Conference on Robotics and Biomimetics*, 2011, pp. 957–962.

Chapter 9 System Validation Results

9.1 Introduction

This chapter shows the results of the experiments required to assess the suitability and viability of performing indoor building inspection using a UAV and suitable sensor suite. The chapter is broken up into sections

9.2 Validating Laser Range Scanner

9.2.1 Drift effects

9.2.8 Simple Coloured Targets

9.2.12 Real Material Targets

9.3 Validating Simulated UAV and Sensor Suite

9.3.1 Real World Test Environment

9.2 Validating Laser Range Scanner

This section focused on using the URG-04LX as a 2D LRS in order to characterise the device so any erroneous effects associated with the device were calibrated and removed from further results.

9.2.1 Experimental Methods: Drift Effects 60 minutes

The experiment is designed to observe and test measurement drift effect associated with the URG-04LX over a specific period of time, similar to those seen in the experiments performed in [1]. The URG-04LX was mounted on the first test rig. A stand was then made to place the target at a specific distance with a constant height. The target for this experiment is a piece of white paper (297mm x 210mm). The test rig was then aligned to measure the distance from the device with an incidence angle of 0° directly in front of the target and a pitch angle of 0°. The actual distance to the target is measured to be 1000mm away from the front of the URG-04LX. The test was performed for 60 minutes and the URG-04LX was ordered to collect range data from scan point 384 which related to

the forward facing scan point with an incidence angle of 0°. The URG-04LX was then programmed to collect range data from this point every 100ms for 60 minutes.

9.2.2 Results: Drift Effects 60 minutes

The experiment was performed as described above with a target of white paper measured at a distance of 1000mm, this was repeated several times (Figure 46). The distance measurements shown in Figure 46 fluctuated with a peak to peak value of about 30-50mm. The distance measurements show that the device measured the distance further away from the distance at which the target was set to (1000mm) at the start of the experiment. The measured distance decreased as time progressed and began to reduce and settle at different times. Plot a settled at around 0.8 hours, plot b settles around 0.4 hours but then became unsettled at 0.9 hours for 0.1 of an hour. Plot c settled at around 0.3 hours and remained settled for the remainder of the experiment. Plot d settled at around 0.6 of an hour, but became unsettled at around 0.9 of an hour.

The average (mean), measure of how spread out the values were (standard deviation) and the most extreme (peak to peak) values of the experiments were seen in Table 14. The means of all of the plots in Figure 46 range between -12mm and +2mm with a standard deviation ranging from 5-8mm. Plot d had the lowest mean to actual target value and max peak-peak value but the highest standard deviation, compared to plot c which had the second lowest mean to actual target value, lowest standard deviation and smallest max peak – peak value. Plots a and b both had similar standard deviation values, max peak – peak values and plot b had the furthest to actual target value mean.

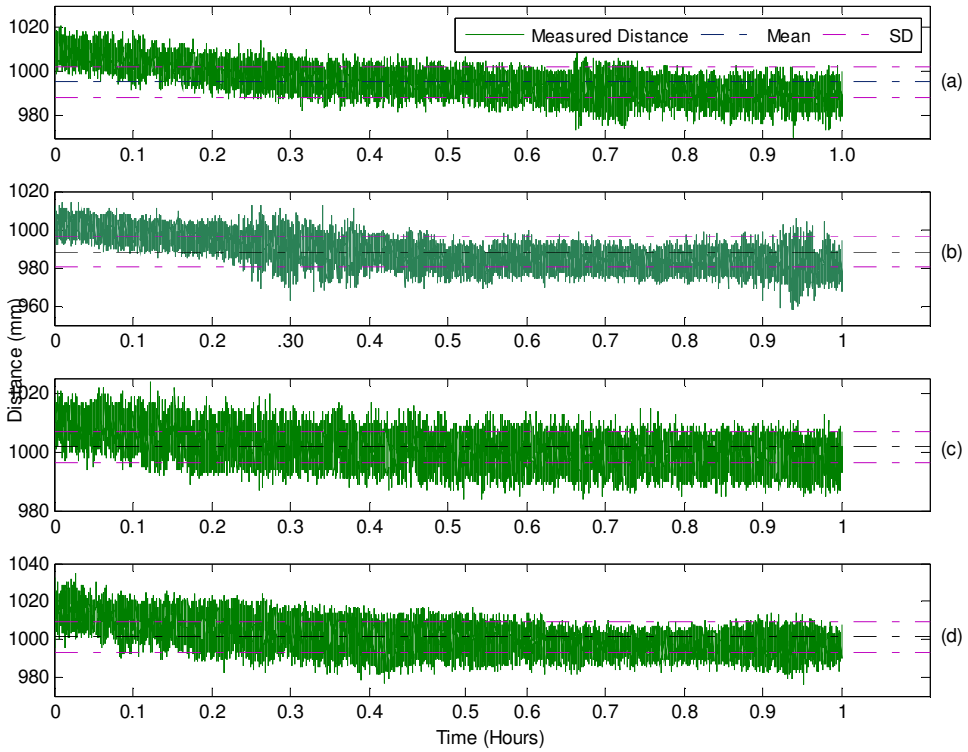

Figure 46 – Distance measurements by the URG-04LX over a 1 hour drift experiment with a white target at a distance of 1000mm

Sample	Mean (mm)	Standard Deviation (mm)	Max Peak – Peak Value (mm)
a	995.3	7.065	51
b	988.3	7.789	56
c	1001	5.257	40
d	1001	7.856	34

Table 14 – Mean, standard deviation and peak to peak values of distance measurements on drift experiment

9.2.3 Discussion: Drift Effects 60 minutes

The mean values in all plots in Figure 46 were between 1-15mm away from the actual known value of the target. When compared to the accuracy value that the URG-04LX is quoted as having an accuracy of ±10mm at a distance of 1000mm under standard conditions. The results show that the URG-04LX had accuracy less than the ±10mm at a distance of 1000mm as quoted by the technical specifications. One of the explanations for this could be due to the increase in temperature in the URG-04LX as the heat from the motor rotating the laser dissipates in the device. The "warm up" time taken for each plot to reach temperature equilibrium between device and environment depends on the temperature of the device when it is turned on and also the ambient temperature of the room. From this it is concluded that the URG-04LX requires a suitable warm up period in order to allow for this temperature equalisation. Looking at the plots in Figure 46 and after analysing the data, additional tests were performed in order to look at the amount of time it takes for the URG-04LX to stabilise its temperature and settle so that the drift effects caused by a lack of warm up time were excluded from the any future results.

9.2.4 Experimental Methods: Drift Effects 240 minutes

The experiment is designed to observe and test measurement drift effect associated with the URG-04LX over a specific period of time. The URG-04LX was mounted on the first test rig. A stand was then made to place the target at a specific distance with a constant height. The target for this experiment was a piece of white paper (297mm x 210mm). The test rig was then aligned to measure the distance from the device with an incidence angle of 0° directly in front of the target and a pitch angle of 0°.This meant that the URG-04LX was parallel to the ground. The actual distance to the target was measured at set to be 1000mm away from the front of the URG-04LX. The test was performed for 240 minutes and the URG-04LX was ordered to collect range data from scan point 384 which related to the forward facing scan point with an incidence angle of 0°. The URG-04LX was then programmed to collect range data from this point every 100ms for 60 minutes. The experiment was conducted in a room illuminated with fluorescent lamps.

9.2.5 Results: Drift Effects 240 minutes

The experiment was performed as described above with a target of white paper measured at a distance of 1000mm and is shown in Figure 47.The distance measurements shown in Figure 47 fluctuate greatly in the first 100 minutes with a peak to peak value of about 200mm. The distance measurements showed that the device measured the distance both further away from and in front of the distance at which the target was set to (1000mm) at the start of the experiment. The measured data stabilised around the actual target distance from 100 minutes into the experiment and the majority of measured distances fit within 1 standard deviation after this time, apart from one obvious anomalous result around 140 minutes. The standard deviation for the entire experiment was 8.3mm with a mean of 1005mm.

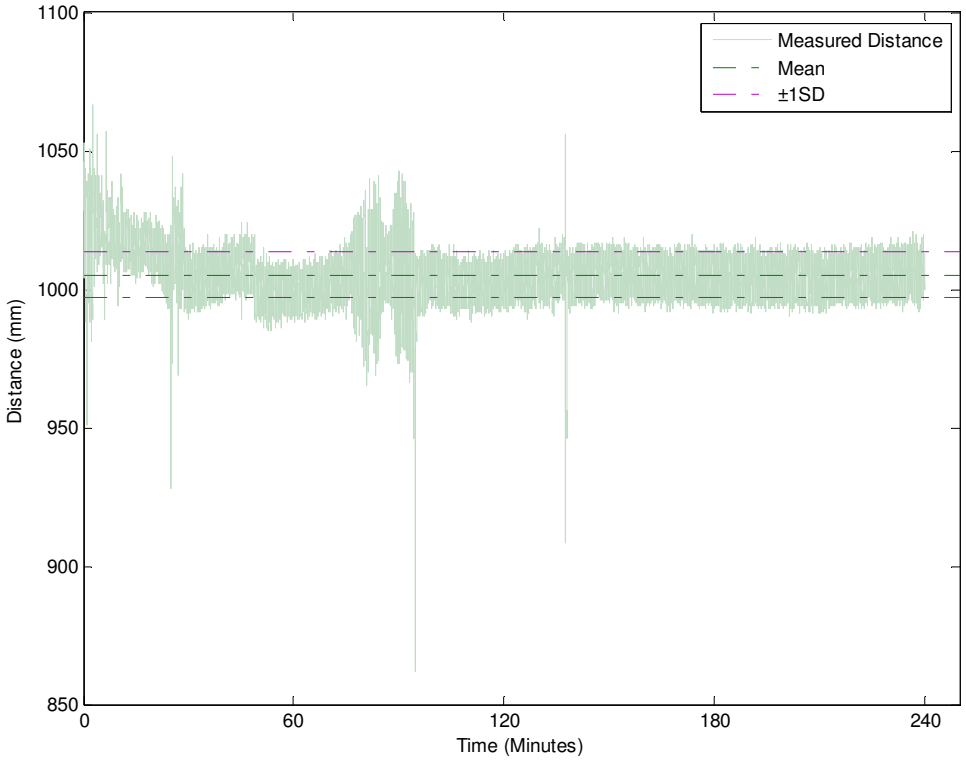

Figure 47 – Distance measurements by the URG-04LX over a 4 hour drift experiment with a white target at a distance of 1000mm

The experimental data was then split into two sections and analysed to find where the warm up point ends and the equilibrium state begins. The two sections were identified and separated in Figure 48. The first 30 minutes of the experiment showed a decrease in measured distance and then

a fluctuating state until 100 minutes. After 100 minutes the measured distances became stable with an anomalous set of points around 140 minutes. After 140 minutes an equilibrium state was observed onwards.

Looking at both samples pre and post 100 minutes it was observed that they had a similar mean of 1007mm and 1004mm respectively. The standard deviation between pre and post 100 minutes had a difference of 6.2mm, with pre 100 minutes standard deviation being 11.24mm and post 100 minutes being 5.029mm. The pre 100 minutes value is larger than the ±10mm accuracy specified by the URG-04LX whereas the post 100 minutes is nearly half the value specified by the URG-04LX. The two pink dotted lines showed two standard deviations between then. It can also be seen that the majority of the post 140 minutes measured distances are within 2 standard deviations of the mean.

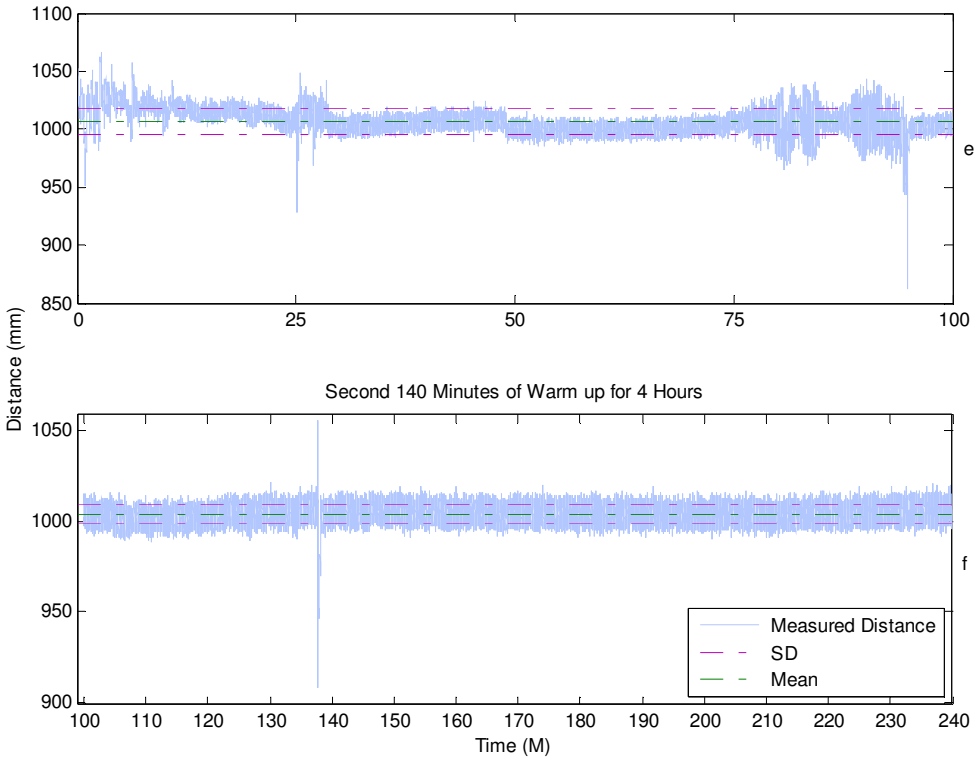

Figure 48 – Distance measurements by the URG-04LX over a 4 hour drift experiment with a white target at a distance of 1000mm. (e) First 100 minutes of the 4 hour warm up period, (f) second 140 minutes of warm up period

Sample	Mean (mm)	Standard Deviation (mm)	Max Peak – Peak Value (mm)
Before 100 Minutes (e)	1007	11.24	200
After 100 Minutes (f)	1004	5.029	148

Table 15 – Mean, standard deviation peak to peak values of distance measurements on drift experiment over 4 hour warm up period

9.2.6 Discussion: Drift Effects 240 minutes

The measured distance mean value calculated from Figure 47 was 1005mm. This was only a 5mm deviation from the actual known value of the target. When compared to the accuracy value that the URG-04LX is quoted as having an accuracy of ±10mm at a distance of 1000mm under standard conditions. The results show that the URG-04LX had accuracy greater than the ±10mm at a distance of 1000mm as quoted by the technical specifications. The increase in accuracy could be due to the increased warm up time. In this experiment we increased the amount of time the URG-04LX was allowed to warm up. The results in Figure 48 showed that the fluctuations in the pre 100 minutes had increased the mean, standard deviation and max peak to peak value seen in overall values in the measured distance by the URG-04LX (Figure 47). The post 100 minute's mean was 0.3% lower than the pre 100 minutes value, also the standard deviation was 76.6% lower as was the max peak to peak value which was 29.9% lower than the pre 100 minutes value. Excluding the pre 100 minutes distance measurements and only using the results post 100 minutes the mean, standard deviation and peak to peak values were reduced and closer to the device specifications. The warm up time required by the URG-04LX so that it measures distance to an accuracy of ±10mm is 140 minutes while working in an operating temperature between 12° and 20°.

In both the 60 and 240 minute experiments the mean value of the measured distance is the most accurate method to determine the actual distance to the target, being within 7mm of the target in all but one case. The use of the mean value of the measured distance is to determine the measured distance to the target.

9.2.7 Conclusion: Drift Effects

The experiment observed and measured the measurement drift effect associated with the URG-04LX over a specific period of time. It is seen in Figure 46 that the URG-04LX fluctuates in returned distance measurements. The “warm up” time taken for each plot to reach temperature equilibrium between device and environment is dependent on the temperature of the device when it is turned on and also the ambient temperature of the room. Leaving the device on for an extended period of time to achieve the equilibrium is required. In the laboratory environment it was found that a minimum time of 140 minutes was required to reach this equilibrium and produce repeatable results from the URG-04LX that measure closely to the specifications given by the URG-04LX of ±10mm. The URG-04LX also produces distance measurements that fluctuate between a peak and trough value, and it is noted that dependence on its position in this cycle affected the measured distance to a target. This means that there is some variation in measured distance values even if the point being measured is exactly the same for each measurement.

9.2.8 Experimental Methods: Effects of Colour on Simple Surfaces

The experiment is designed to observe and test the influence of the surface colour of a target on the URG-04LX’s ability to determine the actual measured distance to the target. The URG-04LX was mounted on the first test rig. A stand was made to place the target at a specific distance with a constant height. The target for this experiment was card (297mm x 210mm) of different surface colours. The test rig was aligned to measure the distance from the device with an incidence angle of 0° directly in front of the target and a pitch angle of 0°.This meant that the URG-04LX was parallel to the ground. The URG-04LX was ordered to collect 1000 measurements from scan point 384 which relates to the forward facing scan point with an incidence angle of 0° for each coloured target. There were 10 different coloured card targets being used in this experiment, pink, white, yellow, blue, green, red, orange, black, grey and silver. Each target was scanned at four different distances, 500mm, 1000mm, 1500mm and 2000mm and the mean value of the distance measurements used. The experiment was conducted in a room illuminated with fluorescent lamps. Before the test, the URG-04LX was turned on for a minimum of 140 minutes to allow the device a suitable warm up period.

9.2.9 Results: Effects of Colour on Simple Surfaces

Results: Effects of Colour on Simple Surfaces at 500mm

The experiment was performed as described above, the data was processed and is presented in Figure 49 and Table 16. It can be seen in Figure 49 that the measurements for the majority of the coloured targets were generally have a single peak around the actual target distance value of 500mm, with the exception of the black, red and silver coloured targets. The majority of the coloured targets lay within ±15mm of the actual target distance with the majority of their peaks being within ±5mm of the actual target distance. The green, pink and blue targets had the highest number of measured distances closest to the actual distance of the target with 289 values measuring 499.8mm, 289 values measuring 500.5mm and 255 values measuring 500.4mm respectively. This was followed by the white target which had 186 values measuring 500.6mm, orange target which had 120 values measuring 500mm, yellow target which had 85 values measuring 499.5mm and the grey target which had 40 values measuring 500.5mm.

The black, red and silver targets had peak measured distance values outside of the majority of targets. The black, red and silver targets had peak values of 455mm, 528mm and 531mm respectively. These values were significantly different from the majority of other coloured target results, either being lower than the actual distance value by 45mm or higher up to 31mm.

The mean and standard deviation value for all of the coloured targets can be seen in Table 16. The mean values for all of the coloured targets were within +31mm or -46mm which is well outside of the accuracy stated in the URG-04LX specifications. If red, black and silver results are excluded for a moment it can be seen that the mean values for pink, white, yellow, blue, green, orange and grey have a maximum variance of between +7mm and -4mm depending on the target. These values are within the URG-04LX specifications. The red and silver coloured targets had higher measured distance values then compared to the other coloured targets. Both targets had similar mean values and a similar spread of distance measurement values. The black coloured target measured a lower distance and mean value than compared to the other coloured targets.

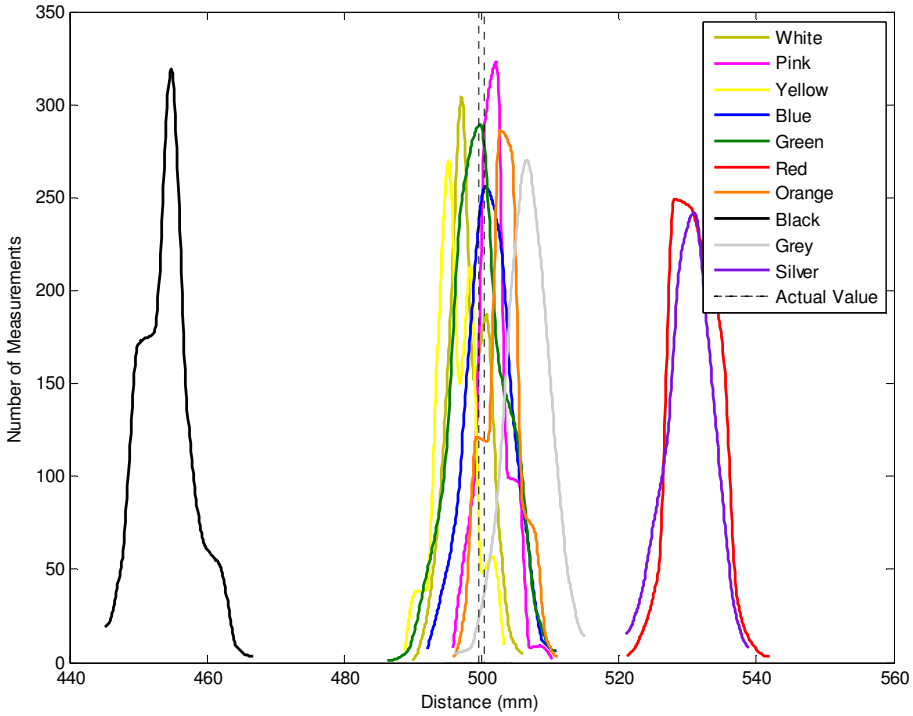

Figure 49 – Distance measurements Histogram by the URG-04LX with targets of varying surface colour at 500mm

Card Colour	Mean (mm)	Standard Deviations (mm)
Red	531.06	4.95
Orange	503.12	2.52
Yellow	496.30	2.76
Green	499.58	3.85
Blue	501.07	3.15
Pink	501.76	2.31
White	498.05	2.64
Black	454.20	3.91
Grey	506.66	3.06
Silver	530.68	3.37

Table 16 – Mean, standard deviation of distance measurements at 500mm

Results: Effects of Colour on Simple Surfaces at 1000mm

The experiment was performed as described above, the data was processed and is presented in Figure 50 and Table 17. It can be seen in Figure 50 that the pink, blue, red, black, grey and silver coloured targets generally have a single peak while the white, yellow and orange coloured targets show more structured results respectively. The majority of the coloured targets lay within ±20mm of the actual target distance with the majority of their peaks being within ±9mm of the actual target distance. The pink target had the highest number of measured distances closest to the actual distance of the target with 297 values measuring 1000mm. The grey coloured target had the next highest amount of distance measurements of 1000mm at 242. The white, orange, blue, green and yellow targets had their highest number of measured distances between 992mm and 994mm. The red and silver coloured targets had peak values of 1018mm measured by 280 points and 1011mm by 222 points respectively. The values of both red and silver were higher than the actual distance of the target by 18mm and 11mm respectively. The black coloured target had a peak value of 936mm measured by 249 points. The value of the black target is lower than the actual distance of the target by 64mm.

The mean and standard deviation values for all of the coloured targets were seen in Table 17. The mean values for all of the coloured targets were within +19mm or -65mm which is outside of the accuracy stated in the URG-04LX specifications of ±10mm. If for a moment the red, black and silver results were excluded it can be seen that the mean values for pink, white, yellow, blue, green, orange and grey had a maximum variance of between +0.2mm and -9mm depending on the target. These values were below the URG-04LX specifications. Observing the red, black and silver coloured targets it can be seen that the red and silver coloured targets had higher measured distance values than compared to the other coloured targets. Both targets had similar mean values and a similar spread of distance measurement values. The black coloured target had lower measured distance and mean values than compared to the other coloured targets.

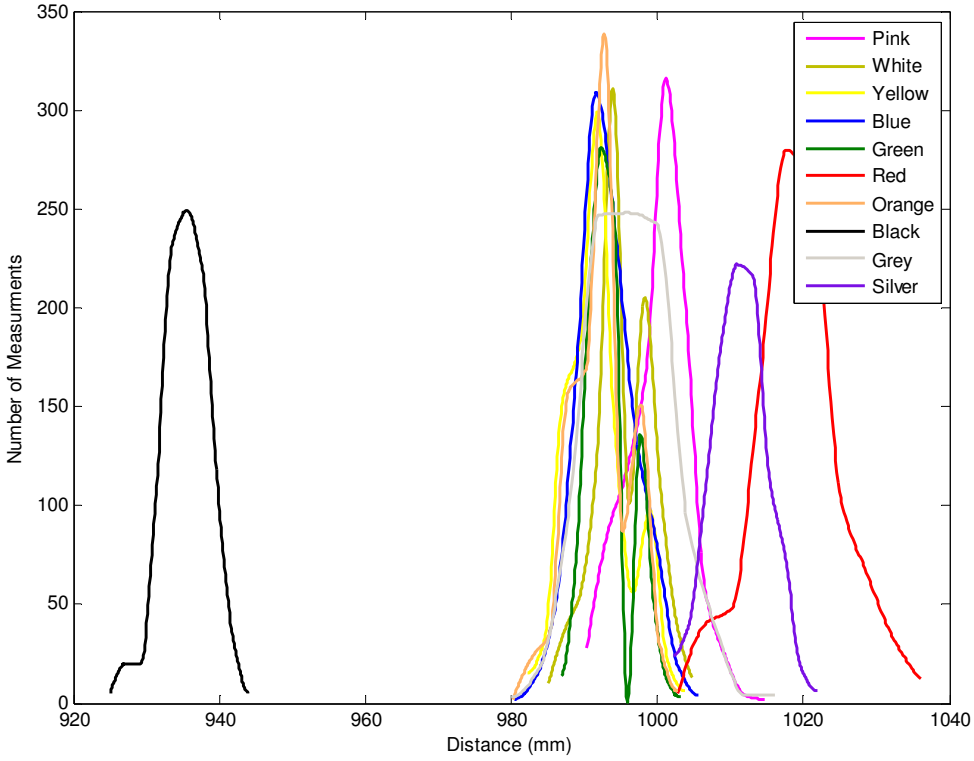

Figure 50 – Distance measurements Histogram by the URG-04LX with targets of varying surface colour at 1000mm

Card Colour	Mean (mm)	Standard Deviations (mm)
Red	1019.70	4.69
Orange	992.51	3.96
Yellow	991.97	4.21
Green	993.43	3.02
Blue	993.34	3.97
Pink	1000.20	4.15
White	995.49	3.96
Black	935.39	3.08
Grey	996.77	5.50
Silver	1011.30	3.93

Table 17 – Mean, standard deviation of distance measurements at 1000mm

Results: Effects of Colour on Simple Surfaces at 1500mm

The experiment was performed as described above, the data was processed and is presented in Table 18 and Figure 51. It can be seen in Figure 51that the white, pink, red, yellow, green, grey and silver coloured targets generally have a single peak while the black, silver, orange and blue coloured targets show more structured results. The majority of the coloured targets lay within ±20mm of the actual target distance with the majority of their peaks being within ±7mm of the actual target distance. The yellow target had the mode of distribution closest to the actual distance of the target with 162 values measuring 1500mm. The grey and red coloured targets had the next highest amounts of distance measurements of 1500mm at 161 and 158. The white and green had their peak values at 1494mm and were below the actual target distance by 6mm. The yellow, blue, pink, orange, grey and red had peak values that range from 1502mm to 1508mm. The silver coloured target had peak values of 1534mm measured by 237 points and is 34mm above the actual target distance. The black coloured target had a peak value of 1470mm measured by 216 points and is 30mm below the actual target distance.

The mean and standard deviation values for all of the coloured targets were seen in Table 18. The mean values for all of the coloured targets were within +37mm or -33mm which is outside of the accuracy stated in the URG-04LX specifications for scanning at 1500mm of ±15mm. If for a moment the black and silver results were excluded it can be seen that the mean values for pink, white, yellow, blue, green, orange, red and grey had a maximum variation of between +6mm and -5mm depending on the target. These values were below the ±10mmURG-04LX specifications. The silver coloured target is seen to have a higher measured distance values then compared to the other coloured targets. The black coloured target had the lowest measured distance and mean values than compared to the other coloured targets.

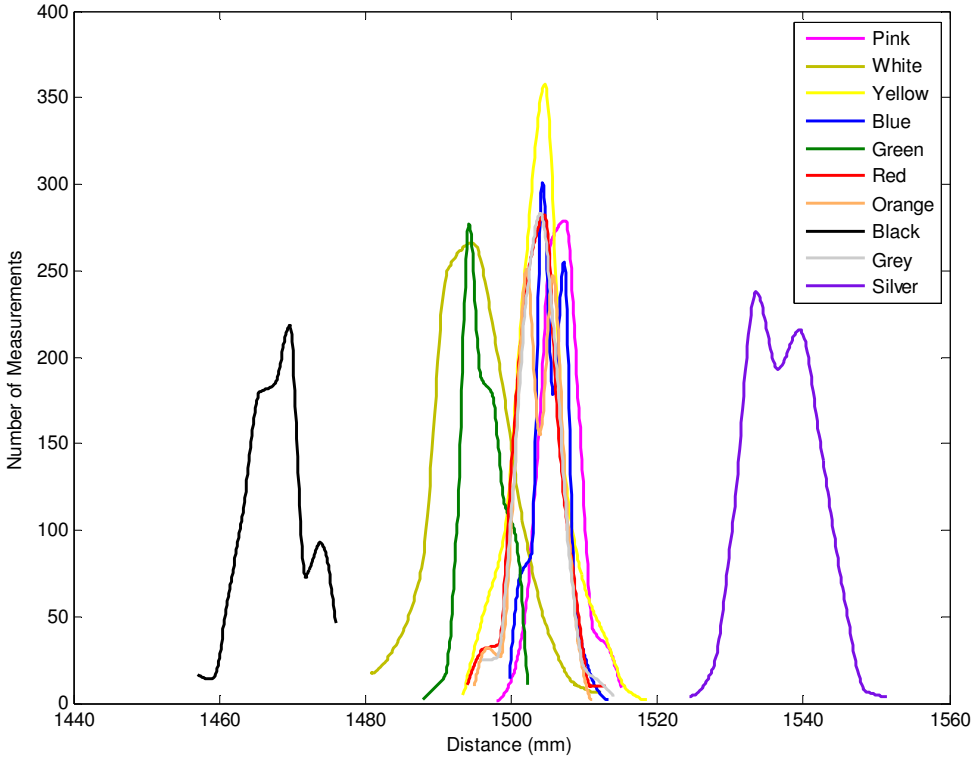

Figure 51 – Distance measurements Histogram by the URG-04LX with targets of varying surface colour at 1500mm

Card Colour	Mean (mm)	Standard Deviations (mm)
Red	1503.50	3.03
Orange	1503.70	2.85
Yellow	1504.20	3.82
Green	1496.10	2.47
Blue	1505.60	2.25
Pink	1506.80	2.94
White	1495.10	5.44
Black	1467.70	3.90
Grey	1504.20	2.94
Silver	1537.70	4.66

Table 18 – Mean, standard deviation of distance measurements at 1500mm

Results: Effects of Colour on Simple Surfaces at 2000mm

The experiment was performed as described above, the data was processed and is presented in Table 19 and Figure 52. It is seen in Figure 52 that the white, orange, red, pink and silver coloured targets generally have a single peak while the blue, black, yellow, grey and green coloured target have more structure. The majority of the coloured targets lay within ±20mm of the actual target distance with the majority of their peaks being within ±11mm of the actual target distance. The orange target had the highest number of measured distances closest to the actual distance of the target with 246 values measuring 2000mm. The blue and black coloured targets had the next highest amounts of distance measurements of 2000mm at 216 and 204. The blue and orange had their peak values at 1998mm and were below the actual target distance by 1.2mm. The grey, yellow, black, white, green, red and pink had peak values that range from 1990mm to 2010mm. The black coloured target had a peak value of 1994mm which are closer to the actual target than in any previous experiments performed so far and even had a higher peak value than grey or yellow. The silver coloured target had peak values of 2024mm measured by 300 points and is 24mm above the actual target distance.

The mean and standard deviation value for all of the coloured targets is shown in Table 19. The mean values for all of the coloured targets were within +22mm or -9.1mm which is marginally outside of the accuracy stated in the URG-04LX specifications for scanning at 2000mm of ±20mm.

If for a moment the silver and blue results were excluded it is seen that the mean values for pink, white, yellow, green, orange, red, black and grey had a maximum variance of between -9.1mm and +9.91mm depending on the target. These values were below the ±10mm URG-04LX specifications. The silver coloured target showed that it had a higher measured distance values than compared to the other coloured targets.

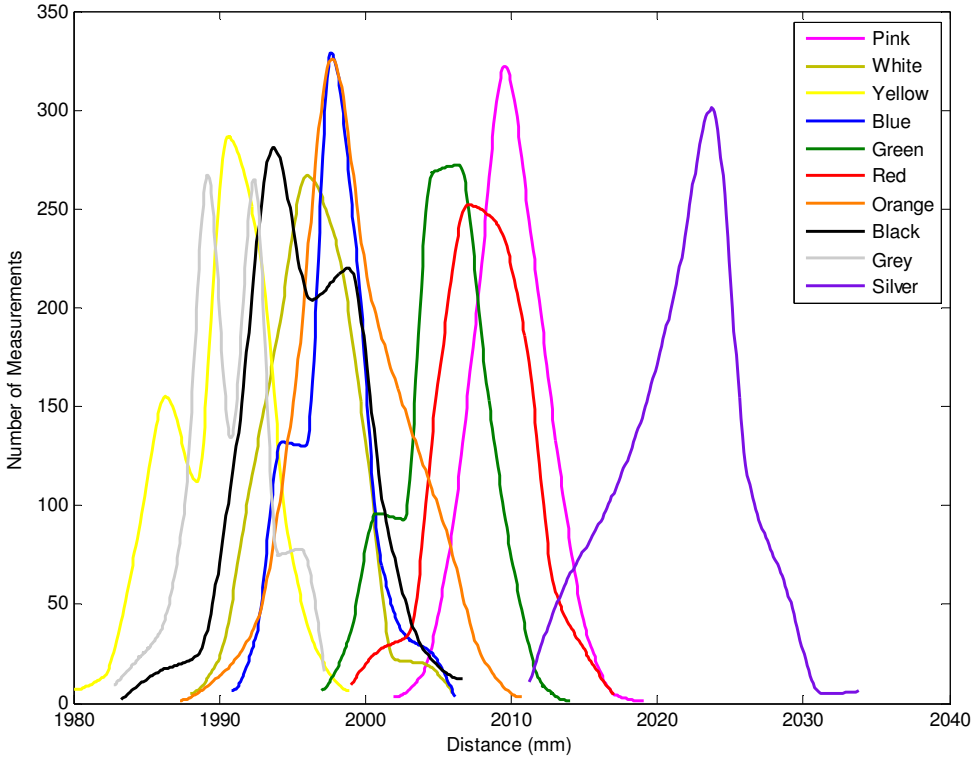

Figure 52 – Distance measurements Histogram by the URG-04LX with targets of varying surface colour at 2000mm

Card Colour	Mean (mm)	Standard Deviations (mm)
Red	2008.60	3.06
Orange	1999.40	3.72
Yellow	1990.00	3.19
Green	2006.00	2.82
Blue	1997.80	2.55
Pink	2009.90	2.57
White	1995.90	2.98
Black	1996.10	3.89
Grey	1990.90	2.79
Silver	2022.00	4.05

Table 19 – Mean, standard deviation of distance measurements at 2000mm

9.2.10 Discussion: Effects of Colour on Simple Surfaces

Discussion: Effects of Colour on Simple Surfaces at 500mm

The results in Table 16 and Figure 49 showed that there is a varying influence of the surface colour of a target on the URG-04LX's ability to determine the actual measured distance to the target. The accuracy of the URG-04LX while scanning pink, white, yellow, blue, green, orange and grey targets is within the specified limits (±10mm). The pink, green, blue, orange, red, silver, black and grey coloured targets have a single peak in Figure 49 while the white, yellow coloured targets show more structured results respectively. The pink, green blue, orange and grey coloured targets had measured distance values which were all tightly grouped around the actual target value. The width of the target value is determined by the width of the bin, and explains why the target value is not a single line. It is observed that the URG-04LX could accurately measure these coloured targets to within ±10mm accuracy. The red and silver coloured targets were grouped closely together in their measured distance spread and mean at around 530mm suggesting that they both affect the ability of the URG-04LX to determine the actual measured distance to the target by increasing the measured distance. The black coloured target was the only target to underestimate the distance to the coloured target. The underestimate was 46mm at its peak and even at its largest distance value was still 34mm below the actual targets distance. One explanation for the increase/decrease in the distance measurements observed when using the targets could be that the light emitted from the URG-04LX be partially or fully absorbed by the surface or that the phase of the returning light wave had changed. The URG-04LX would not be aware that the change was due to the surface colour of the target and still compare the phase of the returning wave to the known phase of the initial emitted wave. This would then make the URG-04LX calculate the distance measurement to the target incorrectly compared to the targets actual value. If the phase and magnitude data could be gathered directly from the laser range scanner before being processed into ASCII the effects of magnitude and phase could be observed. As direct access to the magnitude and phase is not possible using the prewritten commands that the laser range finder it is not possible to determine at this point if magnitude or phase are directly having an effect on the ability of the laser range scanner. The next set of experiments compared surface colour to see if the effect trend continues as distance to the target is increased.

Discussion: Effects of Colour on Simple Surfaces at 1000mm

The results in Table 17 and Figure 50 show that there is an influence on the URG-04LX's ability to determine the actual measured distance to the target and the surface colour of a target. The green, pink, grey, blue, orange, yellow and white coloured targets had measured distance peak values which were all tightly grouped closely (±10mm)around the actual target value. The measurements taken show that none of the targets produced distance measurements that were completely within the specified limits (±10mm). The pink coloured target was closest target to meet the accuracy specifications with a variance of +14mm and -10 mm. The mean values in Table 17 for the pink, white, yellow, blue, green, orange and grey showed that there is a variance of -9mm and +0.2mm between targets. This data showed that the mean values of the measured distance give the results closest the actual target distance value and were higher than the accuracy specified for the URG-04LX. For the red and silver coloured targets the mean distance value was 1019mm and 1011mm respectively. The mean value is closer to the actual target value and is closer than the values in the Effects of Colour on Simple Surfaces at 500mm experiment. This could suggest that as the distance to the target increases the effects such as scattering, reflectance and absorption were also changing, in a way that is reducing the overestimate of distance measurements made by the URG-04LX on red and silver coloured target. Conversely it can be seen that as the distance to the target was increased the mean value for black decreased when compared to the results in Effects of Colour on Simple Surfaces at 500mm experiment.

Discussion: Effects of Colour on Simple Surfaces at 1500mm

The results in Figure 51 and Table 18 show that there is an influence on the URG-04LX's ability to determine the actual measured distance to the target and the surface colour of a target. The pink, green, grey, orange, blue, red, yellow and white coloured targets had measured distance peak values which were all tightly grouped closely (±8mm)around the actual target value. The measurements taken show that none of the targets produced distance measurements that were completely within the specified limits (±15mm). The mean values in Table 18 for the pink, white, yellow, blue, green, red, orange and grey showed that there is a variance of +6mm and -5mm between targets. This data showed that the mean values of the measured distance give the results closest the actual target distance value and were higher than the accuracy specified for the URG-04LX. For silver coloured

target the mean distance value is 1537.7mm. The mean value is +37mm above the actual targets distance value and which is similar to the values recorded in the Effects of Colour on Simple Surfaces at 500mm experiment. This could suggest that as the distance to the target increases the effects such as reflectance and absorption is also changing, in a way that is similar to the results shown in Effects of Colour on Simple Surfaces at 500mm experiment. It is seen that as the distance to the target is increased the mean value for black got closer to the actual target distance.

Discussion: Effects of Colour on Simple Surfaces at 2000mm

The results in Table 19 and Figure 52 show that there is an influence on the URG-04LX's ability to determine the actual measured distance to the target and the surface colour of a target. The pink, green, grey, orange, blue, red, black, yellow and white coloured targets had measured distance peak values which were all tightly grouped closely (±11mm)around the actual target value. The values show that these targets produced the majority of distance measurements were within the specified accuracy limits of (±20mm), with the exception of the silver target which overestimated the distance to the target by 24mm.

The mean values in Table 19 for the pink, white, yellow, blue, green, red, black, orange and grey showed that there is a variance of +9.9mm and -9.1mm variance between targets. This data showed that the mean values of the measured distance give the results closest the actual target distance value and were higher than the accuracy specified for the URG-04LX. For silver coloured target the mean distance value is 2022mm The mean value is +22mm above the actual targets distance value and which is similar to the values recorded in the Effects of Colour on Simple Surfaces at 500nad 1000 and 1500mm experiment. It is seen that as the distance to the target is increased the mean value for black tended to be closer to the actual target distance.

9.2.11 Conclusion: Effects of Colour on Simple Surfaces

The experiment into the effects of colour on simple surfaces show that the colour of the target effects the measured distance to the target by the URG-04LX. The pink, white, yellow, blue, green, orange and grey coloured targets produce the majority of distance measurements that were within ±20mm of the actual target. The mean of these targets were generally within ±10% of the actual target value and depending on the distance the URG-04LX is measuring from, this value could be as low as ±1% with certain targets. The red and silver coloured targets had recorded the distance

to the target higher than the actual value of the target. When compared to other coloured targets in the 500mm and 1000mm experiments both the red and silver targets produce values between 15mm and 30mm above the actual target distance. In the 1500mm and 2000mm experiments the distance measurements of the silver target remained higher than the actual target by 20-40mm. The red targets over measurement of the actual target distance in the same experiments had reduced to +10mm higher than the target distance. The black coloured target had a mean value lower than the actual target distance in the 500mm, 1000mm, and 1500mm experiments which range from -37mm to -65mm. In the 2000mm experiment the values of the black coloured targets distance moved closer to that of the target distance and its mean reduced to within -4mm of the actual target value.

Looking at the data produced from this set of experiments it is seen that the black underestimates, the red and silver overestimate with the exceptions mentioned the distance to the target. The other targets measured the distance to within ±20mm depending on the target and distance to target. The spread and apparent over and under measurements of the coloured targets could be explained by the effect the coloured card had on the target. Black targets absorbed more of the energy from the laser beam which altered the amplitude of the returning laser beam, where the silver targets reflected a percentage the laser beam away from the receiver on the URG-04LX. The URG-04LX also scanned the targets at different times, and as seen in Figure 47 and Figure 48 even after the warm up time had passed and the device reached equilibrium the values measured could vary by up to ±10mm. It should also be taken into account that any large spikes such as those seen Figure 47 between 130 – 140 minutes appeared and created anomalies in the resulting distance measurement.

The next set of experiments looks at objects and surfaces that could be encountered in real life indoor building inspections and observed the ability of the URG-04LX to measure these targets.

9.2.12 Experimental Methods: Real Materials effects on Range Measurements

The experiment is designed to observe and test the influence of real world materials typically found when conducting indoor building inspections and how it affects the URG-04LX's ability to determine the actual measured distance to the target. The URG-04LX is mounted on the first test rig. A stand is then made to place the target at a specific distance with a constant height. The targets for this experiment were a Steel Sheet, Steel Beam, Polystyrene Block, Breeze Block, Red Brick and a Wooden Block. The test rig is then aligned to measure the distance from the device with an incidence angle of 0° directly in front of the target and a pitch angle of 0°.This meant that the

URG-04LX is parallel to the ground. The URG-04LX is ordered to collect 1000 measurements from scan point 384 which relates to the forward facing scan point with an incidence angle of 0° for each coloured target. Each different target is scanned at four different distances, 500mm, 1000mm, 1500mm and 2000mm and the mean value of the distance measurements were used. The experiment is conducted in a room illuminated with fluorescent lamps. Before the test, the URG-04LX is turned on for a minimum of 140 minutes to allow the device a suitable warm up period.

9.2.13 Results: Real Materials effects on Range Measurements

Results: Real Materials effects on Range Measurements at 500mm

The experiment was performed as described above, the data is processed and is presented in Table 20 and Figure 53. The experiment into the effects of colour on simple surfaces show that the colour of the target effects the measured distance to the target by the URG-04LX. The steel beam and red brick were the only two targets to have had their peak values within the ±10mm of the actual target distance. The breeze block and wood brick had peak values that were within ±20mm with the polystyrene blocks peak value 1mm above ±20mm. The steel sheet had the highest peak value of 546mm which is 46mm above the actual distance to the target. None of the target had all of their distance measurements within ±10mm of the target distance.

The mean and standard deviation values for the targets were seen in Table 20. The mean values for the targets were within +56mm or -11mm which is outside of the accuracy stated in the URG-04LX specifications for scanning at 500mm of ±10mm.

If the sheet steel result is excluded for a moment it is seen that the mean values of the other targets had a maximum variance of between -11mm and +23mm depending on the target. These values were closer, but were still higher compared to the ±10mm URG-04LX specifications.

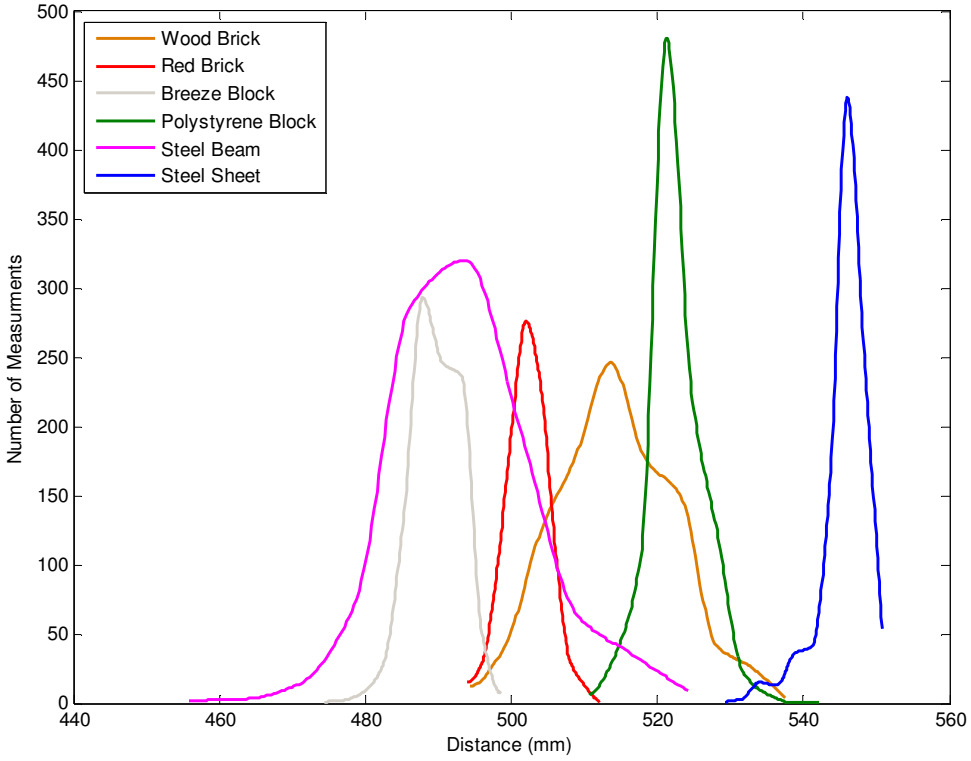

Figure 53 – Distance measurements Histogram by the URG-04LX with realistic targets at 500mm

Target	Mean (mm)	Standard Deviations (mm)
Steel Sheet	556.14	6.22
Steel Beam	493.68	9.73
Polystyrene Block	522.88	3.77
Breeze Block	489.62	3.31
Red Brick	502.64	3.00
Wood Brick	516.04	4.44

Table 20 – Mean, standard deviation of distance measurements at 500mm

Results: Real Materials effects on Range Measurements at 1000mm

The experiment was performed as described above, the data is processed and is presented in Table 21 and Figure 54. The experiment into the effects of colour on simple surfaces show that the colour of the target effects the measured distance to the target by the URG-04LX. The steel beam, red brick, wood brick and breeze block were the only targets to have had their peak values within the ±10mm of the actual target distance. The polystyrene block had a peak value at 1030mm and the steel sheet had a peak value at 1036mm. None of the target had all of their distance measurements within ±10mm of the target distance.

The mean and standard deviation values for the targets were seen in Table 21. The mean values for the targets were within +36mm or -10mm, the positive value is outside of the accuracy stated in the URG-04LX specifications for scanning at 1000mm, namely ±10mm.

If the sheet steel and polystyrene block results were excluded for a moment it is seen that the mean values of the other targets had a maximum variance of between -10mm and +8mm depending on the target. These values were closer, and met the ±10mm URG-04LX accuracy specifications.

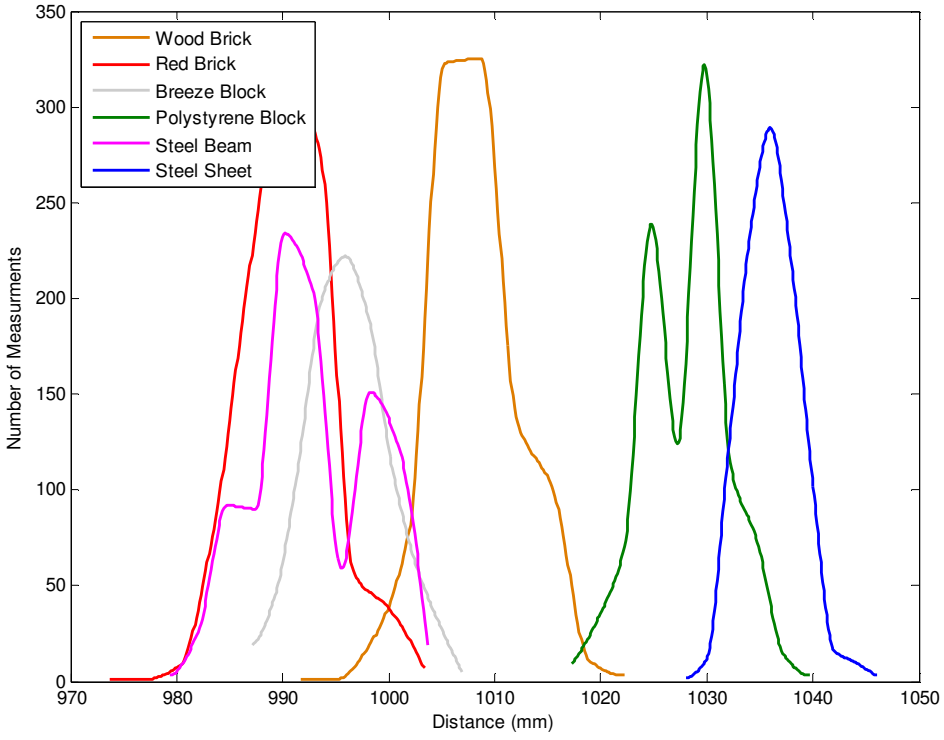

Figure 54 – Distance measurements Histogram by the URG-04LX with realistic targets at 1000mm

Target	Mean (mm)	Standard Deviations (mm)
Steel Sheet	1036.5	2.66
Steel Beam	992.76	5.21
Polystyrene Block	1028.20	4.01
Breeze Block	996.25	3.96
Red Brick	990.57	4.10
Wood Brick	1008.30	4.07

Table 21 – Mean, standard deviation of distance measurements at 1000mm

Results: Real Materials effects on Range Measurements at 1500mm

The experiment was performed as described above, the data is processed and is presented in Table 22 and Figure 55. The experiment into the effects of colour on simple surfaces show that the colour of the target effects the measured distance to the target by the URG-04LX. In this experiment none of the targets had their peak values within the ±15mm of the actual target distance working at a distance of 1500mm. The wooden block had the closest peak measurement value to the actual target distance of 1500mm, followed by the polystyrene block with a peak value of 1520mm. The red brick had a peak value of 1478mm which is 22mm below the actual distance of the target. The breeze block and steel beam both had peak values if 1456mm and 1455mm respectively. The steel sheet over measured the target distance by 55mm giving a peak value of 1555mm.

The mean and standard deviation values for the targets were seen in Table 22. The mean values for the targets were within +54mm or -47mm, the positive value is outside of the accuracy stated in the URG-04LX specifications for scanning at 1500mm of ±15mm. The wooden block and polystyrene block had the closest mean values to the actual target distance, but even these were still outside the URG-04LX specified accuracy.

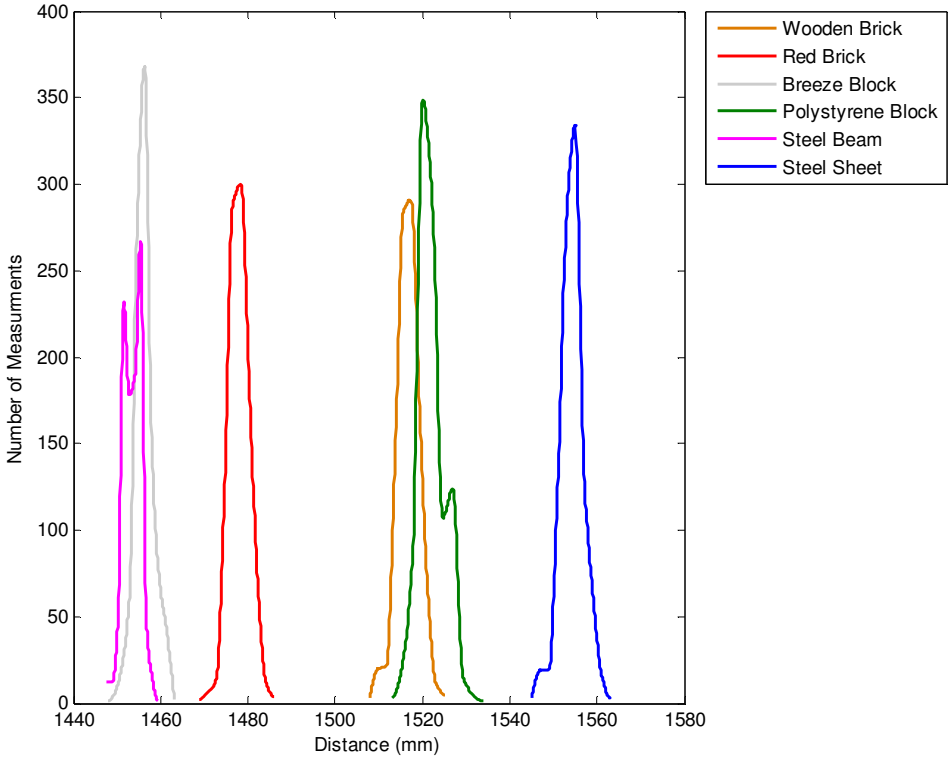

Figure 55 – Distance measurements Histogram by the URG-04LX with realistic targets at 1500mm

Target	Mean (mm)	Standard Deviations (mm)
Steel Sheet	1554	2.68
Steel Beam	1453.50	2.03
Polystyrene Block	1522.00	3.10
Breeze Block	1456.20	2.23
Red Brick	1478.00	2.47
Wood Brick	1516.80	2.69

Table 22 – Mean, standard deviation of distance measurements at 1500mm

Results: Real Materials effects on Range Measurements at 2000mm

The experiment was performed as described above, the data is processed and is presented in Table 23 and Figure 56. The experiment into the effects of colour on simple surfaces show that the colour of the target effects the measured distance to the target by the URG-04LX. In this experiment wood brick, steel beam, polystyrene block, red brick and breeze block targets had their peak values within the ±20mm of the actual target distance working at a distance of 2000mm. The steel beam had the closest peak measurement value to the actual target distance of 1998mm, followed by the wooden block with a peak value of 2007mm. The polystyrene block and red brick had peak values of 1986mm and 1985mm which is 14mm and 15mm below the actual distance of the target and . The breeze block had a peak values if 1985mm. The steel sheet had over measured the target distance by 37mm giving a peak value of 12037mm.

The mean and standard deviation values for the targets were seen in Table 23. The mean values for the targets were within +37mm or -15mm, the positive value is outside of the accuracy stated in the URG-04LX specifications for scanning at 2000mm of ±20mm. If for a moment the steel sheet result were excluded it is seen that the mean values of the other targets had a maximum variance of between +6mm and -15mm depending on the target. These values were below the limits accuracy stated in the URG-04LX specifications.

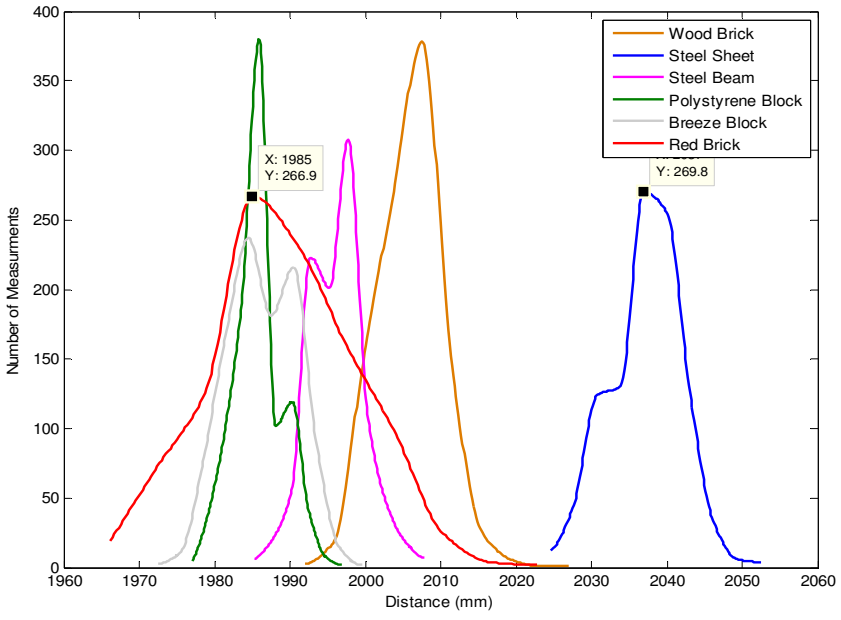

Figure 56 – Distance measurements Histogram by the URG-04LX with realistic targets at 2000mm

Target	Mean (mm)	Standard Deviations (mm)
Steel Sheet	2037.2	4.65
Steel Beam	1996.50	3.71
Polystyrene Block	1985.90	3.34
Breeze Block	1986.80	4.59
Red Brick	1988.80	9.94
Wood Brick	2005.90	4.33

Table 23 – Mean, standard deviation of distance measurements at 2000mm

9.2.14 Discussion: Real Materials effects on Range Measurements

Discussion: Real Materials effects on Range Measurements at 500mm

The results in Table 20 and Figure 53 show that there is an influence on the URG-04LX's ability to determine the actual measured distance to the target and the surface colour of a target. The steel beam, breeze block, red brick and wood brick targets had measured distance peak values which were all grouped around the actual target value (±13mm). The values show that these targets produced the majority of distance measurements were close to the specified accuracy limits of (±10mm), with the exception of the polystyrene block and steel sheet targets which overestimated the distance to the target by 21mm and 46mm respectively.

Discussion: Real Materials effects on Range Measurements at 1000mm

The results in Table 21 and Figure 54 show that there is an influence on the URG-04LX's ability to determine the actual measured distance to the target and the surface colour of a target. The steel beam, breeze block, red brick and wood brick targets had measured distance peak values which were all grouped around the actual target value (±10mm). The values show that these targets

produced the majority of distance measurements were close to the specified accuracy limits of (±10mm), with the exception of the polystyrene block and steel sheet targets which overestimated the distance to the target by 30mm and 36mm respectively.

Discussion: Real Materials effects on Range Measurements at 1500mm

The results in Table 22 and Figure 55 show that there is an influence on the URG-04LX's ability to determine the actual measured distance to the target and the surface colour of a target. None of the targets peak values were within the specified accuracy of the URG-04LX of ±15mm at 1500mm. The values for this experiment were very different than those seen in the 500mm and 1000mm experiments. In the previous real materials experiments the majority of the targets tended to be within ±20mm of the target distance. In this experiment the majority of the targets had values which ranged from +22mm to +55mm which is an over estimate of the target distance by -22mm to -43mm. The closest target to the actual value is the wooden block, which even then had a mean value of +16.8mm, which is over the specified accuracy of the URG-04LX. The increase in distance to the target had an effect on the ability of the URG-04LX to detect the distance to these real materials. In this experiment the ability to measure the distance to the target had been hindered by the increase in distance to the target, making it return distance measurements that were not within the specified tolerances to the device.

Discussion: Real Materials effects on Range Measurements at 2000mm

The results in Table 23 and Figure 56 show that there is an influence on the URG-04LX's ability to determine the actual measured distance to the target and the surface colour of a target. Five out of the six targets peak values were within the specified accuracy of the URG-04LX of ±20mm. The values for this experiment were similar to those seen in the 500mm and 1000mm. The steel beam, breeze block, red brick and wood brick, polystyrene block and breeze block targets had measured distance peak values which were all grouped around the actual target value (±20mm). The steel sheet target again overestimated the distance to the target by 37mm.

The values show that these targets produced the majority of distance measurements that were close to the specified accuracy limits of (±20mm), with the exception of the steel sheet targets which overestimated the distance to the target by 30mm and 37mm.

9.2.15 Conclusion: Real Materials effects on Range Measurements

The experiment into the effects real material surfaces show that the different types of target effects the measured distance to the target by the URG-04LX. The wood brick, red brick, breeze block and steel beam coloured targets produce a majority of distance measurements that were within ±20mm of the actual target. The steel sheet target recorded consistently overestimated distances compared to the actual target distance than any other target. This could be due to the highly polished surface of the steel target, scattering the laser beam away from the target rather than returning it to the receiver in the device. The only exception to this conclusion is the 1500mm experiment, as the values recorded by the URG-04LX showed that none of the targets produced distance measurements that were within the ±15mm accuracy limits.

From this experiment it is concluded that the URG-04Lx did measure accurately measure “real life” targets of varying colour and texture, but not accurately measure highly polished targets due to scattering effect. It can also be seen in the specification of the URG-04LX [2]that as the distance to the target increases the accuracy tolerance increases to 1% of the distance to the target. This increase in in tolerance means that the ability to detect the actual distance to a target is impaired as the distance to the target is increased. This can be seen in sub subsection 9.2.13 where the closet mean values were greater than tolerance values quoted by the specification. From this it is decided that the distance measurements for experiments are performed up to a maximum of 1Meter away from the target so as to reduce the tolerance of the measured distance values.

9.3 Validating Simulated UAV and Sensor Suite

9.3.1 Real World Test Environment

This experiment is designed to observe and test the ability of the sensor suite to measure the range and gather visual images to an example of an environment it could encounter whilst performing an indoor building inspection. The simulated UAV is originally positioned 960mm away from the target and aligned to measure the distance from the device with an incidence angle of 0°, directly in front

of the target. The simulated UAV is then positioned around the target at different incidence angles and at different distances in order to simulate how a UAV would scan a target in a real situation. The targets used in this experiment comprised of breezeblocks, bricks and plank of wood (Figure 57 and Figure 58).

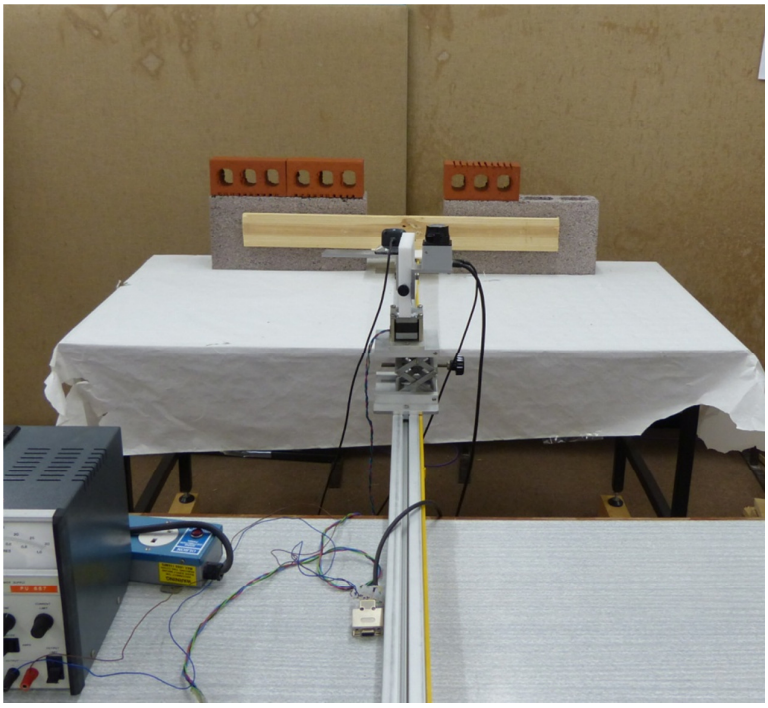

Figure 57 – Simulated UAV scanning real environment targets

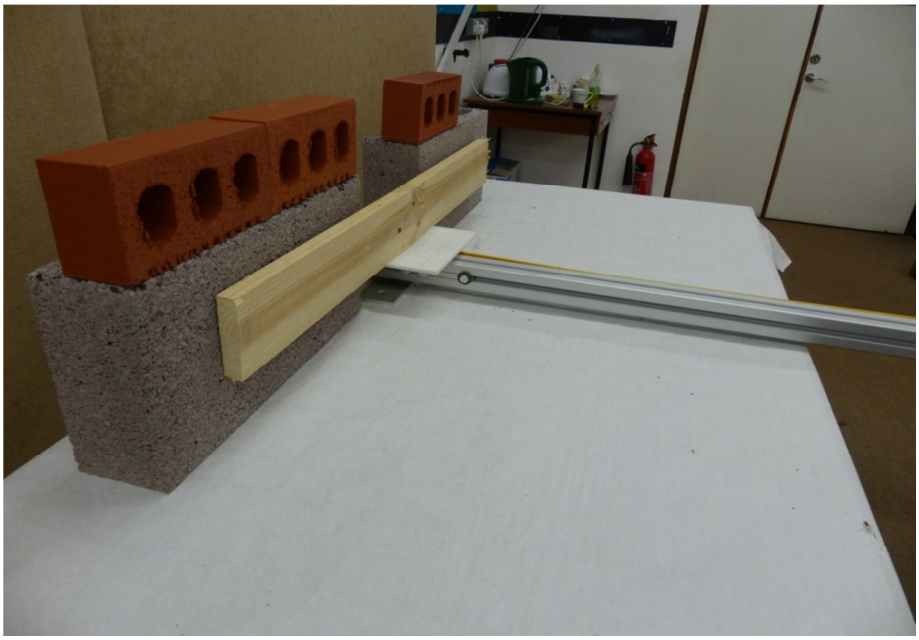

Figure 58 – Real environment targets

9.3.2 Results

The experiment was performed as described above. The data collected is processed and is presented as a point cloud and a mesh, Figure 59 and Figure 60 respectively. Visual images gathered from the VX-500 at the same pitch angle but with varying angles of θ can be seen in Figure 61, Figure 62 and Figure 63

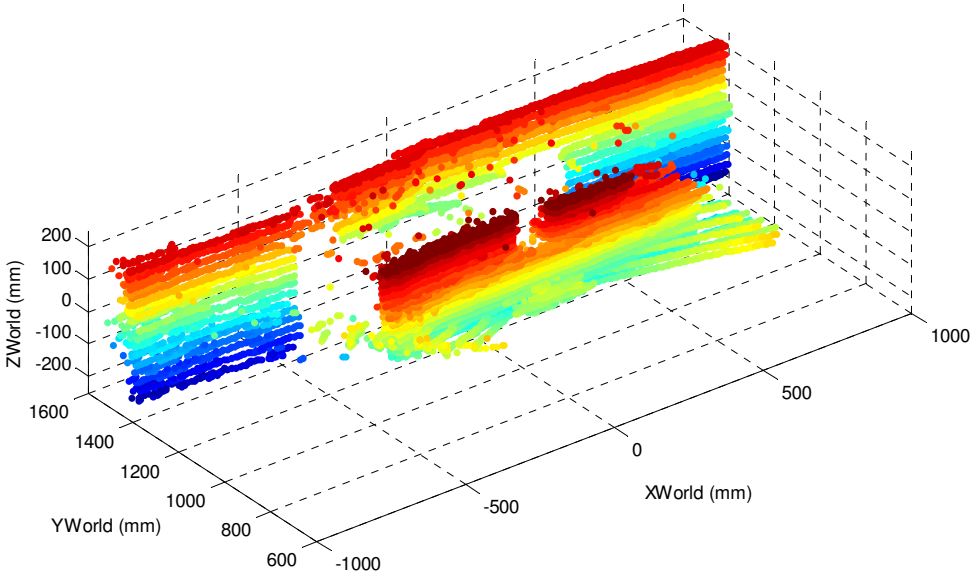

Figure 59 – Point cloud of real environment

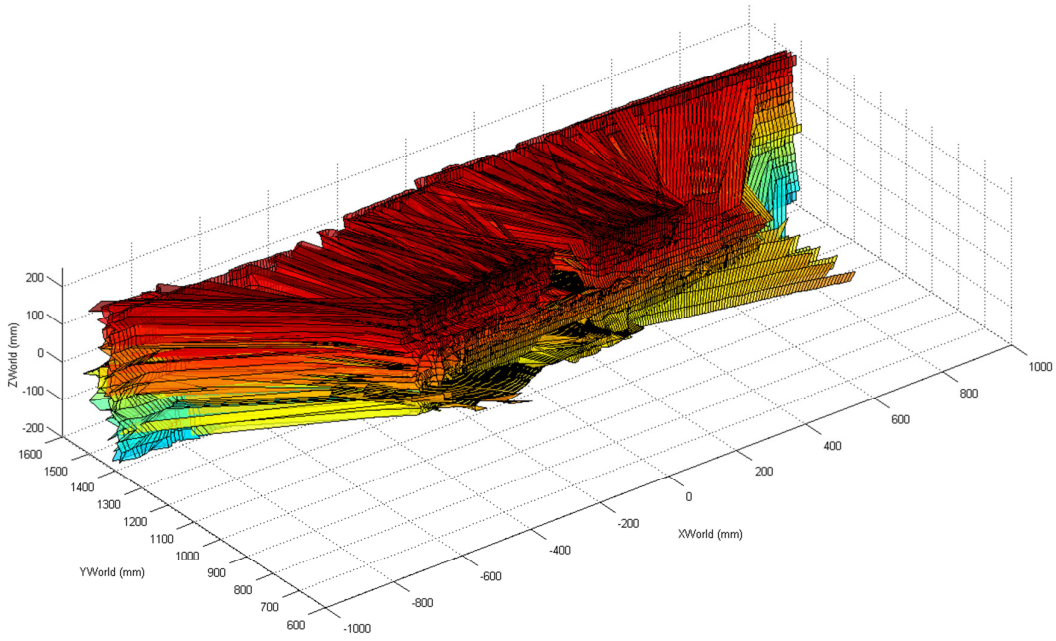

Figure 60 – Mesh of real environment

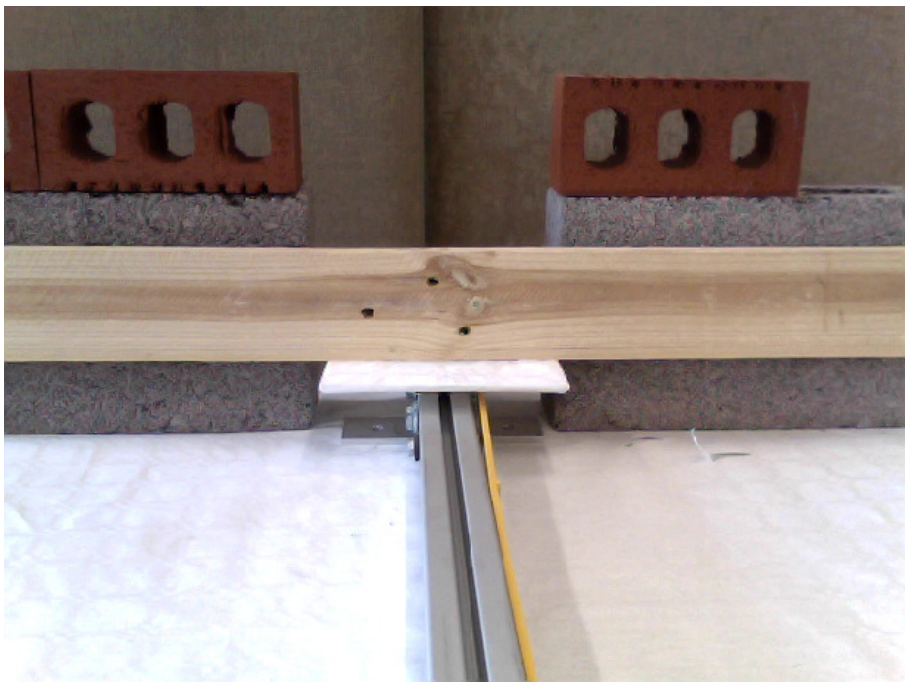

Figure 61 – Image from the VX-500 at 0° θ with at 5° pitch

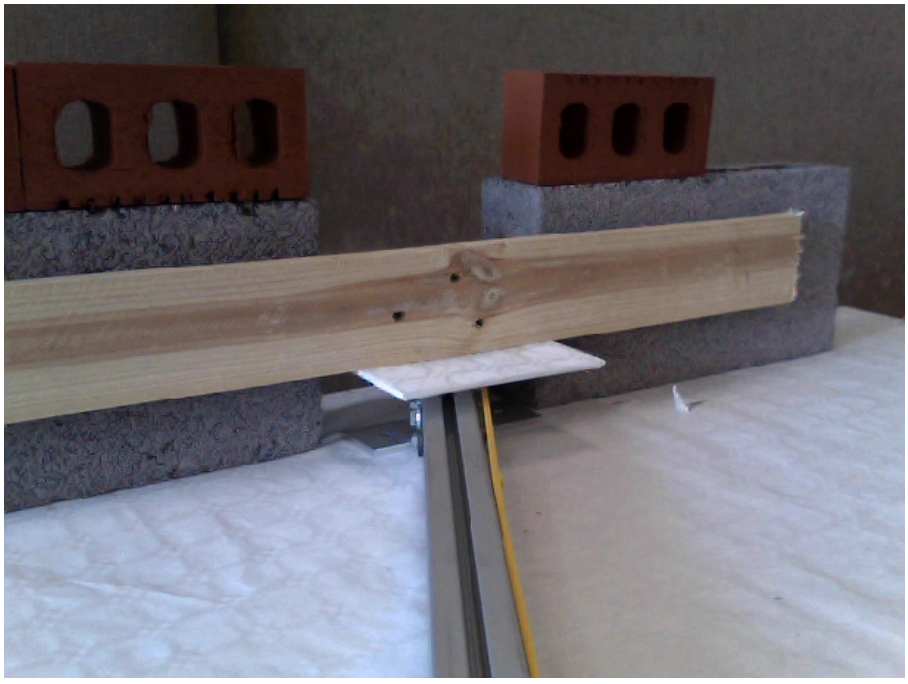

Figure 62 – Image from the VX-500 at 30° θ with at 5° pitch

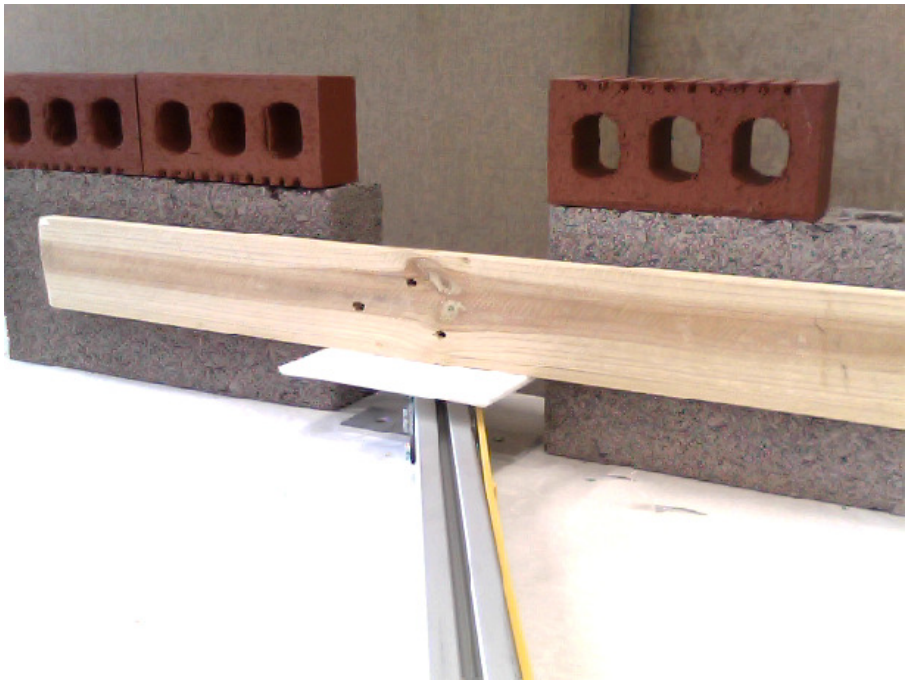

Figure 63 – Image from the VX-500 at -30° θ with at 5° pitch

Looking at the collected scans it is seen that the sensor suite gathered range data showed a series of targets with different sizes and positions in front of the simulated UAV.

The back wall behind the target is set at 1400mm, the brick and breezeblock targets were positioned 960mm away and the wooden plank is 925mm away from the world coordinate origin.

The back wall behind the targets is measured at 1421 – 1444mm away from the world coordinate origins. The wooden plank measured at between 937 – 961mm away from the world coordinate origin. The measured values of the brick were around 953 – 966mm and the breezeblock is around 943 – 967 from the world coordinate origin.

The physical dimensions of the targets were also measured from the data. The plank of wood is measured by the sensor suite to be 864.5mm long, 103.78mm high and approximately 22mm deep. The actual known physical dimensions of the wooden plank were 885mm long, 95mm high and 25mm deep.

The bricks were measured and found to be 194.98mm long, 67.9mm high and approximately 61.7mm deep. The actual known physical dimensions of a single brick were 210mm long, 100mm

high and 63mm deep. In individual scans the individual holes in the bricks were seen as gaps on the bricks surface, which returned values of the back wall behind the target.

The breezeblocks were measured and found to be 432.73mm long, 201.36mm high and approximately 102mm deep. The actual known physical dimensions of a single breezeblock were 440mm long, 215mm high and 100mm deep.

The gap between the two sets of bricks is also measured to be 127.98mm. The actual known physical value of this gap is 220mm.

9.3.3 Discussion

The back wall returned range values that were over the specified tolerance of the LRS at the distance measured ±10mm. The general target range values were under the tolerance of the LRS at the measured distance.

When the individual targets were analysed it is seen that the wooden plank is measured between 937 and 961mm. The minimum distance measured is 23mm lower than the actual known value of the wooden plank, and also outside of the tolerance of the LRS. It is seen that the difference between the known and measured values of length, height and depth were 20.5mm, -8.78mm and 3mm respectively.

The brick is measured between 953 – 966mm. The minimum distance measured is 7mm lower than the actual known value of the brick. The range values of the brick were not all inside the tolerance of the LRS. It is seen that the difference between the known and measured values of length, height and depth were 15.02mm, 32.1mm and 1.3mm respectively.

The breezeblock is measured between 943 – 967mm. The minimum distance measured is 13mm lower and the maximum distance is 7mm higher than the actual known value of the brick. The range values of the brick were outside the tolerance of the LRS. The range values of the breezeblock were not all inside the tolerance of the LRS. It is seen that the difference between the known and measured values of length, height and depth were 7.27mm, 13.64mm and -2mm respectively.

The fact that the gathered data is not within the LRS tolerance is not unexpected. An experiment conducted into real world materials in section 9.2.12 showed that the majority of the data returned values that were ±20mm of the target rather than the tolerance stated by the LRS specification.

9.3.4 Conclusion

The real world test environment experiment showed that the sensor suite mounted on a simulated UAV could gather range scans that were processed into 3D point clouds. The simulated UAV gathered data similar in a similar manner to that of a real UAV if it were flying around a target area gathering data. The data gathered from the sensor suite also gave results as expected on materials that would be encountered whilst performing an indoor building inspection and showed that the majority of the results were within ±20mm of the targets known value.

9.4 Conclusion

This chapter described the experiments conducted in order to assess the suitability and viability of performing indoor building inspection using a UAV and suitable sensor suite. It is shown that the URG-04LX requires a "warm up" period where the returned value of range data is not within the URG-04LX's stated accuracy of ±10mm. It is observed that after around 140minutes of the laser is turned on that its accuracy had increased to higher than that stated by the specifications of the device. From these results every time the URG-04LX is sub sequentially used it is allowed 140 minutes to "warm up" before measurements were recorded.

The coloured paper experiment results showed that the colour of the target paper had an effect on the returned range value. This is especially seen on the black paper as the returned values were lower than the known range of the target. The red and silver paper targets returned higher than expected values than the known range of the target.

The real materials experiment results showed that the colour and type of material had an effect on the returned range value. It is seen that highly polished surfaces produced poor results. The majority of the targets returned range values within ±20 mm of the targets known range.

The real materials experiment also showed that as the distance to the target increases, the tolerance of the URG-04LX to return accurate range data also increases. It is decided that to minimise possible errors and increase the accuracy of the URG-04LX that scans of targets are performed up to a maximum of 1 Meter away from the target.

The real world test environment results showed that the majority of the targets still return range values within ±20mm of the targets known range. The simulated UAV and sensor suite is used to

gather range data and visual images on real world targets and the proposed method for gathering data for an indoor inspection using a UAV and sensor suite had been shown to work.

9.5 References

[1] L. Kneip, F. Tˆache, G. Caprari, and R. Siegwart, “Characterization of the compact Hokuyo URG-04LX 2D laser range scanner,” *2009 IEEE International Conference on Robotics and Automation*. Kobe, pp. 1447–1454, 2009.

[2] L. Hokuyo Automatics Co, “Scanning Laser Range Finder Documentation,” *Hokuyo Automatic LTD*, 2005. [Online]. Available: http://www.hokuyo-aut.jp/02sensor/07scanner/download/products/urg-04lx/data/URG-04LX_spec_en.pdf. [Accessed: 02-May-2010].

Chapter 10 Conclusions and Future Work

10.1 Conclusions

The project has produced encouraging results for the prospect of using a small sensor suite mounted on an unmanned aerial vehicle operating inside a building to perform indoor building scanning. It has been shown that the payload has met its aims and has given a good foundation on which to build an alternative method to perform indoor building scanning.

A sensor suite was developed and a method was shown that allowed for suitable representations in 3D of 2D range scans.

A mathematical description of the orientation and position of a target relative to the sensor suite, unmanned aerial vehicle and world coordinate system was presented.

The test rigs, on which the experiments were performed, were constructed successfully. The 1st test rig showed that a 3D point cloud can be produced from a 2D laser range scanner. The use of the point cloud provided a clear display of the 3D data and the mesh provided limited use unless anomalous data points were removed as seen in chapter 8. The 2nd test rig showed that it can simulate an unmanned aerial vehicle performing an indoor building scanning. The mathematical model developed to describe the 3D point cloud showed that it could provide accurate representations of the range data. It was seen that small errors in the sensor suite and UAV position are possible and can influence the accuracy of the 3D point cloud. The addition of a programmable pitch goniometer and UAV position would be necessary in order to more accurately position the sensor suite and UAV.

The data fusion method used showed that both data sets gathered by the test rig can be fused together allowing the physical dimensions to be found from a visual image. It was shown that the affine transform provided the lowest level of error using this method. The programs developed for simple distance measurements also showed that they perform simple measurements to within ±10mm.It has been seen since completion of the research that other methods of data fusion can be used to more accurately describe the mathematical relationship between a 2D and 3D coordinate system.

The sensor suite showed that a suitable warm up period is required for the laser range scanner to reach an equilibrium from which repeatable results can be taken. Experiments performed to validate

the choice laser range scanner showed that simple coloured and “real world” targets had an effect on the ability of the laser range scanners range accuracy. It was seen that the laser range scanner cannot always meet its supplied specifications and is dependent on the type of target. Experiments performed to validate the simulated unmanned aerial vehicle and sensor suite in a “real world” test environment showed that the system can gather large amounts of multiple 2D range data and also visual images. After manual post processing it was seen that the mesh can be used to display the 3D point cloud data. It has been seen that although large amounts of data can be collected quickly by the LRS the targets scanned had a relatively low resolution. This could be due to the step size of the LRS used and that of the stepper motor. A smaller step on the LRS would have allowed a higher resolution scan which would improve the overall accuracy of the data being gathered as it could resolve smaller objects and defects.

It has been shown that the simulated UAV and sensor suite can perform indoor building scanning in a laboratory environment. The results of this project demonstrate the principle of controlling the UAV and sensor suite, there are significant problems that remain to be solved before any commercial development. In the short term it is likely that the sensor suite needs to be mounted onto a real UAV and tested while in a flying environment. To implement this, the sensor suite pitching and yawing controls would need to be completely automated and miniaturised. Using these would give an associated power, weight and cost penalty. Once the sensor suite has been made airborne tests will need to be done in real world environments. Other issues like accurate position and orientation of the UAV will be encountered and so strategies to deal with this must be found.

10.2 Future Work

In order to take the project from its current early state to completion, work on other areas is going to be required. The problem of 6 degree of freedom SLAM required to accurately describe the position and orientation of the UAV will need to be solved. This could possibly be done with visual markers placed in the scanning environment to allow the UAV to localise relative to the observed marker. Alternatively a base stand could be used in order to project a laser light onto a surface in order for the UAV to localise relative to the base stand.

An additional line of investigation would be to look at how the sensor suite performed when placed on an actual UAV and flown around. From these additional measures for stabilising the sensor suite could be developed. After evaluating the UAV mounted sensor suite the test rig could then be

redesigned in order to incorporate any affects seen. The test rig can also be developed to have automated pitch, roll and yaw controls. This will mirror what will happen if the sensor suite is mounted on a real UAV and also provide more ways in which the sensor suite could scan a target as shown in chapter 4.

The use of meshes to display point clouds requires manual removal of any anomalous data points gathered by the laser range scanner. If a method to detect anomalous data points could be created it would reduce the amount time taken to manually remove them, which could increase the speed at which the data is processed and possibly reduce costs. One of the concerns when using an automated system to do this work is how to make the algorithm distinguish between anomalous data and useful data.

The research effort reported in this thesis has made a significant contribution to the feasibility of the overall concept. It is clear that several other difficult areas of work must be undertaken before a practical alternative system to performing indoor building inspections is created.

Appendix A

URG-04LX Command Communication Structure

The command communication structure of the URG-04LX uses a predefined set of commands that allow the user to control the device. The commands allow, for example, the user to specify the number of times it scans an object and the scanning Field of View (FOV). Other available commands on the URG-04LX allow the user to monitor the current state of the device, change internal motor speeds and to simulate errors within the device for diagnostic purposes. The communication from host personal computer to sensor (URG-04LX) is initiated from the host by sending a command signal that has a command symbol, parameter, string and then a line feed (LF), carriage return (CR) or both. On receipt of the communication the sensor replies with the command echo from the initial command with an appended status, sum, line feed, data relating to the command issued, sum and two line feeds as a termination code. This is shown in Figure 64 and Figure 65.

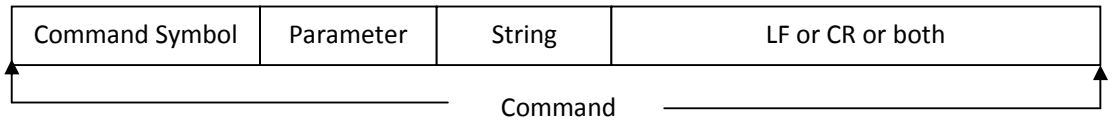

Figure 64 – Host to Sensor Communication Structure

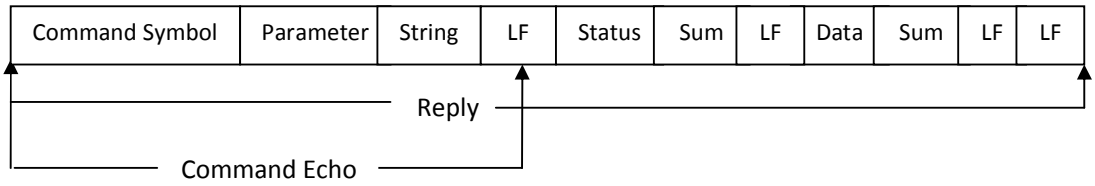

Figure 65 – Sensor to Host Communication Structure

Command Symbol – This is a code that begins every command, each command has a specific unique symbol for command verification.

Parameter – This is the information that the user can set in order to change the sensor settings or to request data from the sensor.

String – This information is optional and is not required by the sensor to perform any commands, but is a useful option available to the user. The String allows the user to verify when the same command is repeated by inputting different reference characters in the string section. The user can then check each command in the command echo to see which command has produced the data.

Line Feed (LF) or Carriage Return (CR) – This is used as a terminating code used by the command structure. This code was used when a command ends before beginning another.

Status – This information give the user the status of the URG-04LX at the time the scan was undertaken. If there are any errors produced when the command was issued the Status informed the user of the type of error.

Sum – This 1 byte data is used as an authentication marker to check that the data being sent back to the host between two line feeds is 64 bits long or less.

Data – This is the main information which directly relates to the command issued by the user. It is separated by a LF and sum after every 64 bits if it exceeds 64 bits.

Appendix B

Yaw Electronic Design

The position of the stepper motor that controls that yaw angle of the sensor suite needs to be accurately controlled. It was decided that the easiest way to implement this control was to use an electronic microcontroller. A PIC32 microcontroller was used to implement this control. The PIC32 has a number of I/O ports capable of interfacing with the stepper motor as well as a USB port to communicate with the PC. To make it easier to access the I/O ports on the PIC32 microcontroller a PIC32 expansion board (Figure 66) and also a PICtail plus daughter board (Figure 67) were used. This expansion board allowed the PIC32 microcontroller permanent mounting and also temporary fixings to allow access to some of the I/O ports. After preliminary testing it became apparent that more access to the I/O ports on the PIC32 microcontroller was required and the PICtail Plus daughter board also allowed a more permanent access for the wiring.

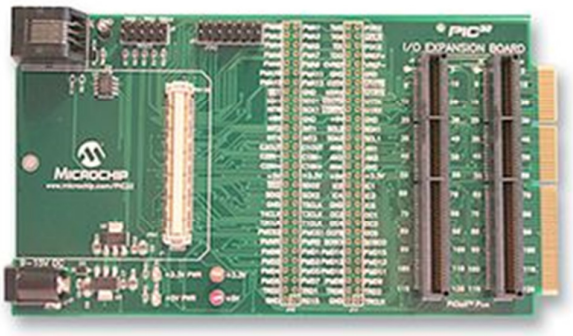

Figure 66 – PIC32 Expansion board

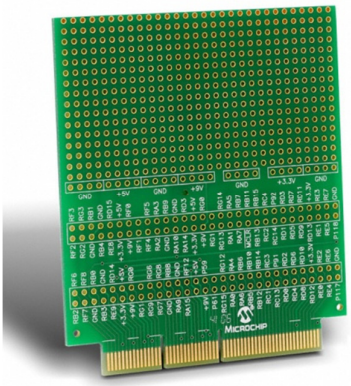

Figure 67 – PICtail Plus daughter board

The I/O ports on a PIC32 when set to a logical state high can supply +3.3V but low current. The MY701 stepper motor has a minimum input voltage of 2.5V and requires 2.1A which the PIC32 cannot supply. Using a bidirectional H-Bridge circuit (Figure 68), the voltage and current requirements of the stepper motor could be met while maintaining the control required to rotate the motor.

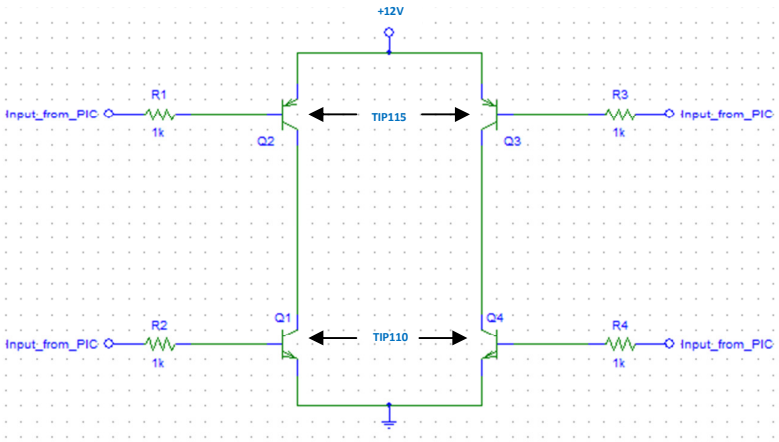

Figure 68 – H-Bridge Circuit Diagram

After designing and implementing a suitable bidirectional H-bridge circuit the stepper motor can be driven and controlled as shown below in Figure 69

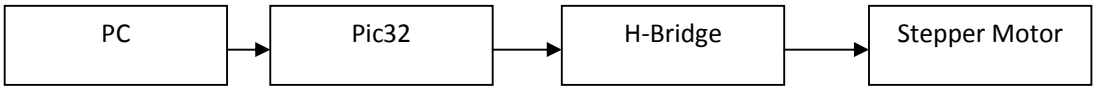

Figure 69 – System communication flow diagram

PIC32 Coding

To control the stepper motor the PIC32 microprocessor required coding in order to correctly energise the magnets within the stepper motor. The stepper motor used was a hybrid stepper motor. A hybrid stepper motor uses the characteristics from both variable reluctance and permanent magnet. The stepper motors permanent magnet provides the rotor flux and is guided by the rotor teeth to the correct parts of the air gap. The stepper motor permanent magnet is placed in the middle of the rotor and is magnetised in the axial direction. The poles of the magnet are surrounded by soft toothed laminations[82]. “The main flux path is from the north pole of the magnet into the end stack”, (A stack is a magnetically isolated section of the motor along its axial length[82]) “across the air gap through the stator pole, axially along the stator, through the stator pole, across the air gap and back to the magnet south pole via the other end stack.”[82]

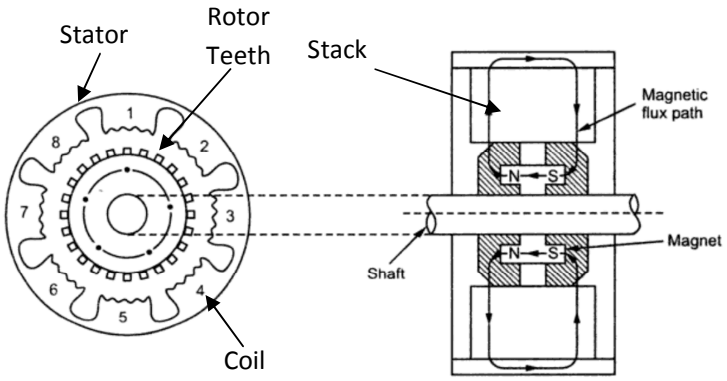

Figure 70 – Hybrid Stepper Motor [82]

The PIC32 controls of the hybrid stepper motor by controlling the current flow to the windings. There are eight poles on the stator of the MY701 hybrid stepper motor, with each pole controlling several teeth. This device has a two phase winding system[83] which means that the coils on poles 1, 3, 5 and 7 are connected in series to form phase A. Coils 2, 4, 6 and 8 are connected in series to form coil B. The specific order that the poles are energised (raised from no voltage to a high voltage) determines which way the stepper motor is to rotate. "When phase A has a positive current applied to it the stator poles 1 and 5 become south and 3 and 7 become north. The rotor teeth with north and south polarity align with the teeth of stator poles 1, 3, 5 and 7 respectively. When A is de-energised and B energised the rotor will move by one quarter of the tooth pitch."[82] When the current is reversed the poles 1 and 5 become north and 3 and 7 become south and the rotor teeth with north and south polarity align with the teeth of stator poles 1, 3, 5 and 7 respectively.

In the MY701 the coils are arranged as shown in Figure 71. The phase A is represented by the black (A) and green wires (C) where phase B is represented by the red (B) and blue (D) wires

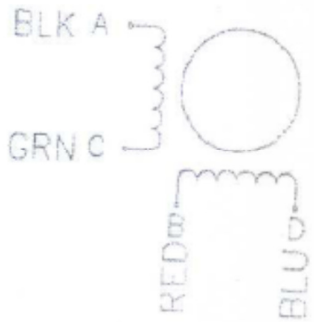

Figure 71 – MY701 Magnetic Coil Windings [83]

If for example the windings were energised one at a time in the required order, they rotate in increments of 1.8°, but the different energising configuration Figure 72 shows how to control the stepper motor to implement half-stepping control which yields a smaller rotation increment of 0.9°. One of the main advantages of using half-stepping is that it has smaller increment steps of the stepper motor and allows for the sensor suite to gather data at a greater resolution. The code for the control of the stepper motor is written in MPASM, which is the assembly language of the PIC microcontrollers.

The sensor suite's yaw position can now be set to repeat a pre-programmed sequence. This allows it to be automated or customised to yaw in a pre-set manner such as a large arc or maintaining a specific position to gather data. Using the PIC32, a method for controlling the stepper motor has been designed. This allows the sensor suite to yaw quickly and automatically on a pre-programmed sequence which increases the speed at which the data is gathered.

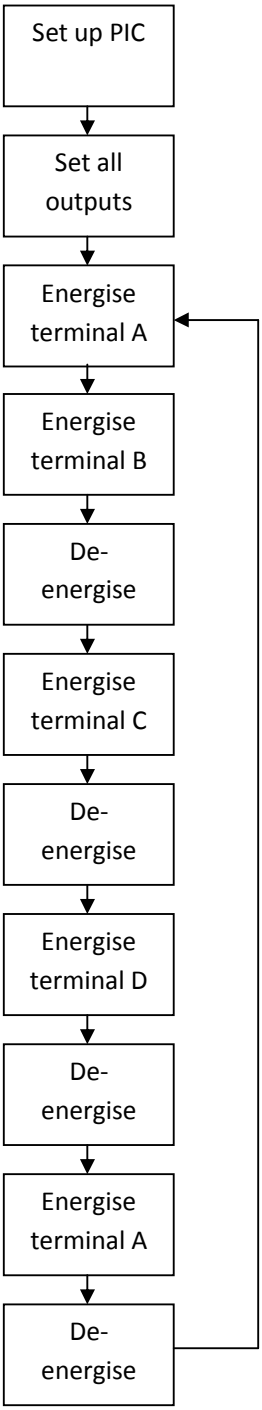

Figure 72 - Stepper Motor Flow Diagram